Electron Spin Properties of Carbon based Nanomaterials: Metallofullerenes, Nanotubes and Peapods



Mujtaba Zaka

Department of Materials

University of Oxford

A thesis submitted for the degree of

Doctor of Philosophy

Trinity Term 2011

Abstract

The successful utilization of carbon nanomaterials in future electron spin-based technologies is highly dependent upon the ability to control their assembly at the nanoscale to form tailored solid-state architectures. Spin active metallofullerenes (MFs), Sc@C_{82} and La@C_{82}, can be self assembled in 3D fullerene crystals or inside a carbon nanotube to form peapod structures.

Single walled carbon nanotubes (SWCNTs) are an architect material to potentially allow the formation of 1-D spin chains. SWCNTs should be optimised to allow formation of spin chains and free of magnetic catalyst and carbon impurities, which have previously limited investigations of SWCNT spin properties. To address this, SWCNTs produced by laser ablation with a non-magnetic PtRhRe catalyst were purified through a multiple step centrifugation process in order to remove amorphous carbon and catalyst impurities. Centrifugation of SWCNT solutions resulted in sedimentation of carbon nanotube bundles containing clusters of catalyst particles, while isolated nanotubes with reduced catalyst particle content remained in the supernatant. Electron paramagnetic resonance (EPR) signals were only detected for samples which contained catalyst particles, with the ultracentrifuged SWCNTs showing no EPR signal at X-band (9.4 GHz) and fields $\leq$0.4 T.

Integration of MFs into future devices requires a clear understanding of the nature of the spin and spin-spin interactions. Evaluating the spin properties of MFs, in both 3D (crystals) and 1D (peapods), will identify the spin-spin interactions and the affect of the surrounding SWCNT. Diluting spin active Sc@C_{82} and La@C_{82} MFs in a diamagnetic C_{60} matrix, between 0.4% and 100%, permitted the tuning of the mean fullerene separation and thus interfullerene spin interactions. In dilute concentrations

of MFs the hyperfine structure was resolved in EPR and with increasing concentration exchange narrowing was observed as a single narrow EPR peak.

Encapsulation of $Sc@C_{82}$ MFs, of varying dilutions, into purified SWCNTs allowed formation of highly ordered 1-D array of metallofullerenes. Changing the spin environment from 3D crystal to 1D peapod resulted in the loss of the observed hyperfine structure in EPR. A single narrow peak was observed for $Sc@C_{82}$:C_{60} peapods, indicating significant affect of the surrounding SWCNT structure upon the spin interactions of 1D metallofullerenes. Peapods of $Ce@C_{82}$ showed a similar EPR signal, suggesting that the observed narrow peak arises from charge transfer between the MF cage and the surrounding SWCNT.

I would like to dedicate this thesis to my parents

Asma and *Yasin Zaka*

for their love and inspiration

Acknowledgements

I count myself fortunate to have had the opportunity to work in such a friendly, entertaining and dynamic group. Jamie Warner has been a phenomenal supervisor and I truly appreciate all the assistance he has provided. Jamie has been great to work with, whether in the lab or on the TEM, and to socialize with outside of the office, in particular playing cricket and tobogganing come to mind. Special mention goes to Yasuhiro Ito for his wealth of knowledge of everything fullerene related, his supplies of highly purified metallofullerenes and his unique sound effects. I would like to thank Fran for her assistance with TEM and possibly more important, her weekly supply of brezns (German pretzels). Members of the group Yimin, Alex, Raj, Evan, Wenjing, Chris and Katie, have been great to work with, fun to socialize with and have provided many fond memories and I wish them all the best for the future.

Most of my experiments have often been tedious, however, the time spent producing nanotubes at the IFW Dresden with Mark Rümmeli was one the highlights of my DPhil. I would like to thank Mark, Ronny, Sailaja, Alicja, Ferdinand and Vladislav for their help with nanotube production and EPR experiments and for introducing me to some novel aspects of Dresden, 11.30am lunches, medieval Christmas markets and Swiss-Saxony.

I would like to thank John Morton and Arzhang Ardavan for their assistance with EPR experiments and advice on modelling. I would like to thank Kyriakos his support in lab work and the regular supplies of EPR tubes. I would like to acknowledge David Staunton for access to the Biochemistry ultracentrifuge. I would like to thank Jeffrey Harmer for assistance with the EMX spectrometer. I would like to express my

gratitude for supervision by Andrew Briggs who has continually provided great advice, encouragement to explore challenging and rewarding goals and support to establish collaborations and attend conferences. I thank the EPSRC for funding my DPhil and the British Carbon group, St. Anne's College and the Department of Materials for providing funds to attend conferences.

Rizvi, Vasileia, Richard, Thomas, Gouquan and Hua have been great to share an office with. Living with Rizvi, for almost four years, mainly consisted of partying, gaming, Nandos, occasionally working and importantly lots of laughter, simply put good times - Going to miss you loads!!! Vasileia is one of my best friends and she knows me so well. She has provided an appreciation of everything Greek, and so the best to describe her is $\kappa\alpha\tau\alpha\pi\lambda\eta\kappa\tau\iota\kappa\acute{\eta}$ $\varphi\acute{\iota}\lambda\eta$. Congrats to Richard on winning fantasy football this year, though I am sure I will regain the top spot next year but it won't be the same without our daily football discussions. Tahsina, Kirren, Sina and Mohammad are some of my closet friends and I will miss all the fun times we had. I have enjoyed my time at St. Anne's college and would like to thank all the great friends that I have made and I look forwarding to seeing you all again. I would like to thank all the members of the Materials cricket team, for providing much fun over the summer months.

Finally, I must thank my family, my brother and sister, Baber and Saiher, and my parents Asma and Yasin, for putting up with me for four years and encouraging me to finally leave the student world and get a real job.

Contents

Contents vi

Nomenclature ix

1 Introduction 1

2 Carbon Nanomaterials 4

2.1 Introduction to Carbon Nanomaterials 4

2.2 Metallofullerenes 5

2.2.1 Synthesis of Endohedral Metallofullerenes 7

2.2.2 Structure of Endohedral Metallofullerenes 10

2.2.2.1 Cage Isomerisation 12

2.2.3 Properties of Endohedral Metallofullerenes 12

2.2.3.1 Electronic properties 13

2.2.3.2 Optical Properties 16

2.2.3.3 Magnetic properties 18

2.3 Carbon Nanotubes 19

2.3.1 Structure of Carbon Nanotubes 21

2.3.2 Carbon Nanotube Synthesis 22

2.3.3 Purification of Carbon Nanotubes 29

2.3.4 Towards Carbon Nanotubes Homogeneity 31

2.4 Peapods 35

2.4.1 Synthesis of Peapods 36

2.4.2 Structure of Peapods 39

2.4.2.1 Ordering and Orientation of Peapods 41

2.4.3 Properties of Peapods 42
2.4.3.1 Electronic Properties of Peapods 43
2.4.3.2 Transport Properties of Peapods 45
2.4.3.3 Dynamics of metallofullerenes in peapods 46
2.5 Summary 48

3 Experimental Methods **49**
3.1 Electron Paramagnetic Resonance 49
3.1.1 Principles of CW EPR 50
3.1.2 Practical Methodology 53
3.2 Transmission Electron Microscopy 54
3.3 Optical Absorption 58
3.4 Raman Spectroscopy 60

4 Purified Carbon Nanotubes Spin Properties **63**
4.1 Introduction 63
4.2 Purification of Carbon Nanotubes 65
4.2.1 Principles of centrifugation 66
4.2.2 Experimental Methods 67
4.2.3 SWCNT Ultracentrifugation 75
4.3 Analysis of Purified SWCNTs 83
4.3.1 Nanotube Composition 84
4.3.2 Purity analysis using absorption spectroscopy 87
4.3.3 Structural Analysis 91
4.4 Spin properties 93
4.4.1 Electron Paramagnetic Resonance 93
4.4.2 Vibrating Sample Magnetometer 98
4.4.3 Raman Spectroscopy 100
4.4.4 Paramagnetic Properties 100
4.5 Summary 103

5 Metallofullerene Spin Properties **105**
5.1 Introduction to Metallofullerenes 105
5.1.1 MF Spin Properties 107

5.1.1.1 Spin Interactions 107
5.2 EPR investigations 109
5.2.1 Experimental methods 110
5.2.2 EPR results La@C_{82} 111
5.2.2.1 Simulating the spin 111
5.2.3 EPR results Sc@C_{82} 113
5.3 Discussion 114

6 Interactions in Peapods **117**
6.1 Introduction to Peapods 117
6.2 Production of Peapods 118
6.3 Analysis of Peapods Structures 120
6.3.1 PtRhRe laser ablation SWCNT peapods 120
6.3.2 Metallic and Semiconducting SWCNT Peapods 137
6.4 Summary 149

7 Conclusions **151**

List of Publications **155**

References **157**

Nomenclature

1D	1-dimensional
3D	3-dimensional
AFM	Atomic force microscopy
CNT	Carbon nanotube
CoMoCat	Co and Mo catalyst chemical vapour deposition
CVD	Chemical vapour deposition
CW	Continuous wave
DFT	Density functional theory
DGU	Density gradient ultracentrifugation
DOC	Deoxycholate
DOS	Density of states
DWCNT	Double walled carbon nanotube
EELS	Electron energy loss spectroscopy
EPR	Electron paramagnetic resonance
ESEEM	Electron spin echo envelope modulation
FET	Field effect transistor
FFT	Fast Fourier transform
FWHM	Full width half maximum
GMR	Giant magnetoresistance
HiPCO	High pressure carbon monoxide
HOMO	Highest occupied molecular orbital
HPLC	High performance liquid chromatography
HRTEM	High resolution transmission electron microscopy
LUMO	Lowest unoccupied molecular orbital
MEM	Maximum entropy method
MF	Metallofullerene

MWCNT	Multi walled carbon nanotube
OAS	Optical absorption spectroscopy
PtRhRe	Platinum, rhodium, rhenium catalyst mixture
QIP	Quantum information processing
SC	Sodium cholate
SCFs	Super critical fluids
SDS	Sodium dodecyl sulphate
SQUID	Superconducting quantum interference device
STM	Scanning tunnelling microscope
STS	Scanning tunnelling spectroscopy
SWCNT	Single walled carbon nanotube
TEM	Transmission electron microscopy
UV-Vis	Ultraviolet visible
VSM	Vibrating sample magnetometer
X-band	Radiation with frequency around 9.5 Ghz
XRD	X-ray diffraction

Chapter 1

Introduction

The development of future technologies to replace existing silicon based technologies, has brought huge interests into the emerging field of spintronics which could potentially revolutionize the electronics industry. Spintronic technologies are based upon harnessing the spin of a particle in contrast to its charge. Electrons have spin properties which can be manipulated and the spin has quantum properties. These quantum properties permit information to be stored in a superposition of the spin states and have potential application in quantum information processing.

Spintronics is currently employed in read head and magnetic memory devices based upon giant magnetoresistance (GMR) [1, 2]. GMR has been observed in systems consisting of ferromagnetic layers sandwiching a non magnetic metallic layer. Device resistance depends on the relative orientations of magnetization in the ferromagnetic layers, with small resistance when there is parallel magnetization, and large resistance when anti-parallel magnetization. This observed change in resistance can been used to detect changes in the magnetic field and has been exploited in spin valve devices. Spintronics applications are also being developed using semiconducting systems [3, 4] with potential application in sensor, memory and logic

devices [5]. Electron or nuclear spins also exhibit quantum properties. Spins can have an "up" or "down" state or a superposition of the two states to form a qubit, the building block of quantum information processing (QIP) [6]. QIP is a desirable technology as the advanced computation has potential applications in cryptography and simulations.

A potential candidate for spin based technologies, in particular QIP [6], is an endohedral metallofullerene. Atoms can be inserted into the vacant hollow interior of the fullerene cage forming novel structures, such as Sc@C_{82}, La@C_{82} or N@C_{60}. Metallofullerenes can hold single electron spins with long coherence times [7] and, therefore, have promise as building blocks for electron spin based technologies. Advances in the synthesis of spin active metallofullerenes have allowed for high yields and purity, making metallofullerenes more encouraging than N@C_{60}, which suffers from challenges in separation and purification. Utilization of metallofullerenes, such as Sc@C_{82} and La@C_{82}, in devices is highly dependent upon a tailored solid-state architecture to enable controlled assembly of the metallofullerenes at the nanoscale.

The challenge of controlled self assembly can be potentially solved by either forming 3D fullerene crystals or a 1D array of metallofullerenes filled inside a single walled carbon nanotube (SWCNT). Macroscopic crystals of metallofullerenes diluted with empty caged fullerene should allow control over the metallofullerene spin-spin interactions. Metallofullerenes can be inserted into the hollow interior of SWCNTs to form novel peapod structures and offer a route to non-covalent highly ordered one dimensional (1D) crystal, as shown in Figure 1.1. Upon encapsulation these hybrid peapod structures have been shown to have novel electronic properties compared to the constituting components. Encapsulation of Gd@C_{82} in SWCNTs has been demonstrated to show localized band gap modulation at metallofullerene

sites, through charge transfer and elastic strain, which can be manipulated to allow band gap engineering [8]. The spin of the metallofullerene species can be exploited

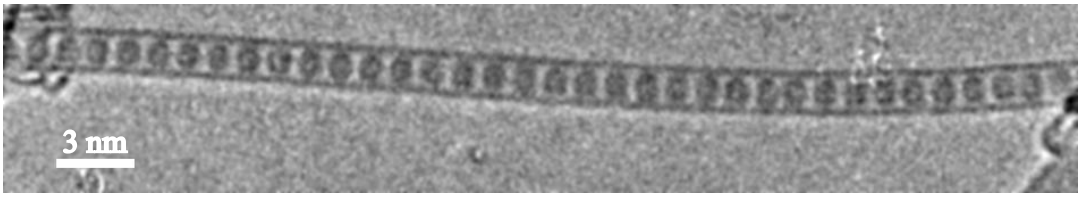


Figure 1.1: HRTEM image of a 1-D ordered array of Y@C_{82} metallofullerene in a SWCNT

for use in spintronic devices, spin labelling or quantum information processing. Important goals towards achieving these applications are control over the assembly of spins and a clear understanding of nature the spin properties in these systems. This thesis focuses on understanding the nature of the interactions between metallofullerene spins in 3D crystals and how they are affected upon encapsulation inside SWCNTs to form 1D arrays.

Chapter 2

Carbon Nanomaterials

2.1 Introduction to Carbon Nanomaterials

A novel area of carbon based research, developed over the last few decades, is the exploration of carbon nanomaterials based on newly discovered allotropic forms, fullerenes, nanotubes and graphene, as shown in Figure 2.1. These nanomaterials exhibit sp^2 carbon-carbon bonds and possess a unique blend of structural and electronic properties with a wide range of applications.

Fullerenes consist of a carbon cage with a hollow interior and despite the curvature the structure is highly stable. The hollow centre of the fullerene cage can be occupied by foreign atoms, forming a hybrid metallofullerene material. The cage provides a unique environment where the atom(s) are stabilised, and allows access to atomic-like systems. Carbon nanotubes are cylindrical carbon sheets with a hollow interior, existing as single cylinders or concentric cylindrical systems. Carbon nanotubes can be filled with other molecules, such as metallofullerenes, to form highly ordered 1-dimensional systems, commonly termed peapods. These peapod systems

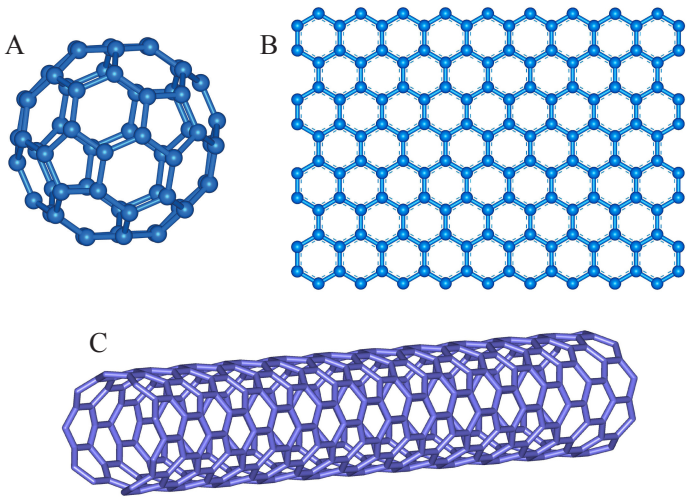


Figure 2.1: Schematic image of (A) C_{60} fullerene (B) Graphene sheet (C) Single walled carbon nanotube

offer an approach to investigate the properties of highly ordered 1-dimensional systems.

2.2 Metallofullerenes

C_{60} fullerene was famously discovered by Kroto *et al.* and opened new interest into carbon based materials [9]. Other caged structures, shown in Figure 2.2 have since been developed, and a new avenue of fullerene chemistry been explored by the encapsulation of atoms inside the hollow centre of these fullerene cages. The cage structure provides a stable environment for the encapsulated atom to exist, offering a distinctive way to investigate otherwise unstable atoms. Encapsulation of metal atoms into cage systems can be used in a broad range of applications, from spintronic devices, utilizing the spin properties of the metal atom [6], to MRI contrast agents [10], where the cage provides a closed environment preventing degradation of

hazardous Gd based contrast agents. These unique systems have sparked interest to understand the nature of these endohedral systems, in particular the interaction between the metal atom and the fullerene cage. The production of endohedral metallofullerenes systems have been a physical challenge, as often very low yields were produced, hindering investigations and implementation into applications. Significant efforts have been made to enhance the yield of production process and obtain larger quantities of endohedral metallofullerenesas well as their efficient separation and purification.

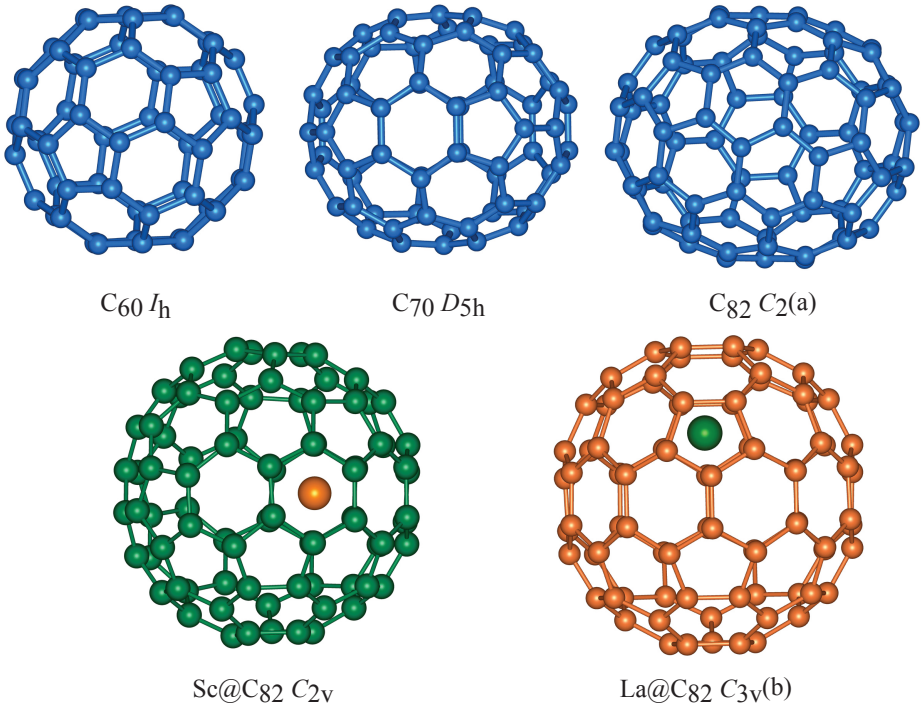


Figure 2.2: Image of different fullerene cages and isomeric form: $C_{60}(I\mathrm{h})$, C_{70} (D_{5h}, C_{82} (C_2(a)), Sc@C_{82} (C_{2v}) and La@C_{82} (C_{3v}(b)) .

2.2.1 Synthesis of Endohedral Metallofullerenes

The main methods employed for the production of macroscopic amounts of endohedral fullerenes are DC arc-discharge [11], high-temperature laser vaporization [12] and ion bombardment [13] of a fullerene substrate. Metallofullerene production methods have been optimized to allow large scale quantities of endohedral metallofullerenes to be produced and purified, permitting the chemical and physical properties to be investigated. Of the three methods, DC arc discharge offers a route for large scale production of endohedral metallofullerenes. Metallofullerenes used in experiments were produced via arc discharge and purified by high performance liquid chromatography (HPLC). The metallofullerene samples were obtained through a collaboration with the Shinohara labs.

Arc Discharge

DC arc discharge functions by producing an arc between the cathode, a carbon rod, and the anode, a composite rod containing a metal oxide and graphite. The arc burns the rods releasing hot carbon vapour in a depressurized He atmosphere. Upon cooling, carbon atoms collide to form fullerenes and endohedral metallofullerenes species. The soot produced is collected under anaerobic conditions [11], to minimise degradation of any air sensitive metallofullerenes. Figure 2.3, shows a schematic design, taken from [14], of an arc discharge system used by the Shinohara group and also shows photos of the arc discharge system used to produce metallofullerenes in Shinohara labs.

The drawbacks of the current production method of endohedral metallofullerenes are the relativity high proportion of empty caged fullerenes that are produced, re-

quiring the extensive use of HPLC to extract the small quantities of endohedral metallofullerenes. Chromatography has been challenging as the desired endohedral metallofullerenes are of similar size and shape to the empty caged fullerene, making separation difficult [15, 16]. HPLC has been further developed to allow high yielding single stage separations [17], by using more mobile phases, containing strong solvents for fullerenes, and modifying the stationary phase to improve fullerene and metallofullerene separations.

Investigations to improve the yield of endohedral metallofullerenes have led to a number of novel changes to the production process. Bandow *et al.* [18] demonstrated that using a LaC_2 enriched composite instead of La oxide increased the yield by a factor of 10. Employing M-Ni alloy as the metal source, rather than a metal oxide, also improved the yield [19] due to higher stability of the metal alloy and reduction of oxygen produced from the metal oxide. Using M-Ni alloys, in conjunction with high He pressure, high atomic ratio of M/C, low electric current and maintaining a large gap between cathode and anode, provided preferable formation of metallofullerenes over formation of empty caged fullerenes.

Laser Vaporization

An alternative route to the formation of endohedral metallofullerenes was reported by Huang *et al.* [12] where laser vaporization was applied to incorporate La atoms inside the fullerene cage. Excitation of La, in a composite of C_{60} and La_2O_3, provided a 'window' mechanism, where the La atoms penetrated an opening in the carbon cage. Theoretical modelling [20] supports the idea of a 'window' mechanism. Synthesis using laser vaporization has become a possibility, with endohedral fullerenes containing yttrium atoms have been successfully produced [21, 22]. Laser

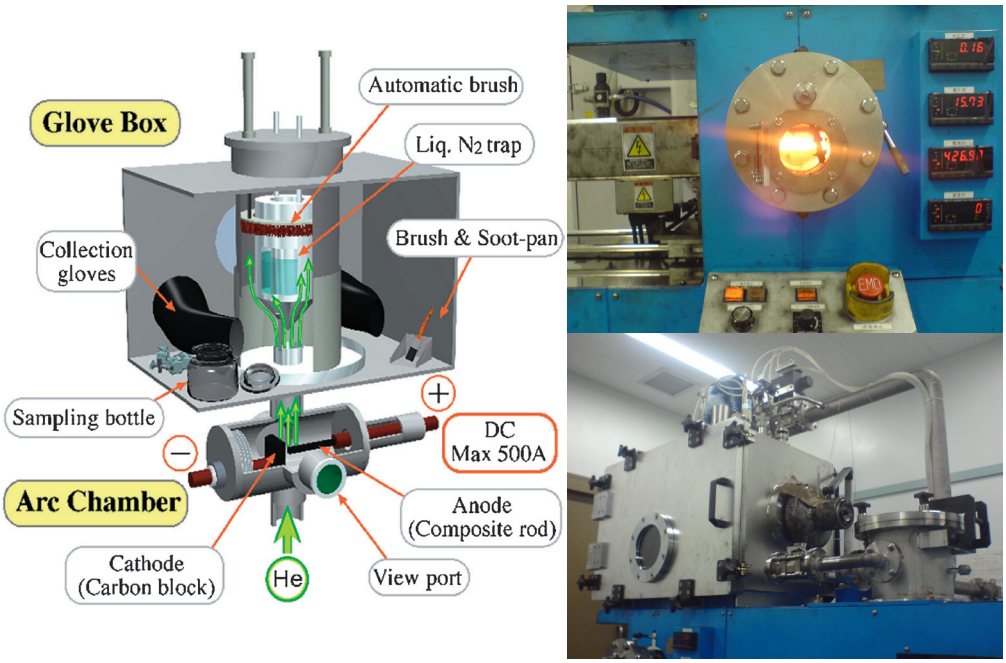


Figure 2.3: Large-scale DC arc-discharge as used by Shinohara *et al.* with anaerobic conditions used in the setup, preventing degradation of any air sensitive products [14]. Photo (top) shows the arc discharge system used to produce metallofullerene, through collaboration with Shinohara labs. Photo (bottom) shows the sample collection chamber where vaporised fullerenes were collected.

vaporization has been useful to study the formation mechanism of fullerenes and metallofullerenes [23, 24]

Ion Implantation

Ion implantation provides an interesting alternative for endohedral fullerene production. Ions of the desired species are electrostatically accelerated to a high energy and fired at the fullerene cage and isolated using HPLC, producing endohedral fullerenes. This method of production can not be used for metallofullerenes based on reactive atoms, such as La@C_{82}, but is used more commonly to produce fullerenes of alkali

metals [25] and group V fullerenes [26], such as $N@C_{60}$. For large scale production of metallofullerenes, DC arc-discharge and laser vaporization hold more potential than the ion implantation method.

2.2.2 Structure of Endohedral Metallofullerenes

Metallofullerenes were identified through mass spectroscopy experiments [27], however, the structure of these novel materials was only fully understood years later, primarily through characterization using X-ray diffraction (XRD) [28]. The uncertainties about the structure of metallofullerenes were concerned around the location of the metal atom. Soderholm *et al.* [29] investigated $Y@C_{82}$ through extended X-ray absorption fine structure (EXAFS) spectroscopy, but the experimental data could not produce a clear solution. Soderholm highlighted the possible scenarios of where the yttrium atom could be located, inside the C_{82} cage, functionalized on the outside of the cage or incorporated into the cage structure.

As the isolation and separation of metallofullerenes became easier, more experimental debate about the endohedral nature followed, scanning tunnelling microscopy [30], transmission electron microscopy [31] and electron spin resonance data [32] suggested that the metal atom is encapsulated inside the fullerene cage. Direct confirmation of the endohedral nature through structural data or models had been lacking, until Takata *et al.* [28] made the breakthrough in determining the nature of endohedral metallofullerenes using XRD. Takata *et al.* combined the XRD results with a combination of Rietveld analysis [33] and maximum entropy method (MEM) [34] to produce a structural model for $Y@C_{82}$ shown in Figure 2.4. The structural model showed high electron density inside the $Y@C_{82}$ cage, where the

number of electrons around the maximum totalled 38, close to the atomic number of yttrium. Comparison with a hollow C_{82} cage showed no electron density inside the cage. A measure of the distance from the centre to the yttrium atom, 3.14 Å, was much shorter than the 4.10 Å radius of the C_{82} cage. The combination of these results provided enough evidence to confirm that the yttrium atom is located inside the cage. These results also identified that the yttrium atom resided close to the edge of the cage, rationalized by the strong charge transfer between Y^{3+} and C_{82}^{3-} [35]. Similar XRD MEM has also been performed for other endohedral metallofullerenes including Sc_2C_{82} [36], $Sc@C_{82}$ [37] and $La@C_{82}$ [38], shown in Figure 2.4 also demonstrating that the electron density of the metal atom is located off centre due to charge transfer between the cage and metal atom.

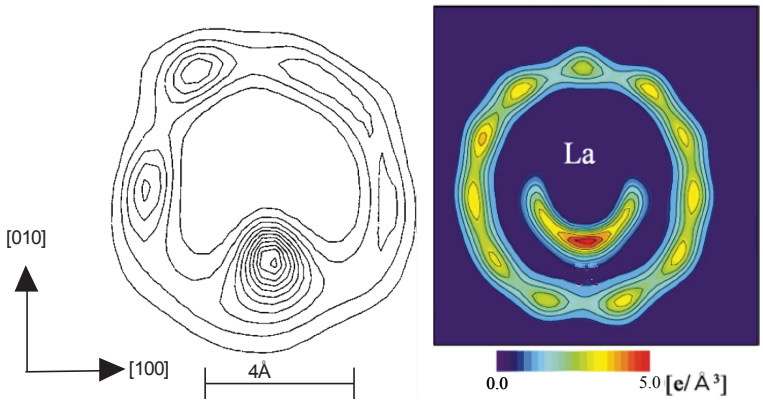


Figure 2.4: MEM electron density distribution of $Y@C_{82}$ for [001] section. Structural model provides evidence for the endohedral nature of $Y@C_{82}$ due to the high electron density off centre, corresponding to yttrium atom [28]. MEM electron density distribution for $La@C_{82}$ with an area of high electron density shown off-centre [38]. Contour Lines are drawn from 0.0 to 5 (e Å^{-3}) with a 0.5 (e Å^{-3}) step width.

2.2.2.1 Cage Isomerisation

The C_{82} cage has nine possible isomers based upon calculations derived from the isolated pentagon rule [39]. The calculations indicate that from the possible isomers the C_2(a) isomer is the most stable isomer. In metallofullerenes the metal atom transfers electrons to the fullerene cage, forming a charged species C_{82}^{n-}, where n is the number of electrons transferred and is dependent on the valency of the metal atom. For C_{82}^{n-} the C_2(a) isomer is no longer stabilised and in the case of trivalent metallofullerenes, La@C_{82} and Y@C_{82}, only 2 isomers have been isolated. Hoinkis *et al.* [40] reported that the single peak observed in the mass spectrometer data of La@C_{82} and Y@C_{82} produced additional lines in the EPR spectra. An additional octet was observed for La@C_{82} and a doublet of Y@C_{82} hyperfine structure due to two different species of La@C_{82} and Y@C_{82}. Similar results have been reported by Suzuki *et al.* [41] and suggested that each isomer would have different g values and hyperfine constants. Kobayashi *et al.* [42, 43] predicted the relative energies for isomers of C_{82}, C_{82}^{2-}, C_{82}^{3-} through ab initio molecular orbital and non-local density functional calculations, shown in Figure 2.5. The calculations indicate that the C_{2v} endohedral structure is the most stable for M@C_{82} species.

2.2.3 Properties of Endohedral Metallofullerenes

Due to the encapsulation of a metal atom, endohedral metallofullerenes possess properties which are not observed for empty caged fullerenes. The metal atom(s) will transfer electrons to the fullerene cage, forming a stable ion pair of a endohedral metal cation and an anionic fullerene cage. Interest in the electronic charge transfer properties of endohedral metallofullerenes has been plentiful, with the main aims

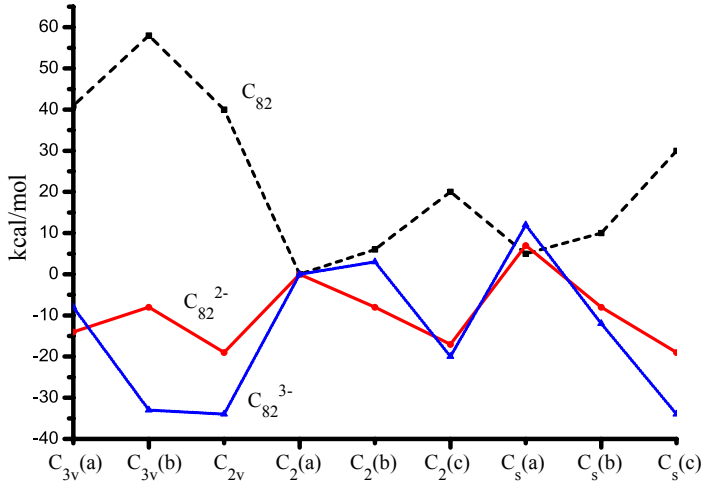


Figure 2.5: Energies of isomers of C_{82}, C_{82}^{2-}, C_{82}^{3-} relative to C_2(a) isomer

to determine the valency of all endohedral metallofullerenes and to understand the properties of different metallofullerene species.

2.2.3.1 Electronic properties

The charge transfer of the metal atom to the fullerene cage is fundamental to understanding the properties of endohedral metallofullerenes. XRD MEM measurements of La@C_{82} and Y@C_{82} indicated that the metal atom transfered three electrons to the cage, leaving the metal atom in a 3^+ valence state. Determining the valency of the Sc atom caused some controversy, with disagreements over whether the state is divalent or trivalent [44, 45]. Clarification was achieved through synchrotron X-ray results [37], UPS experiments [46] and XRD MEM measurements [47], indicating that the charge transfer from the Sc atom to the cage forms a $Sc^{2.2+}@C_{82}^{2.2-}$ state. DFT calculations [48] explained this phenomenon by strong hybridization between the Sc d valence orbital and the π orbital of the cage.

The paramagnetic properties of endohedral metallofullerenes have been studied

through electron paramagnetic resonance, with extensive research collected for solutions of EPR-active metallofullerenes Sc@C_{82} [49], La@C_{82} [50, 51] and Y@C_{82} [51]. To date most of the EPR conducted on endohedral metallofullerenes has been in solution, where the fast rotational dynamics of the fullerene cages gives isotropic signals. The unique charge transfer properties of these endohedral metallofullerenes permits observable hyperfine structure, whereby the electron and nuclear spin interact, with Sc@C_{82} and La@C_{82} exhibiting eight line hyperfine structure and Y@C_{82} exhibiting a doublet, shown in Figure 2.6A-C.

Electron paramagnetic resonance measurements by Johnson [50], first reported the observed hyperfine structure of La@C_{82}, suggesting that the origin of the EPR signal was due to a single unpaired electron localized in the $LUMO^{+1}$ level of the fullerene cage, due to the transfer of the three valence electrons of La ($5d^26s^1$) to the fullerene cage. As explained Sc@C_{82} behaves differently to La@C_{82} and Y@C_{82} due to the difference in valency. From EPR investigations the Sc ($3d^14s^2$) atom will transfer the two 4s electrons to the fullerene cage, while the remaining 3d electron will hybridize with the π orbital of the C_{82} cage. Most other endohedral metallofullerenes are EPR silent at room temperature and show only minimal structure at low temperatures. A metallofullerene which exhibits paramagnetic resonance is Sc_3@C_{82} [52], showing a hyperfine structure of twenty-two equally spaced lines, corresponding to three scandium nuclear spins of 7/2, shown in Figure 2.6D.

Structural isomers of the metallofullerenes Sc@C_{82}, Y@C_{82} and La@C_{82} can be detected in the EPR spectrum, [41, 40]. In each case the EPR spectrum shows the typical hyperfine structure, as mentioned above, but contains some satellite peaks, attributed to ^{13}C isotopes and the hyperfine structure of metallofullerene isomers. Separation of the minor isomer of La@C_{82} allowed Yamamoto *et al.* [53] to compare

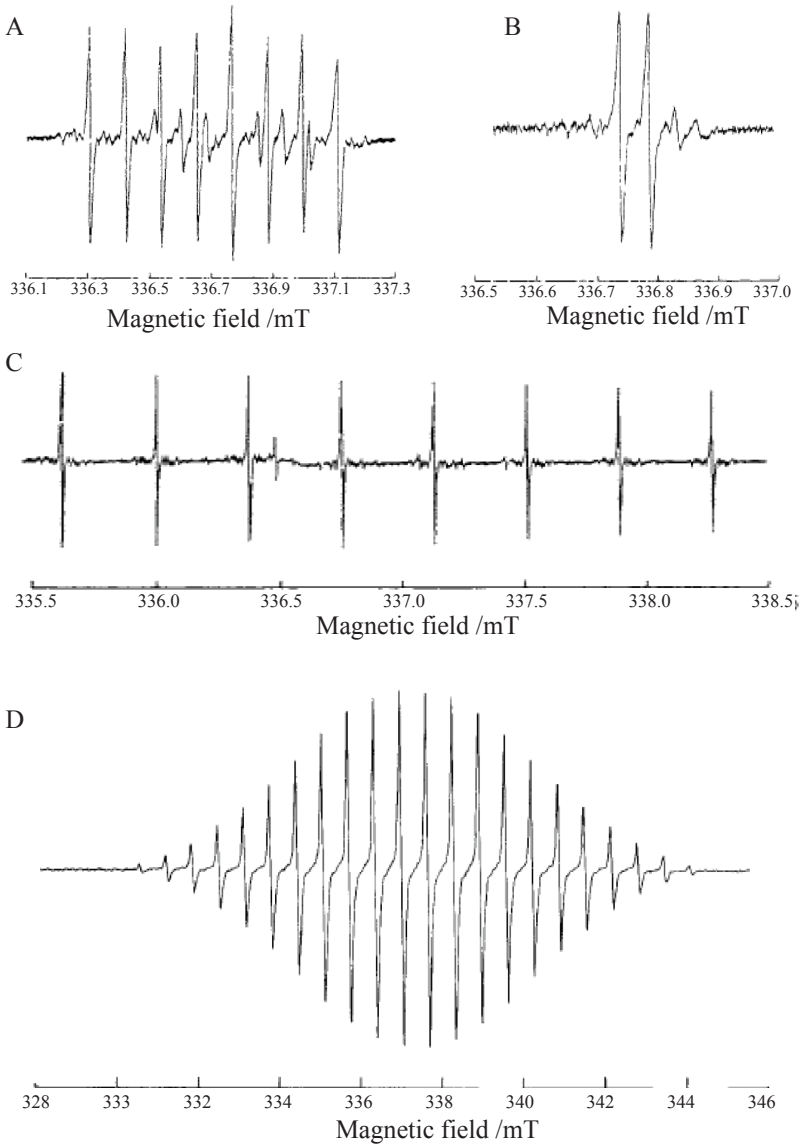


Figure 2.6: EPR spectra of (A) La@C_{82} showing eight hyperfine peaks (B) Y@C_{82} showing the two peak hyperfine structure (C) Sc@C_{82} showing eight hyperfine peaks (D) Sc_3@C_{82} showing the twenty-two equally spaced lines due to the three scandium nuclear spins [52]

the hyperfine structure between the major isomer La@C_{82}(I) and the minor isomer La@C_{82}(II). The hyperfine structure of the minor isomer La@C_{82}(II) is very similar to the major isomer, with eight equally spaced lines, however the hyperfine constant is smaller. This difference in hyperfine constants was also present for Y@C_{82} isomers [54] and Sc@C_{82} isomers [32] while still maintaining similar spectral structure.

Electrochemistry of endohedral metallofullerenes species has been performed to determine whether the endohedral metallofullerenes act as electron donors or acceptors. Redox properties of endohedral metallofullerenes were primarily investigated by Suzuki *et al.* [55, 56] by performing cyclic voltammetry (CV) on La@C_{82}, their study revealed interesting properties about La@C_{82} compared to empty caged fullerenes. Suzuki *et al.* demonstrated that the first oxidation potential (+0.07 V) is approximately equal to that of ferrocene, suggesting that La@C_{82} is a moderate electron donor. The reduction potential of La@C_{82} provided intriguing results, as five reversible waves were detected by CV, even though the C_{82} cage has a 3^- charge. It was also noted that La@C_{82} is a stronger electron acceptor than empty caged fullerenes [57]. Y@C_{82} shows strikingly similar CV results [56, 58] to La@C_{82}, their oxidation states are very close and both act as good electron donors and acceptors. Other fullerenes which have been studied are Ce@C_{82}, Gd@C_{82} [56] and Sc_3@C_{82} [59].

2.2.3.2 Optical Properties

On account of the charge transfer properties of endohedral metallofullerenes the optical properties are considerably different from those of empty caged fullerenes and the optical absorption has provided further understanding of these endohedral metallofullerenes. Absorption spectra of endohedral metallofullerenes show a broad

peak at around 1400 nm which extends down to around 2300 nm and some narrow peaks are also visible around 1000 nm and 600 nm. These peaks relate to the electron transfer between the metal atom and the fullerene cage. The absorption spectra of La@C_{82}, and Y@C_{82} in carbon disulfide show similarities in peak position, as seen in Figure 2.7A, however, for Sc@C_{82} the absorption spectrum is very different. This is due to the difference in charge state of the metallofullerenes, where Sc@C_{82} is divalent compared to trivalent of La@C_{82} and Y@C_{82}. Akiyama *et al.* [60] demonstrated similar absorption spectrum for a range of trivalent metallofullerenes M@C_{82} (M=La, Ce, Pr, Nd, Gd, Tb, Dy, Ho, Er, and Lu). They quantitatively analysed the absorption coefficients of these metallofullerenes, providing an accurate method to analyse the amount of isolated metallofullerenes in solution.

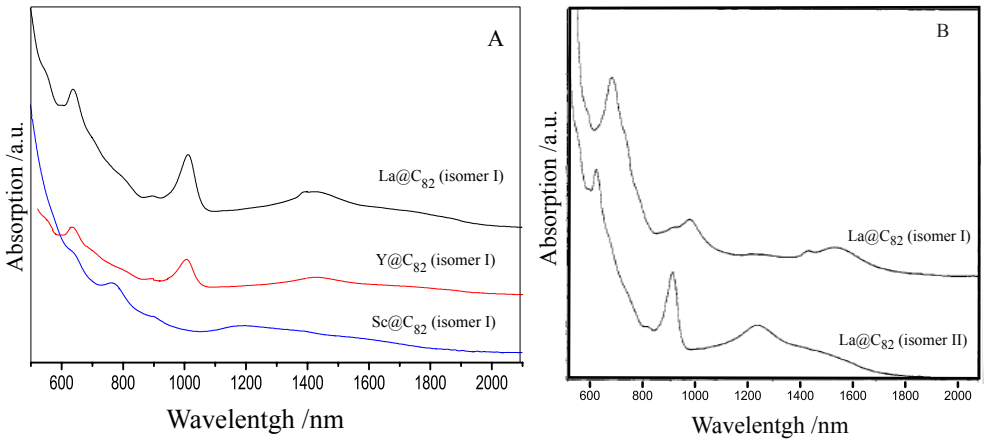


Figure 2.7: (A) UV-Vis-NIR absorption spectra for La@C_{82} (I), Y@C_{82} (I), Sc@C_{82} (I) in carbon disulfide. Spectra of Sc@C_{82} shows difference in absorption peaks to La@C_{82} and Y@C_{82}. (B) UV-Vis-NIR absorption spectra for major, La@C_{82} (I) and minor, La@C_{82} (II) isomers, showing differences in absorption peaks [53]

Isomers of metallofullerenes have different optical properties, Figure 2.7B shows a comparison of La@C_{82} isomers, with the minor La@C_{82} (II) isomer containing

shifted absorption peaks at 900 nm and 1200 nm [53]. UV-Vis-NIR absorption spectroscopy has illustrated differences in the spectra arising from the valency and isomerization of the metallofullerene species.

2.2.3.3 Magnetic properties

Detailed understanding of the magnetic properties of metallofullerenes was achieved through magnetic measurements by using Superconducting Quantum Interference Devices (SQUID). Funasaka *et al.* [61] pioneered the study of endohedral metallofullerenes with SQUID magnetic measurements, initially applying the method to study bulk $Gd@C_{82}$, due to the Gd large magnetic moment of 7.94 μ_B. SQUID magnetic measurements confirmed the paramagnetic nature of Gd by indicating that the inverse magnetic susceptibility is proportional to temperature, shown in Figure 2.8A, fitting well with the Curie-Weiss law throughout the measured temperature range.

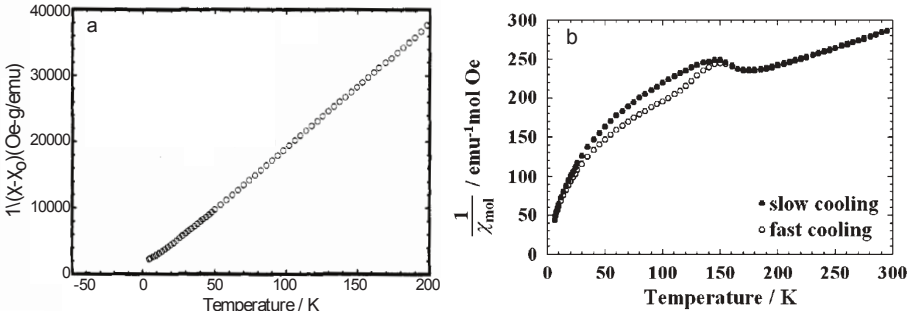


Figure 2.8: (A) Temperature dependence of inverse susceptibility of $Gd@C_{82}$ [62] (B)Temperature dependence of the inverse integrated SQUID susceptibility of solvent free $Sc@C_{82}$ crystal for slow and fast cooling, indicating a unusual behaviour from 120 K to 200 K [63]

Comparing the magnetic properties of $La@C_{82}$ with $Gd@C_{82}$ Funasaka *et al.* [62] indicated that the inverse magnetic susceptibility, as a function of temperature,

followed the Curie-Weiss law, which was again consistent with a paramagnetic state. It is known that for La@C_{82} single crystals there is a structural transition between 140 K and 180 K [64], and there is a strange magnetic behaviour between 100 K and 200 K [62]. The correlation between the magnetic behaviour and structural transition of endohedral metallofullerenes had not been studied until recent work by Ito *et al.* [63], where the group applied similar methods to study solvent-free Sc@C_{82}. Different crystal structures were studied by varying the cooling process, through slow and fast cooling. They found that Sc@C_{82} possessed magnetic and structural phase transitions around 150 K, revealing an antiferromagnetic-like interaction. This behaviour amongst the Sc@C_{82} molecules restricts the molecular rotations, causing unusual magnetic susceptibility from 120 K to 200 K as shown in Figure 2.8B.

2.3 Carbon Nanotubes

The discovery of carbon nanotubes has been credited to early reports by Radushkevich (1952) [65] and Endo (1976) [66]. Carbon nanotube research maintained limited activity until Iijima (1991) [67] published details of an arc discharge process which resulted in carbon nanotubes to be produced on the negative end of the electrode, causing large interest in these novel nanomaterials. Iijima demonstrated electron micrographs of carbon nanotubes and resolved the structure through diffraction studies. Carbon nanotubes are a form of carbon with a hollow cylindrical structure and can exist as single walled (SWCNTs), double walled (DWCNTs) or multiwalled carbon nanotubes (MWCNTs), as shown in Figure 2.9.

SWCNTs can be produced from a number of methods, arc discharge, laser ablation, chemical vapour deposition (CVD), high pressure carbon monoxide (HiPCO)

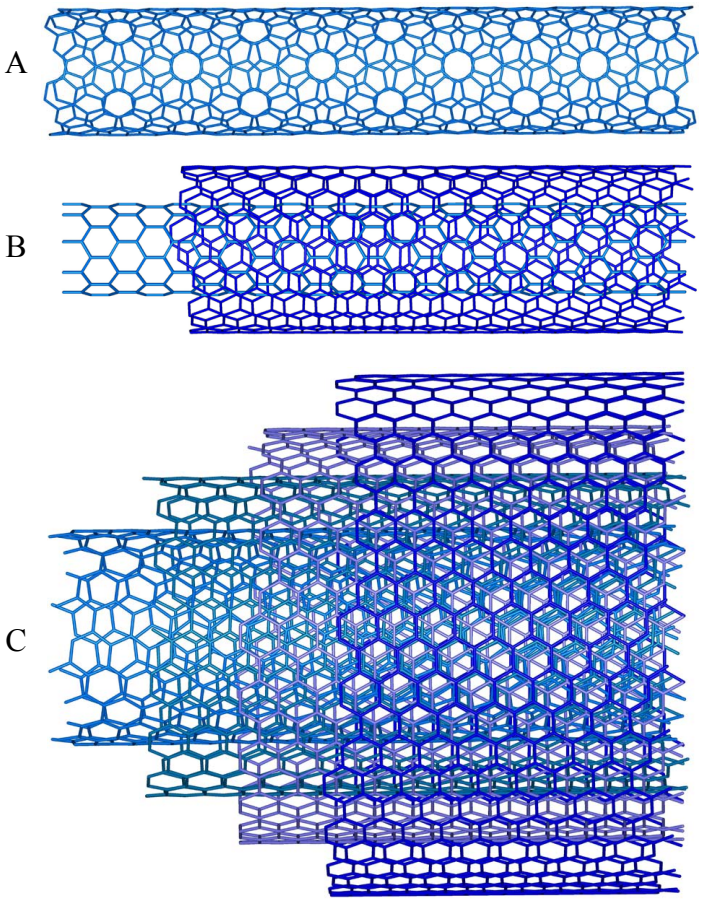


Figure 2.9: Schematic image of different nanotube structures (A) (10,5) SWCNT (B) [(9,0)(10,9)] DWCNTs and (C) [(12,8)(16,14)(20,19)(24,25)] MWCNTs

gas phase CVD and Co/Mo catalyst mixture (CoMoCat) CVD. The problems with most of these methods are the metal catalyst particle impurities, often magnetic, and other carbonaceous impurities. Another problem with current production techniques is the heterogeneous nature of the nanotubes, whether they are a mixture of single walled or multi walled, differences in length and diameter, and variation in chirality. These facts have hindered the understanding of the nanotube spin properties.

Nanotubes have potential applications in electronic field effect transistors (FETs) [68], composite materials, structural materials, sensors, drug delivery systems. By exploiting the novel hollow cylindrical structure of SWCNTs as an architectural material, the interior of the SWCNTs can be filled with spin active fullerenes, to form highly ordered 1D arrays of spins which could have potential application in spintronic devices. For any application in spin based technology it is important to understand the intrinsic spin properties of the SWCNTs and ensure that the SWCNTs are highly purified. There has be a drive to purify nanotubes to obtain cleaner higher quality samples, free from catalytic and carbon impurities, as well as developing techniques to separate nanotubes into semiconducting and metallic tubes, separating nanotube by diameter and separating nanotube by chirality.

2.3.1 Structure of Carbon Nanotubes

Carbon nanotubes can exist as SWCNTs or, by forming concentric cylinders, DWCNTs or MWCNTs, as illustrated in Figure 2.9. The structure of carbon nanotubes can be conceptualized as the rolling of graphene, a single layer sp^2-bonded carbon in a honeycomb lattice, to form a cylindrical structure with a hollow centre. Depend-

ing upon the direction in which the graphene is rolled up to form the nanotube the diameter and electronic properties of the SWCNTs will vary, as depicted in Figure 2.10. The direction in which the graphene is rolled is given by a chiral vector C_h. The chiral vector can be defined in terms of the carbon atoms in the graphene by a pair of integers (n,m) and a pair of lattice vectors (a_1,a_2);

$$C_h = na_1 + ma_2$$

The chiral vector of the nanotube determines the diameter of the nanotube, where the diameter, $d = C_h/\pi$. The value of (n,m) determines the electronic properties of the SWCNTs. If the CNTs have (n,0) then the nanotube is termed zig-zag, while if n=m, then the nanotube is termed arm-chair. Figure 2.10 illustrates chiral, arm-chair and zig-zag SWCNTs made from different (n,m) values. Semiconducting and metallic nanotubes depend on the values of (n,m). If $n - m = 3j$, where j is an integer, the nanotube is metallic, with all other values giving semiconducting nanotubes.

2.3.2 Carbon Nanotube Synthesis

Iijima [67] reported the synthesis of carbon nanotubes by an arc discharge, a similar process as that for producing fullerenes. The produced nanotubes contained a variety of multi-walled nanotubes, amorphous carbon impurities and catalyst particles. The demand for control over the produced carbon nanotubes has seen a number of production processes develop. Significant steps toward high quality nanotubes have been achieved, with the development of new production methods such as laser ablation, chemical vapour deposition (CVD), HiPCO and CoMoCat.

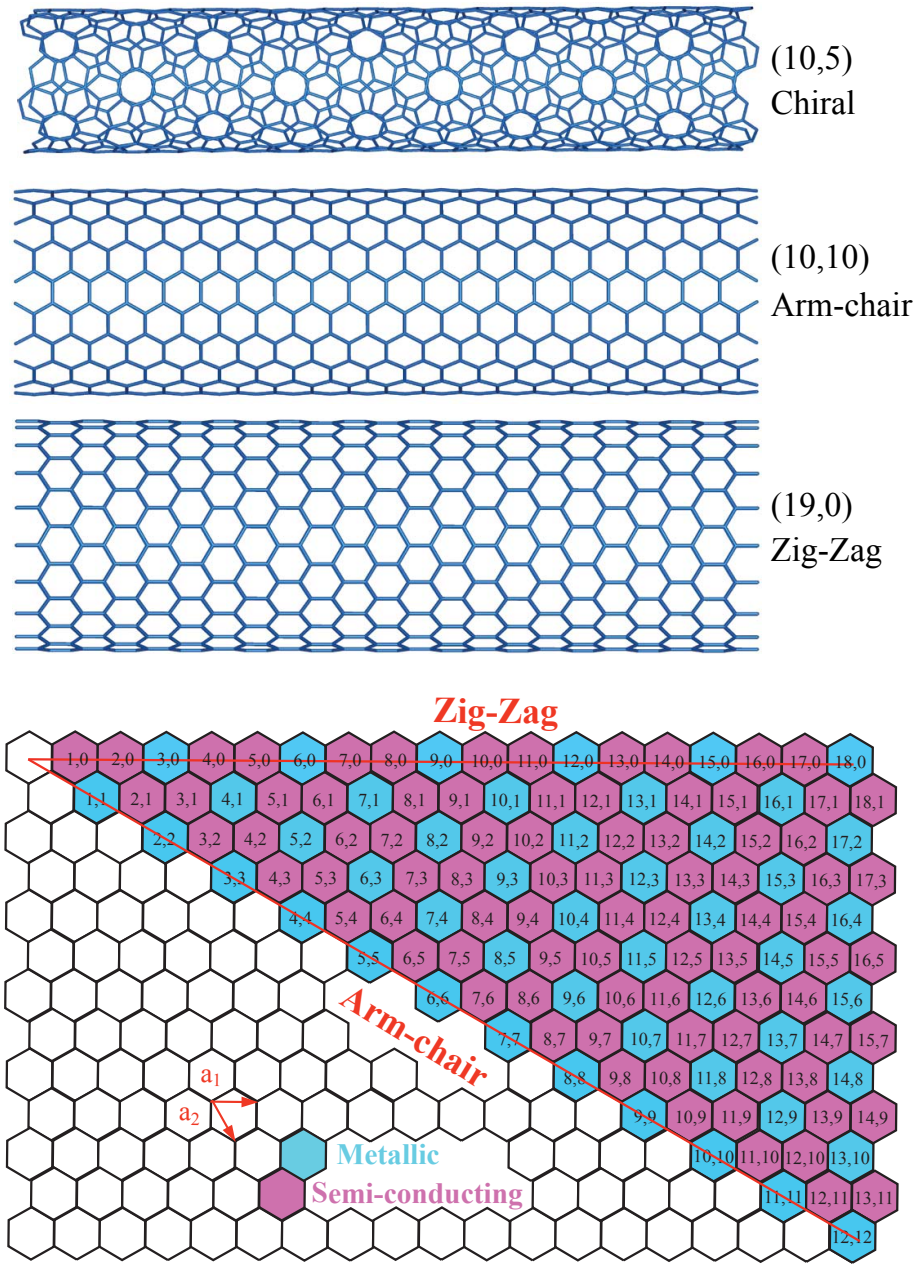


Figure 2.10: (*top*) A schematic image of a chiral (10,5), arm-chair (10,10) and zig-zag (19,0) single walled carbon nanotube (*bottom*) Conceptualized rolling of graphene sheet to form carbon nanotube, semiconducting nanotube are shown in purple and metallic nanotubes are shown in blue.

Arc Discharge

Arc discharge production of carbon nanotubes, used by Iijima [67] followed a similar process method to produce fullerenes. A voltage is applied between two graphite electrodes resulting in an arc striking the graphite electrodes, causing the graphite to vaporize and then re-condense to form carbon nanotubes. Arc synthesis also produces fullerenes but they do not contaminate the nanotubes as they are predominantly found in the soot produced from the arc and are removed by using a helium flow, while the synthesized nanotubes are deposited on the cathode. Iijima's production method offered limited control, producing both single walled and multi-walled nanotubes. Early nanotube production of SWCNTs via arc discharge suffered due to their poor yields [69], however using various catalyst particles proved critical towards large scale production [70]. Metal catalysts such as Co [69], Fe [71] or Ni [72] or metal catalyst mixtures, Fe/Ni or Ni/Co [73], or combined with rare earth metals, Ni/Y [74], have been implemented into the cathode to improve the overall yield and offer control over the SWCNTs diameter. Another experimental factor which affects the diameter of the produced nanotubes is the background pressure of the helium argon gases [75]. The diameter distribution is dependent on the argon helium mixture, as the ratio of the gases affects the thermal conductivity and diffusion coefficients, thereby controlling the condensation of carbon and metal catalyst particles around the cathode.

Laser ablation

Thess *et al.* [76] developed an alternative method to produce carbon nanotubes using a laser to ablate a graphitic source. Using a combination of graphite and

metal catalysts Co/Ni, laser ablation production methods offered high yields, with approximately 70-90% conversion of graphite into carbon nanotubes. The graphite catalyst mixture was heated to 1200 °C using a furnace with an argon flow. Employing a laser pulse to strike the graphite catalyst mixture causes the atoms to vaporize and then the atoms condense and nanotubes grow from the catalyst particles. The argon gas flow causes the nanotubes to move from high temperature region and collect on the copper cold tip. Nanotubes produced from laser ablation form nanotube bundles, held together by weak van der Waals interactions.

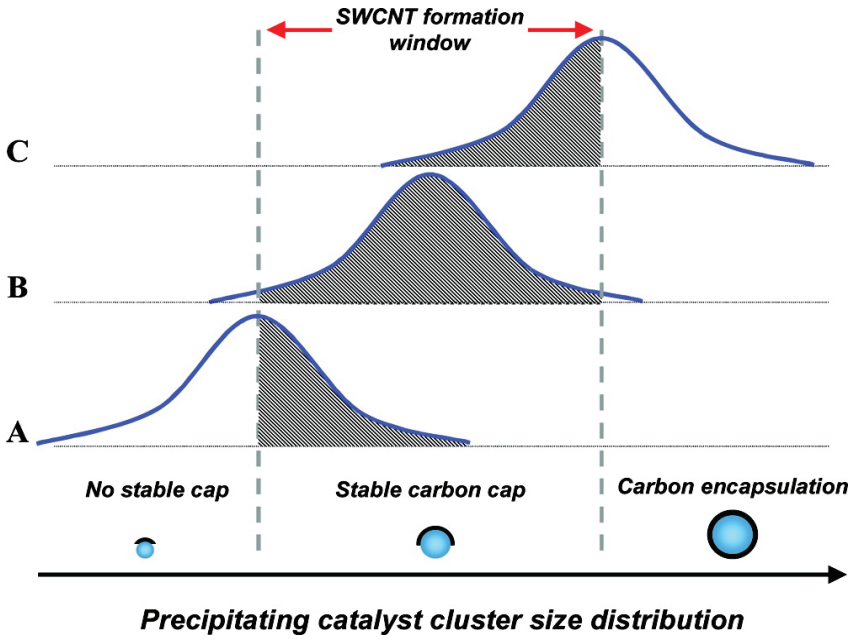


Figure 2.11: Schematic diagram showing the growth mechanism proposed by Rümmeli *et al.* [77]. The precipitating catalyst particle cluster size distribution varies with oven temperature, increasing from A-C. SWCNTs are only formed in the overlap (shaded region) between the precipitating catalyst size distribution and SWCNTs growth window, as indicated by the shaded are. The degree of overlap will determine the SWCNT mean diameter and diameter distribution [77]
Reprinted with permission from: Rümmeli, M. H. et al. (2007) 'Catalyst volume to surface area constraints for nucleating carbon nanotubes', J. Phys. Chem. B, 111(28): 8234-8241. © 2007 American Chemical Society

A growth mechanism for SWCNTs by laser ablation proposed by Rümmeli [77]

suggests a catalyst volume to surface area model. After the laser has ablated the graphite and the catalyst, the carbon atoms and catalyst particles will cool and the carbon atoms will precipitate on the catalyst surface. For a carbon nanotube to grow the precipitated sp^2 carbon is required to form a stable hemispherical cap and grow cylindrically from the catalyst particle. DFT calculations [78] emphasised the importance of the formation of a stable hemispherical carbon cap for nanotube nucleation to occur. The formation of a stable hemispherical cap is dependent upon the size of the catalyst cluster. If the catalyst is too small the cap will be unstable and the catalyst particles are likely to coalesce, while if the catalyst is too large then multiple sp^2 carbon structures will form, coalescing together to make a carbon shell surrounding the catalyst particle. Therefore a distribution of precipitating catalyst cluster size allows for successful SWCNT formation, as illustrated in Figure 2.11, which leads to control over the mean diameter and diameter distribution. The amount of carbon which precipitates onto the catalyst particle before the point of nucleation is also important and will depend on the carbon solubility of the catalyst particle. Varying the temperature of the system can be used to control the diameter distribution as the the temperature affects the catalyst cluster size distribution. The growth mechanism of SWCNTs using mixed catalyst, has been an effective route to higher yields and can also be explained through the nucleation window of carbon nanotubes [79]. Using a mixture of catalyst particle alters the catalyst particle size distribution, maximizing the formation of the hemispherical cap during the nucleation window allows for improved nanotube yields.

Chemical Vapour Deposition

Chemical vapour deposition (CVD) offers a scalable and controllable approach to produce carbon nanotubes for certain applications. A carbon precursor source, such as methane [80], carbon monoxide [81] or ethylene [82], is heated to elevated temperatures until it decomposes, allowing the nucleation of the free carbon atoms, using metallic nanoparticles as a catalyst, to form carbon nanotubes, illustrated in Figure 2.12A. Varying the diameter of catalyst $FeCl_3$ nanoparticles [83], deposited on a silicon substrate, changes the diameter of the produced nanotubes, allowing for controlled growth. The original production method has seen several high profile developments, such as super growth, HiPCO and CoMoCAT to improve the yield, purity and scalability of carbon nanotube growth.

To counter the problem of impurities produced during CVD, Hata *et al.* [84] developed a method to use a weak oxidiser, water, to assist in the removal of amorphous carbon and not damage the nanotube structure. Amorphous carbon can hinder nanotube growth by covering the catalyst surface reducing its activity and there by reducing the overall nanotube production. Using an ethylene carbon source, controlled amounts of water vapour showed enhancement of catalyst activity and resulted in large growth of vertically aligned nanotube forests with heights of up to 2.5 mm, as shown in Figure 2.12B. The SWCNT forest could be easily lifted off the substrate, leaving the catalyst embedded on the substrate, allowing nanotubes to be produced with a purity of up to 99.98%. The high purity, magnetic free samples can be produced on a large scale and offer a potential solution to SWCNTs application demand.

One of the most promising large scale nanotube production methods is HiPCO

gas phase CVD [85], which has the potential to produce nanotubes on the kilogram per day scale. HiPCO differs from conventional CVD as the entire process is conducted in the gas phase. Using high pressure, 30-50 atm, and high temperature, 900-1100 °C, CO and Fe are fed through the gas flow. The Fe particles will react with CO to form a $Fe(CO)_5$ complex, which will decompose under high temperatures, causing Fe particles to cluster together. These Fe clusters act as catalyst centres allowing the CO molecules to react together releasing CO_2 and allowing C to nucleate and form SWCNTs. The concentration of CO_2 produced by the reaction is equal to that of carbon and can therefore serve as a useful real-time feedback parameter. The produced SWCNTs contain large quantities of Fe catalyst particles, which will require some purification to remove these impurities. HiPCO SWCNTs have a small diameter distribution, around ∼1 nm, limiting their potential for any filling experiments to produce peapod structures, where a minimum nanotube diameter of at least ∼1.35-1.4 nm is required to exothermically fill $La@C_{82}$[86].

The process has been adapted using a heterogeneous Co/Mo catalyst mixture, CoMoCat [88], performed at a lower temperature between 750 and 900 °C, and produces SWCNTs of high quality. A scalable approach [89] has been developed to allow large scale production of SWCNTs. The process has been shown to have significant control over the produced nanotubes [87], as illustrated in Figure 2.12C, varying the temperature will increase the diameter size but will maintain the same chiral angle. While changing the support from SiO_2 to MgO will keep the diameter consistent but vary the chiral angle. As with HiPCO nanotubes the diameter distribution, between 0.7 and 1.3 nm, of CoMoCat nanotubes is too small for any filling and limit their potential use for making peapods.

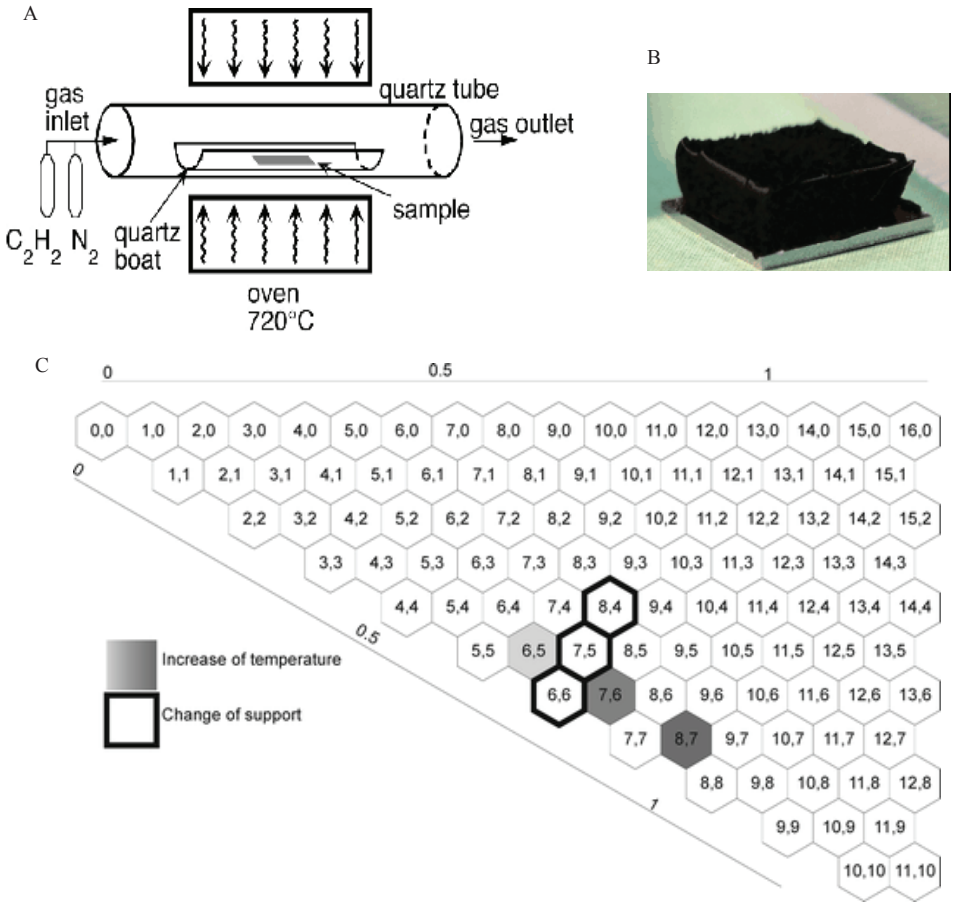


Figure 2.12: (A) Schematic design for the CVD process (B) Picture of a 2.5-mm-tall SWCNT forest on a 7-mm by 7-mm silicon wafer [84] (C) (n,m) map showing the affects of temperature and support morphology on the produced SWCNT [87].

2.3.3 Purification of Carbon Nanotubes

The synthesis of carbon nanotubes often produces impurities. These include carbon based forms, such as fullerenes, amorphous or graphitic carbon, as well as metal catalyst particles, which can be clustered or surrounded by carbon shells. Synthesis procedures have improved nanotube yields and scalability, but they are still hindered by the impurities which contaminate the nanotubes. For successful application it is

essential to have a high purity SWCNT source, therefore there is a need to purify the raw material to remove these impurities. The multiple synthesis methods produce nanotubes with a variety of diameters, lengths, carbon impurities and use a range of catalysts. Therefore a range of purification schemes have been developed, each suited to purify nanotubes from a specific source. In most cases a combination of purification techniques are implemented to achieve the best results. Purification methods have been primarily developed using either chemical treatment of the nanotube or physical removal of impurities.

Chemical treatment

Metal catalyst nanoparticle impurities are often encased by a graphitic carbon shell making them impervious to acid treatments. To facilitate removal of metal catalyst particles it is essential to initially remove carbon impurities, which would then allow acid treatment to purify the nanotubes. Chiang [90] studied the effects of oxidative annealing, where raw carbon nanotubes were heated in air between 300-500 °C oxidising the amorphous carbon species and removing the impurities.

Oxidative annealing results in the removal of the carbon shell surrounding catalyst particles leaving them exposed to acid treatment. Acid treatments using either nitric [91] or sulphuric acid, have been successfully demonstrated to remove catalyst particles. The drawback of using harsh acid treatments is the formation of defects in the nanotube structure and creation of functionalized carboxylic groups on the nanotube. An alternative treatment process has been developed, particularly for Pt catalyst grown SWCNT, uses microwave digestion in conjunction with an aqua regia treatment [92]. Microwave digestion heats the metal catalyst particles, causing them to expand and break the surrounding carbon shells, while aqua regia treatment

offers a method to remove catalyst particles which are resistant to individual acid treatments.

Physical treatments

Physical methods have been developed to help remove these impurities while countering the need for harsh chemical treatment. Filtration of nanotubes is a non-destructive purification method, but has achieved limited success [93] due to limited ability to differentiate nanotube sizes and difficulty in acquiring high purity samples without continuous repetition. Size exclusion chromatography of SWCNTs, wrapped by surfactants [94] or DNA [95], has effectively removed impurities and allowed length separation for both MWCNTs and SWCNTs. Specifically for CVD super-growth nanotubes [84] mechanical cutting of the nanotube from the catalyst substrate yielded nanotubes absent from catalyst particles, which remain attached to the substrate. Centrifugation offers a potential route to purifying SWCNTs [96], low centrifuge speeds have been demonstrated to separate amorphous carbon while high centrifugal speeds can effectively separate out heavy catalyst particles leaving a SWCNTs aqueous suspensions. The process shows potential in producing high purity samples, up to 90%, and can be used to perform large scale purification of SWCNTs.

2.3.4 Towards Carbon Nanotubes Homogeneity

The heterogeneous production of carbon nanotubes severely limits many potential applications, where homogeneous nanotubes are required. Current synthesis methods all produce a variety of nanotubes which may vary in diameter, length, chirality and the number of walls. To approach this problem there are two potential solu-

tions; modify current synthesis methods to selectively produce specific nanotubes or devise post production processes that enable selective sorting of nanotubes. Specific applications such as a field effect transistor require semiconducting nanotubes and nanoscale interconnects require metallic nanotubes. The demand of separated semiconducting and metallic nanotubes has seen much focus on developing novel separation techniques.

Li *et al.* [97] demonstrated an improved CVD setup using combined catalysts FeRu to produce nanotubes with a narrow diameter and (n,m) chirality distribution, producing predominantly semiconducting nanotubes with chirality (8,4), (7,5) and (7,6). Combining the process with ion exchange chromatography they developed a procedure to selectively secure single chirality (8,4) nanotubes. CVD using a solid support catalyst of Co nanoparticle [98] produced SWCNTs with narrow diameters and with chiral angles near the arm-chair limit, predominantly (6,5) and (7,5) nanotubes. Selective growth of semiconducting SWCNTs has been successful with a proposed strategy of using plasma enhanced CVD which preferentially produced semiconducting SWCNT of up to 96%, compared to the control of HiPCO, 61%, and laser ablation, 70% [99, 100, 101]. The proposed production methods offer routes to producing separated nanotubes, but the relative purity and yield are currently low. With an emphasis on optimising the CVD process the separated nanotube will have a narrow diameter and therefore be unable to encapsulate the fullerene to forms peapods.

Various purification methods have been explored to either isolate nanotubes by chirality or separate nanotubes into electronic forms. Krupke [102] separated metallic and semiconducting nanotubes using di-electrophoresis, shown in Figure 2.13A, where a electric field is applied to a solution of SWCNTs and due to the different

dielectric constants, relative to the solvent, metallic SWCNTs move towards an electrode array, while the semiconducting SWCNTs remain in the solvent. There has been a drive to use molecules or systems which bind preferentially to semiconducting or metallic nanotubes as a method of separation. DNA wrapping [103] of carbon nanotubes, through π -stacking, improved dispersability of the nanotubes, showing selectivity for certain nanotube species as demonstrated in Figure 2.13B. Further studies have provided a technique to use different DNA sequences [104] to selectively isolate specific nanotube chirality. Figure 2.13C illustrates an (8,4) SWCNT wrapped by a DNA sheet, sequence $(ATTT)_3$, produced with 90% purity. Using macromolecules to aid selectivity has highlighted the use of aromatic polymers [105] and flourene based polymers [106]. In each case the polymer based systems can be modified to selectively isolate different chiral nanotube species.

Alternative to DNA and macromolecules, SWCNTs have also been dispersed in surfactants such as sodium dodecylbenzene sulphonate (SDBS), sodium dodecyl sulphate (SDS) or sodium cholate (SC). The surfactants coat the nanotube surface allowing dispersability in an aqueous solution, which is otherwise limited by the hydrophobic nanotube surface. Sonication further increases the dispersability of nanotubes in the aqueous surfactant solutions. Centrifugation of the aqueous SWCNTs solutions has been demonstrated to separate isolated nanotubes from nanotube bundles. A promising separation technique involves the use of surfactants to make well dispersed isolated solutions and then employing density gradient centrifugation to separate nanotubes by diameters and chirality. Arnold *et al.* [107] demonstrated that the differences in buoyant densities could be utilized to separate out nanotubes by diameter and chirality by using density gradient ultracentrifugation (DGU). Under ultracentifugation the SWCNTs will settle at a point where their density matches

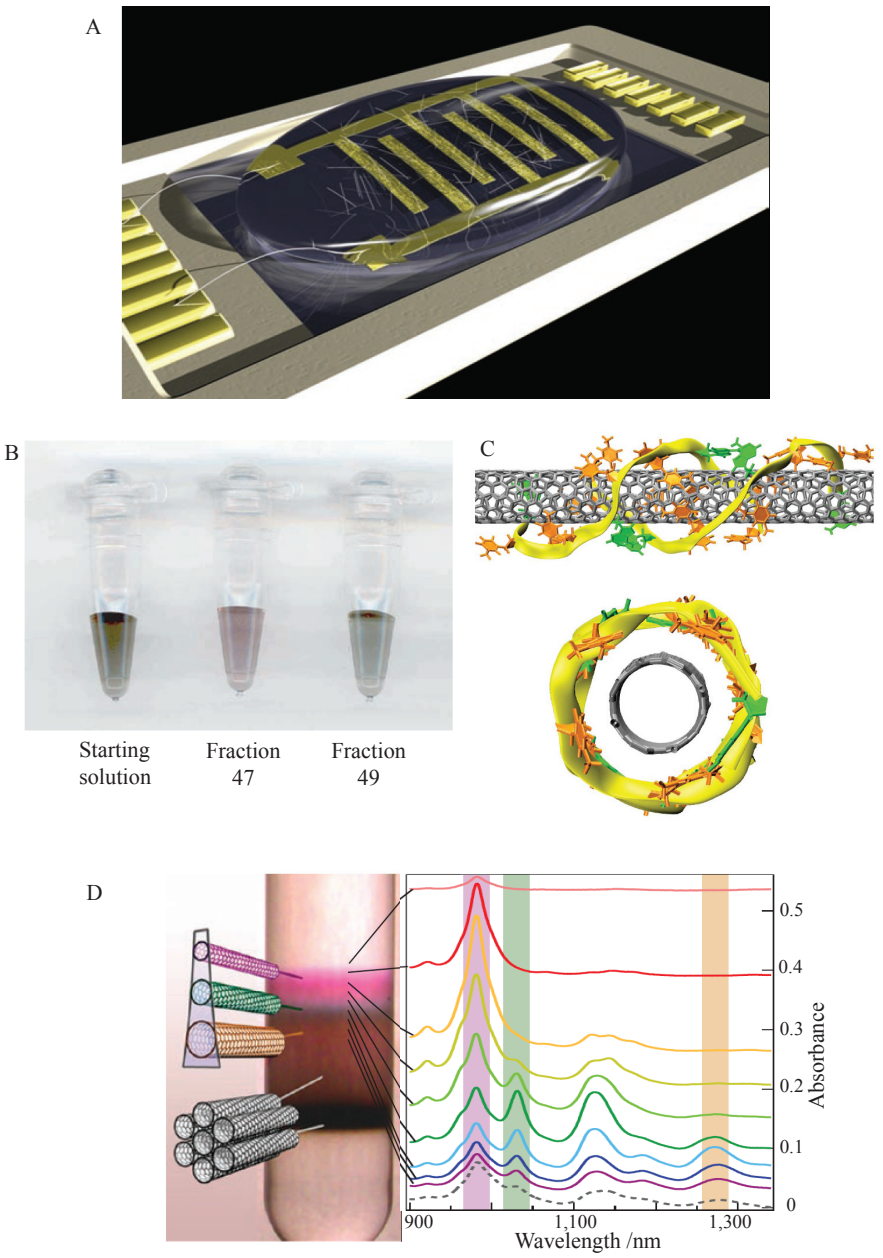


Figure 2.13: (A) Schematic of dielectropheresis of SWCNTs [102] (B) Ion exchange chromatography of DNA wrapped SWCNTs showing visible colour differences between samples [103] (C) (8,4) SWCNT wrapped by a DNA sheet ($ATTT_3$ sequence) [104] (D) Density gradient ultracentrifugation scheme for small diameter nanotubes encapsulated in SC, resulting in isolated smaller diameter nanotubes forming in the supernatant, while nanotube bundles aggregate to the bottom [107]

the density of the gradient, resulting in layering of SWCNTs depending upon their buoyant density. Using a single surfactant or a combination of surfactants has shown the separation of nanotubes by diameter and chirality, as shown in Figure 2.13D. Surfactants [108], SC and SDS, have inequivalent binding energies to SWCNTs and depending on electronic type resulted in the observed differences in buoyant density. Advancements of the original DGU process have enabled 99% pure separated samples to be produced. Applying the process to a variety of SWCNTs, produced from different production methods, have allowed a range of colours of nanotube solutions to be produced, as the optical properties of the SWCNT depend on the diameter and chirality [109]. Further advances have explored self generating density gradients [110], which have demonstrated high efficiency separation, while enabling a larger SWCNT volume to be separated compared to the original process.

2.4 Peapods

Single walled carbon nanotubes (SWCNTs) possess the ability to encapsulate atoms or molecules inside the available hollow interior and to form new hybrid systems. Incorporation of fullerene molecules inside nanotubes was first observed by Smith *et al.* [111]. These new materials, an example shown in Figure 2.14 have been commonly termed as 'peapods'. Since their initial discovery, peapods have received attention due to their unique structure and chemical and physical properties. Peapods possess novel properties, due to the encapsulation of fullerene molecules inside the nanotube. Incorporating endohedral metallofullerenes is one of many lines of research based upon the filling of SWCNTs. The nomenclature [112] used to express these hybrid materials is X@SWCNTs, where X is an atom, molecule or chemical

compound. One of the most interesting design feature of peapods are that SWCNTs provide a unique 1D architecture for the filled material, which facilitates control over the ordering of the encapsulated material as well as having the potential to conduct chemical reactions [113].

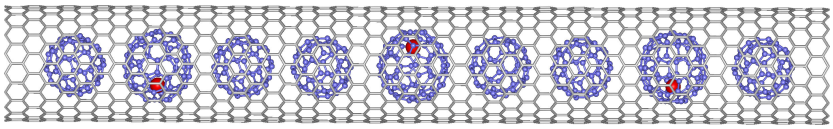


Figure 2.14: Schematic of $Sc@C_{82}$:C_{60} filled inside a (18,0) SWCNT

2.4.1 Synthesis of Peapods

C_{60} peapods, first observed by Smith *et al.* [111], were synthesized via pulsed laser vaporization of graphite in the presence of metallic catalysts, producing both carbon nanotubes and C_{60} molecules. High resolution transmission electron microscopy (HRTEM) images indicated that the majority of the carbon nanotubes were empty, but chains of C_{60} were observed in some carbon nanotubes with around 5% filling. Significant progress towards encapsulation of SWCNTs has seen a number of production methods; hot vapour gas filling, liquid phase filling and super-critical fluid filling. SWCNTs can be grown to have diameters ranging from 0.7 - 2.0 nm, allowing a wide variety of molecules to be encapsulated. Molecules will require enough kinetic energy to move to the open end of the SWCNTs and pass through a small energy barrier to enter the hollow interior of the nanotube. Depending upon the relative diameters of the SWCNT and the fullerene the encapsulation process can be exothermic [114, 115], with the endohedral metallofullerenes being stabilized upon entering the SWCNT by van der Waals interactions. The synthesis of peapods may

not be limited to using just carbon SWCNTs. Novel theoretical calculations show that boron-nitride SWNTs would encapsulate La@C_{82} and La_2@C_{80} [116].

Hot Vapour gas filling

Gas-phase reactions have been commonly used to produce high-yield synthesis of peapods. Open-ended SWCNTs and isolated fullerenes are placed in quartz tubes under vacuum, then thermally treated, for a period of 4 - 5 days, allowing fullerenes to sublime and migrate inside the SWCNT. There are a number of factors to consider in order to optimize the filling level of the peapods. SWCNTs should be purified and open-ended, as amorphous carbon and other impurities can prevent filling of fullerenes. As the sublimation temperature of fullerenes are low ($\sim$ 350 °C) a temperature of 400 - 600 °C is sufficient enough to facilitate filling. It has been shown [117] that filling of 100% can be achieved using the synthesis method. This method is very effective for most empty caged fullerenes and endohedral metallofullerenes, but ineffective for other encapsulated or functionalized fullerenes, e.g. N@C_{60}, due to their low thermal stability.

Liquid phase filling

Solution phase filling of SWCNTs allows molecules which are thermally unstable, non-volatile or functionalized to be encapsulated. SWCNTs are immersed in a concentrated solution of fullerenes with the solvent transporting fullerene molecules inside the nanotube. To achieve a high level of filling the solvent should have minimal interactions with the fullerene and the SWCNTs. A variety of solvents have been studied with the aim to improve the yield of encapsulated SWCNTs. Hexane has been successfully demonstrated to produce C_{60}@SWCNT and N@C_{60}@SWCNT

[118] and funtionalized fullerene [119] peapods. Other organic solvents have been ineffective with Khlobystov *et al.* [120] suggesting that using aromatic organic solvents for encapsulation results in a filling of $\sim 1\%$, with HRTEM showing that the surface of the nanotube is contaminated with solvent impurities. Due to the difference in molar concentrations of C_{60} and the solvent, the solvent being around 1000 greater, the nanotube will be largely filled with solvent. The solvents studied were determined to have insufficient diameter to diffuse between the fullerene and the inner wall of the nanotube, represented in Figure 2.15A. As a result the only other diffusion route is via defect sites on the side wall of the nanotube. To maximize the filling with solvents it is important to use SWCNTs of large diameter or with defective side walls, encouraging the diffusion of solvent molecules out of the nanotube.

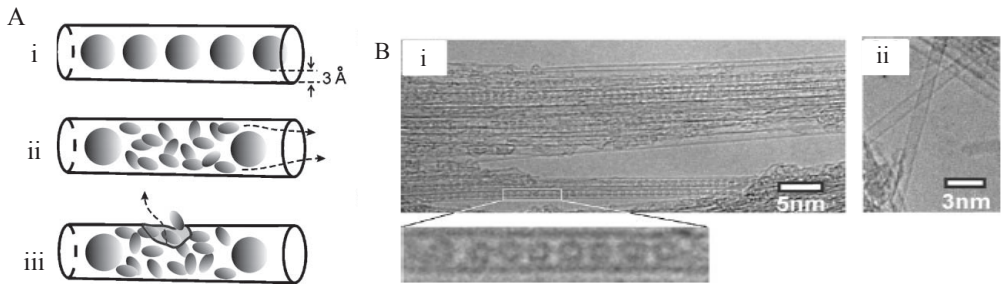


Figure 2.15: (A) Schematic diagram of filling (i) Regular peapod structure with van der Waals separations between C_{60} molecules (ii) Partially filled nanotube with C_{60} and solvent molecules, the solvent molecules diffuse between the fullerene and the inner wall (iii) Partially filled nanotube with C_{60} and solvent molecules, with the solvent molecules diffusing through defect sites on the side wall of the nanotube. Spheres represent C_{60} molecule, ellipses represent solvent molecules [120]. (B) HRTEM images of (i) SWCNTs of diameter 14.9 Å filled with C_{60} in $scCO_2$ at room temperature. (ii) SWCNTs of diameter 13.6 Å remain empty under $scCO_2$ filling conditions [120]

Supercritical fluid filling

Low temperature filling can also be achieved by using supercritical fluids (SCFs) rather than organic solvents. The majority of work conducted in this area has been produced by Khlobystov *et al.* [120], with the motivation of using SCFs because they possess a higher level of diffusivity compared to organic solvents. Carbon dioxide, which has a critical temperature of $T_c = 31\,^{\circ}\mathrm{C}$, is a suitable SCF for volatile fullerenes, allowing synthesis of peapods to be carried out at ambient temperatures. $ScCO_2$ has a very low critical diameter, compared to other organic solvents such as ethanol or toluene [120], allowing the CO_2 molecules to pass through the fullerene-sidewall gap. This method of filling is ideal for functionalized fullerenes or volatile fullerenes as the synthesis is performed at ambient temperatures. As with liquid phase filling the level of fullerene encapsulation is dependent upon the diameter of the SWCNT host. HRTEM images shown in Figure 2.15B show the effect of different diameter tubes upon filling, the narrow 13.6 Å diameter nanotubes are almost empty, where as the wider 14.9 Å diameter tubes are largely filled [120].

2.4.2 Structure of Peapods

Peapods have a unique structure where a 1-dimensional array of fullerenes are formed inside a SWCNT without covalent interactions [121, 122]. HRTEM and XRD, are useful analytical tools to measure the level of filling in peapods. HRTEM imaging provides structural information about the packing of fullerenes inside nanotubes and can also reveal molecular motion in real time. HRTEM is fundamental for the study of peapods as it clearly indicates whether fullerene molecules are encapsulated inside the SWCNT, as shown in Figure 2.16A.

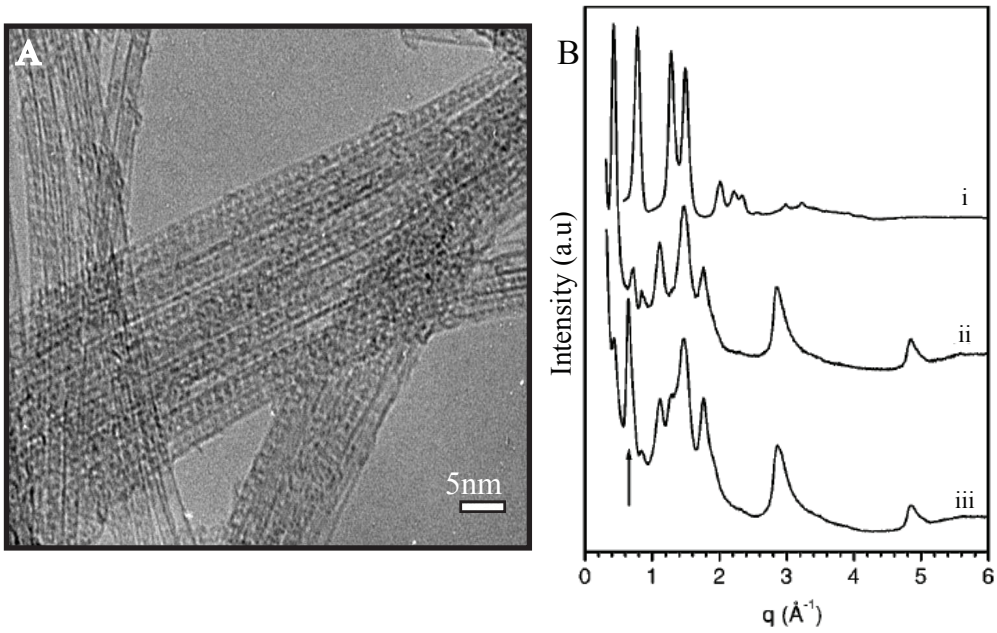


Figure 2.16: (A) HRTEM image of C_{60} peapods showing high filling of nanotubes (B) XRD of (i) C_{60} (ii) Empty SWCNTs (iii) C_{60}@SWCNT. The arrow indicates the momentum transfer of $q = 0.65$ Å^{-1} corresponding to a inter fullerene distance of 0.97 nm [123]

Prolonged exposure can result in beam irradiation causing damage to both the fullerene and the SWCNT. Recent studies have shown that using a low accelerating voltage of 80 kV can reduce the knock-on damage to the SWCNT [124] and its has also been demonstrated that the stability of SWCNTs against exposure to accelerated electrons increases with the diameter of the nanotube [125].

XRD has been used to measure the filling ratio for the bulk sample of C_{60} peapods [126], which can be more accurately determined than using HRTEM. It can also determine the inter-fullerene separation. For C_{60} this has been determined to be around 0.97 nm, as demonstrated in Figure 2.16B. This separation is slightly less than that of C_{60} crystals, indicating that the encapsulation inside the SWCNT has

influenced fullerene interactions and reduced the inter-fullerene distance.

2.4.2.1 Ordering and Orientation of Peapods

In bulk fullerene crystals each fullerene will have 12 nearest neighbours in a face centred cubic closed packed arrangement. Fullerenes encapsulated inside a SWCNT will form a linear chain and have only 2 nearest neighbours. Theoretical [127] and experimental [128, 129] studies highlight possible ordering arrangements of fullerenes in SWCNTs. With increasing nanotube diameter fullerene molecules can form new arrangements within the nanotube. For C_{60}, zig-zag, double helix and a two molecular layers have been identified, as shown in Figure 2.17A, with a total of 10 possible arrangements theoretically calculated.

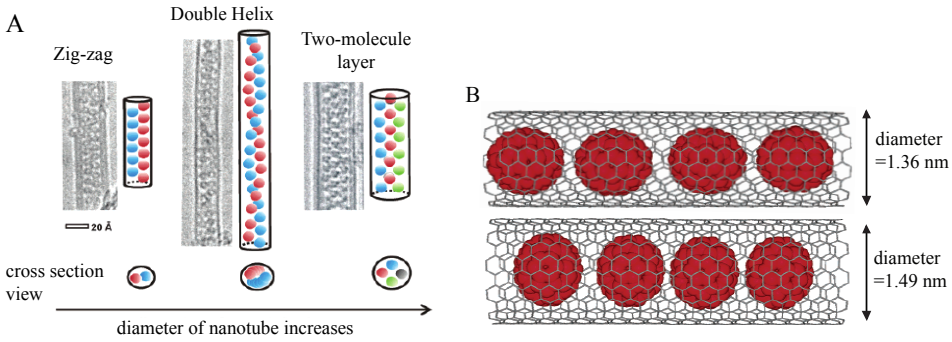


Figure 2.17: (A) Different phases of C_{60} assembled in carbon nanotubes of different diameters [128] (B) Structural diagrams shown longitudinal (top) and traverse (bottom) orientations of C_{70}[130]

The orientation of fullerenes inside nanotubes is dependent upon fullerene size and the endohedral nature of the fullerene. Peapods of C_{70}, which have an ellipsoidal structure, shown in Figure 2.17B, have two distinct orientations [130]. C_{70} molecules can have a longitudinal orientation in narrow nanotubes or have traverse orientation in wider nanotubes. The orientation of endohedral metallofullerenes

varies due to the asymmetric charge distribution within the fullerene cage. Endohedral metallofullerenes possess electric dipole moments which affects their molecular orientation inside the nanotubes. HRTEM observed the different orientations of the endohedral metallofullerenes molecules, as the metal dopant showed increased contrast, as indicated in Figure 2.18. HRTEM images of Ce@C_{82}@SWCNT [129] and La@C_{82}@SWCNT [131] peapods, shown in Figure 2.18A/B, indicate that metallofullerenes preferentially orientate their dipole axis along the nanotube axis to maximise electrostatic interactions between neighbouring molecules.

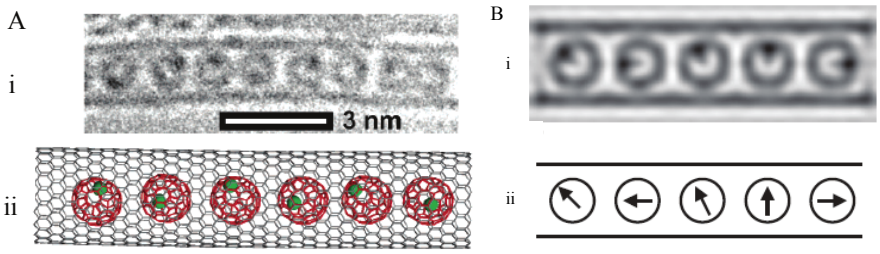


Figure 2.18: (A) (i) HRTEM image of Ce@C_{82} peapods, with the dark spot corresponding to the Ce atom (ii) Schematic diagram of the peapod structure [129] (B) (i) HRTEM model of La@C_{82} molecules inside SWCNT, with the dark spot corresponding to the La atom. (ii) Deduced dipole orientations for each molecule [131]

2.4.3 Properties of Peapods

Upon encapsulation of metallofullerene molecules inside the hollow interior of SWCNTs the properties of both the metallofullerene species and the SWCNTs will be perturbed, due to effects such as possible charge transfer between metallofullerene and SWCNTs and the mechanical strain of the inserted metallofullerenes. Several experimental studies have been conducted towards understanding the electronic, transport and structural dynamics of metallofullerene peapods.

2.4.3.1 Electronic Properties of Peapods

Energy electron loss spectroscopy (EELS) has been employed to study the valence state of the metal atom and to indicate the amount of charge transfer that occurs between the metal atom to the fullerene cage and the SWCNT. EELS measurements performed on $Gd@C_{82}$ metallofullerene peapods [132] were compared to a bulk sample of $Gd@C_{82}$. The Gd M_{45} absorption edges of both samples, shown in Figure 2.19A were very similar, with peaks at 1184 and 1214 eV, indicating that the valence state of the Gd peapod sample is the same as the Gd^{3+} of the bulk fullerene sample. Through EELS experiments it was determined that encapsulation of metallofullerenes inside SWCNTs does not alter the valence state of the metal atom.

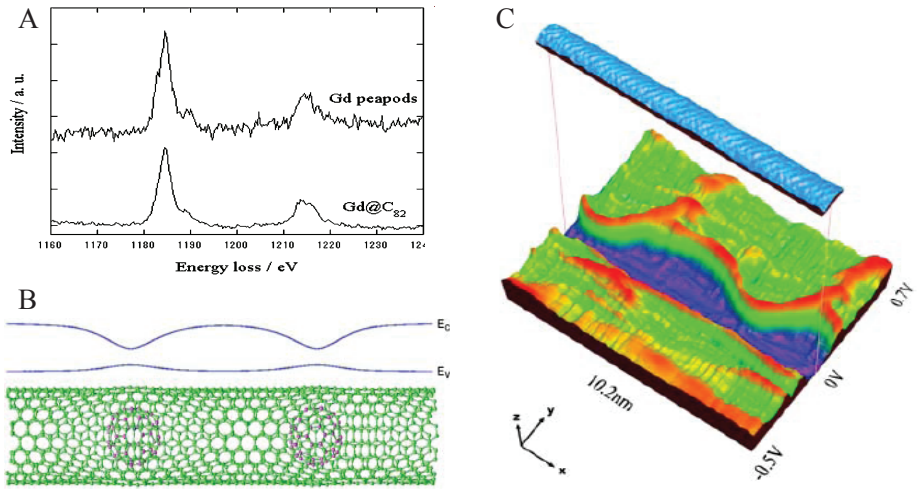


Figure 2.19: (A) EELS spectra of $Gd@C_{82}$@SWCNT bundle and Gd^{3+} in $Gd@C_{82}$. The M_{45} absorption edges are clearly observed for both species. (B) Illustration of two $Gd@C_{82}$ endohedral metallofullerenes in a (11,9) SWCNT, including a schematic representation of the modulation of conduction and valence bands (C) (top) 3D topograph of 10.2 nm length (11,9) SWCNT containing $Gd@C_{82}$. (bottom) Corresponding $\mathrm{d}I/\mathrm{d}V$ spectrum along the tube showing spatial variation. The x-axis indicate the position of the tube, the y-axis shows the energy and the z-axis shows $\mathrm{d}I/\mathrm{d}V$, decreasing from red to green to blue [132, 8]

Low temperature scanning tunnelling microscopy (STM) and spectroscopy (STS) [132, 8] has revealed that the encapsulation of metallofullerene significantly affects the electronic structure of SWCNTs. It has been considered that the band gap of semiconducting SWCNTs could be altered by the insertion of metallofullerene molecules, as illustrated in Figure 2.19B. The spatial variation of the local density of states, $\mathrm{d}I/\mathrm{d}V$, along the tube axis, at a temperature of $\sim$5 °C, is shown in Figure 2.19C. The STM image shows two Van Hove singularity (VHS) peaks, corresponding to conduction and valence band edges, and from the VHS peaks it is possible to evaluate the local band gap, with the original SWCNT band gap, 0.43 eV, narrowed to 0.17 eV where the fullerene is believed to be located. The change in band gap is due to a combination of charge transfer at metallofullerene sites within in SWCNT and elastic strain [8]. The possibility to control the distance between metallofullerenes can lead to changing the shape of the potential well for the electron and holes and offers band gap engineering. This result conflicts with the EELS measurements, which indicated no observable charge transfer, suggesting there is no definite conclusion regarding the nature of charge transfer between the metallofullerene and the SWCNT.

Although there has been extensive work regarding the EPR of metallofullerenes in solutions or solid crystal, there has been limited reported work about the EPR of metallofullerene peapods. Jakes *et al.* [133] reported a temperature study of the EPR spectrum of La@C_{82} peapods, revealing loss of hyperfine structure, with the authors suggesting that this occurs due to the charge transfer between the fullerene cage and the SWCNT. EPR studies of N@C_{60} and N@C_{70} peapods [134] revealed the typical three peaks seen for a N@C_{60} with significant line broadening. In N@C_{60} the spin is retained on the nitrogen atom and not transferred to the fullerene cage,

hence the nitrogen hyperfine is still detected upon encapsulation inside the nanotube. For spin active metallofullerenes the exact nature of the metallofullerene spin upon encapsulation still remains unclear. One of the key practical issues in the EPR study of peapods is the necessity of highly pure SWCNTs free from amorphous carbon impurities and magnetic catalyst particles.

2.4.3.2 Transport Properties of Peapods

The transport properties of peapods have been examined by measuring the field effect transistor (FET) characteristics of the metallofullerene peapods. Compared to single bundles of SWCNT-FET, which are *p*-type and dominated by hole transport, peapod-FETs have shown an ambipolar behaviour. The ambipolar behaviour has been identified for both fullerene and metallofullerene peapods.

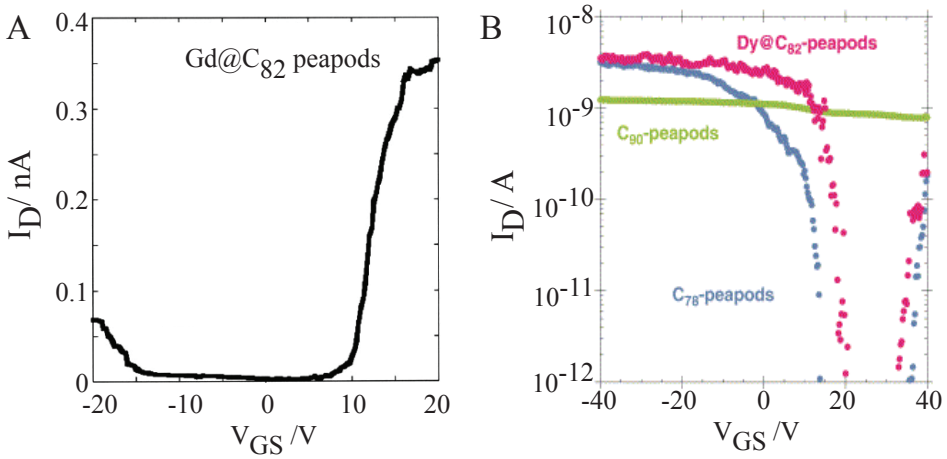


Figure 2.20: I_{DS} - V_{DS} curves at V_{DS} = 20 mV for (A) Gd@C_{82} peapod FET (B) C_{90}@SWCNT, C_{78}@SWCNT and Dy@C_{82}@SWCNT FETs and T = 23 K [135, 136]

Figures 2.20A and B show the I_{DS} -V_{DS} curves for Gd@C_{82}@SWCNT [135], C_{90}@SWCNT, C_{78}@SWCNT and Dy@C_{82}@SWCNT FETs [136]. C_{90}@SWCNT

FETs demonstrates metallic behaviour without a zero-conduction region, while Gd@C_{82}@SWCNT, C_{78}@SWCNT and Dy@C_{82}@SWCNT FETs show a distinct off state, relating to both hole and electron transport behaviour. The origin of this ambipolar behaviour is related to the presence of an encapsulated fullerene, as the fullerene will perturb the band gap of the SWCNT. Smaller band gaps can lead to significant carrier transport through both the valence and conduction bands, resulting in the observed ambipolar FET behaviour. The overall band gap modulation is dependent upon two factors, the charge transfer between the encapsulated metal atom and the fullerene cage and the diameter of the fullerene cage. Transport measurements have also been performed on spin active Sc@C_{82} metallofullerene peapods [137] again showing band structure modification of the SWCNTs by Sc@C_{82} encapsulation and low temperature measurements providing evidence of that the transport properties of Sc@C_{82}@SWCNTs are quantum coherent.

2.4.3.3 Dynamics of metallofullerenes in peapods

Metallofullerene peapods provide a unique environment to investigate the rotational dynamics of the encapsulated metal atom and understand the dynamics of metallofullerenes ordered in a 1-dimensional array. The motion of La@C_{82}, La_2@C_{82} [138], Ce@C_{82} [139], Gd_2@C_{82} [140] have been observed revealing information of the dynamic behaviour. ^{13}C and ^{139}La nuclear magnetic resonance of La_2@C_{82} determined circular motion of the lanthanum atoms within the fullerene cage even at room temperature, as shown in Figure 2.21A.

HRTEM allows visual investigation of the dynamics of metallofullerene peapods by monitoring the motion of the metal atoms inside the fullerene cage. HRTEM images in Figure 2.21B of Ce@C_{82} peapods taken with a exposure time of 2s with an

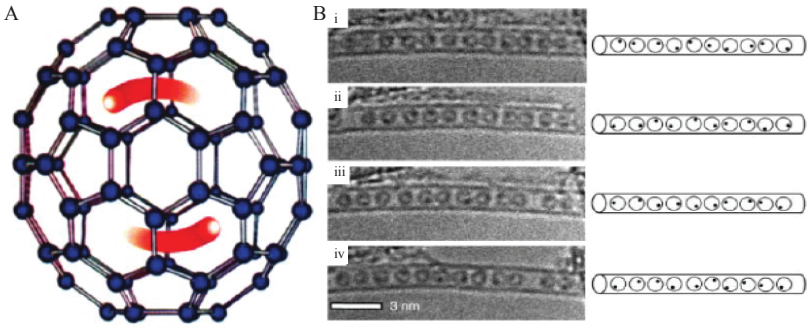


Figure 2.21: (A) Schematic diagram representing the circular motion of two La atoms inside the I_h cage of C_{82} [138]. (B)(i-iv) A time series of successive HRTEM images of Ce@C_{82}@SWCNT, taken with 2s exposure time, and their schematic representation [139]

interval of 10s between each image with a schematic representation in each case [139]. Individual Ce atom are visible in HRTEM, indicated by the spot of higher contrast, inside the fullerene circle. The Ce atoms maximise electrostatic interactions between neighbouring molecules by orientating themselves so that the dipole axis is along the nanotube axis. The time evolution of Ce@C_{82} shows that the atoms remain in a fixed orientation for a period of time before rapidly jumping into another stable orientation, indicating that the observed motion is due to molecular rotation of the metallofullerene cage rather than the individual movement of the encapsulated Ce atom. The rotational dynamics of spin active Sc@C_{82}@SWCNTs have also been observed [141], however, the high contrast spots were not observed in the HRTEM images, indicating that the Sc@C_{82} metallofullerene undergoes continuous rapid rotation which is therefore not detected within the 2s exposure time. Changing the nanotube environment by using MWCNTs changed the rotational dynamics of the Sc@C_{82} as several cages were in fixed orientations with observable high contrast spots for a period of time.

2.5 Summary

Metallofullerenes exhibit novel electronic, optical and magnetic properties, due to charge transfer between the encapsulated metal atoms and the fullerene cage. For metallofullerenes, La@C_{82}, Sc@C_{82} and Y@C_{82} an unpaired electron is delocalized across the cage and interacts with the metal atom. Hyperfine coupling between the electron and nuclear spin of the metal has been detected by EPR for metallofullerene solutions. The goal is to understand the nature of inter-fullerene spin interactions in macroscopic 3D crystals and 1D peapod arrays.

SWCNTs are to be implemented as an architecture material to form 1-D arrays of metallofullerenes. Laser ablation offers a route to produce high quality SWCNTs with a controllable diameter distribution, permitting successful encapsulation of metallofullerene cages. Chemical or physical purification processes of laser ablation SWCNTs should allow high purity samples to be produced. The heterogeneous nature of produced carbon nanotubes results in varying diameter, length and chirality. Centrifugation provides a path towards purifying SWCNTs but can also generating homogeneous SWCNTs samples.

Encapsulation of metallofullerenes inside a carbon nanotube architecture has already demonstrated hybrid properties, largely due to the charge transfer between metallofullerene and the nanotube and the mechanical strain of a forming a 1D array. This thesis aims to understand the metallofullerene spin properties and understand the affect of changing the environment from a 3D crystal to a 1D array.

Chapter 3

Experimental Methods

3.1 Electron Paramagnetic Resonance

Electron paramagnetic resonance (EPR) is a technique to study the spin properties of paramagnetic materials, with applications in the analysis of biological samples, proteins, and chemical samples, radicals and magnetic materials. EPR measures the absorption of microwaves by paramagnetic materials while varying the magnetic field as opposed to radiation frequency. Continuous wave (CW EPR), performed at 9.5 Ghz (X-band), is a fundamental tool to assist the understanding of the spin properties of metallofullerenes and determine the nature of the spin in different carbon environments, 3D crystal (powder) versus 1D array (peapod). CW EPR can also been preformed on SWCNTs to measure the purity level of SWCNTs by tracking EPR signals from magnetic catalyst particles and amorphous carbon impurities.

3.1.1 Principles of CW EPR

In the absence of a magnetic field, an electron spin, S= 1/2, has two degenerate energy levels since the associated magnetic moment is randomly orientated. When an external magnetic field is applied, the electron spin S can only be aligned parallel or anti-parallel to the field which results in the splitting of the spin state into two non-degenerate energy levels, $m_s = \pm 1/2$. The splitting between the two spin states, shown in Figure 3.1, has a energy difference;

$$\Delta E = g.\mu_B.B_o.$$

where g is the g-factor (a proportionality constant), μ_B is the Bohr magneton, and B_o is the static magnetic field. The splitting of the electron spin states in the presence of a magnetic field is due to the *Zeeman Effect* and is fundamental to EPR. If the system is exposed to electromagnetic radiation equal to the energy difference between the energy levels then the photon energy, $h\nu$, will be absorbed by the spin, as demonstrated in Figure 3.1;

$$\Delta E = h\nu = g.\mu_B.B_o.$$

To measure this absorption the electron spins are irradiated with a fixed frequency microwave radiation and the magnetic field is swept. When the field reaches resonance conditions, microwaves are absorbed by the electron spins and this absorption is observed experimentally.

Typical EPR samples contain many electron spins in the system, which can interact with each other and with the lattice environment. If there was no lattice interaction, then the applied microwave field would eventually equilibrate the two population levels causing a loss of the EPR signal. With electron spin lattice interactions, there are competing processes between microwave field equilibration and

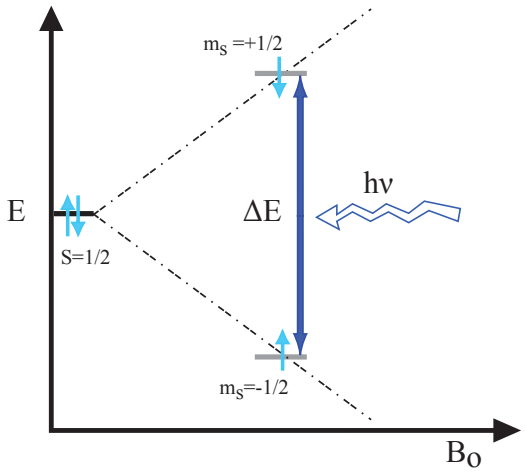


Figure 3.1: Diagram representing the Zeeman splitting of the electron spin, S =1/2, with an applied magnetic field.

the spin lattice interaction, allowing the continued observation of the EPR absorbed signal. If the strength of the microwave field increases with respect to the spin lattice interaction, then the EPR signal *saturates*, and no net energy is transferred between the field and the spin system [142]. The coupling between the electron spin and the lattice environment is measured by T_1, the spin relaxation time. The effects of saturation and spin lattice interactions are shown in Figure 3.2. Experimentally if the spin system is not saturated the spin susceptibility, integrated area of the EPR absorption spectra, should increase proportionally with the square root of the microwave power.

Electron spins are sensitive to the environment and can interact with nuclear spins of the systems. The nuclear spin has magnetic moments which is influenced by the presence of the magnetic field. The energy of nuclear spin, I, is influenced by magnetic field, leading to the nuclear Zeeman effect. The electron spin and nuclear spin can interact, resulting in *hyperfine interaction*, which splits the EPR lines

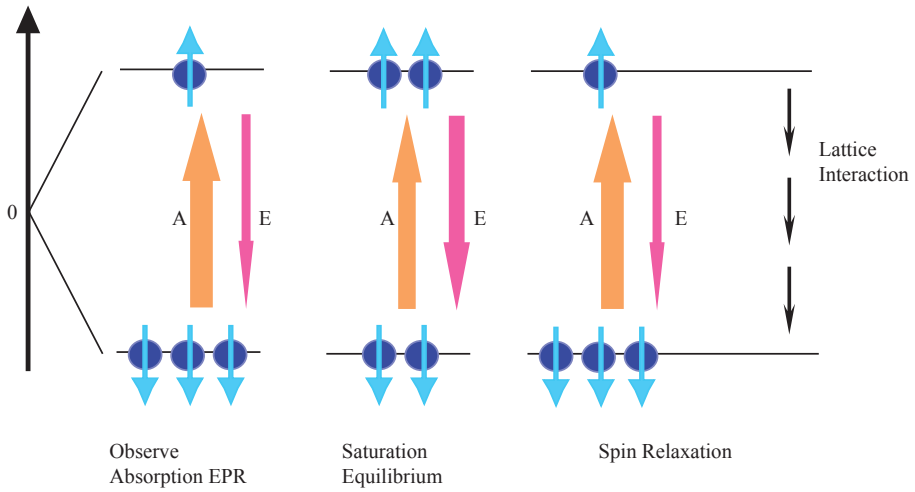


Figure 3.2: Schematic diagram of effect of saturation and lattice interactions, where A is absorption and E is emission. [142]

into several components. Each electron spin Zeeman level is split by the hyperfine interaction into $2I + 1$ levels, giving a total of $2I + 1$ allowed transitions, which are detected in the EPR signal. Species such as Sc and La, with $I = 7/2$ have 8 EPR lines, as shown in Figure 3.3, where the EPR lines are separated by hyperfine splitting constant a. Y with $I = 1/2$ would show 2 lines in the EPR signal.

In systems where there are many electron spins the electronic magnetic moments of the respective electron spins can interact with each other. The interaction between the magnetic moments is referred to as dipole-dipole interaction and is proportional to $(1/r^3)$, where r is the distance between the magnetic moments. Strong dipole-dipole interactions will result in the broadening of the overall EPR signal.

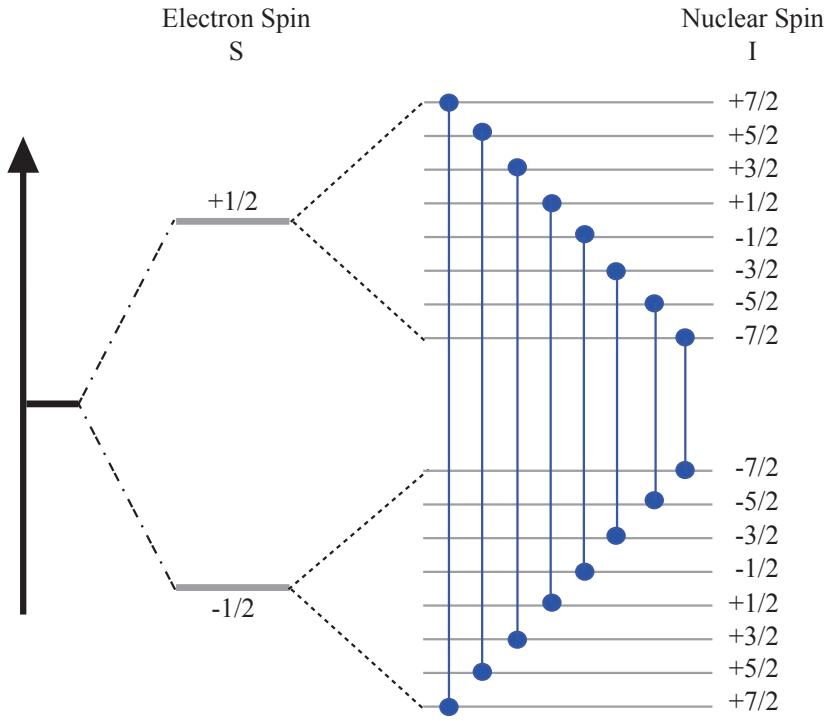


Figure 3.3: Schematic diagram of origin of the hyperfine interaction between the electron spin and nuclear spin of La or Sc atoms

3.1.2 Practical Methodology

Sample preparation of metallofullerene and nanotube samples is important as it can affect the observed EPR signal. When EPR samples are prepared it is important that the samples are degassed to remove any oxygen from the system. Oxygen could interact with the metallofullerene spin system via Heisenberg exchange and/or electron-electron dipolar interactions [143], which may result in changes in the observed lineshape and spin-lattice relaxation measurements. Samples prepared in solution or powder phase will exhibit different EPR signals due the nature of the spin system. Solution phase samples will exhibit an isotropic hyperfine constant and due to the rotational and translational motion of molecules will give an average

g-value. Powder or polycrystalline samples contain multiple paramagnetic centres which are rigidly held leading to anisotropic hyperfine constants and g values. The anisotropy can give more complex EPR spectra, since all orientations of the paramagnetic centres are observed resulting in broadening of the EPR signal. Powder EPR can reveal how the spin interacts with the neighbouring system, for metallofullerenes this relates to how the spin interacts with other fullerenes and with the carbon nanotube. The g-factor for a completely free electron is, g=2.0023, however this can be expected to shift due to the nature of the environment surrounding the spin. Spin orbit coupling and interactions between the electron spins and environmental sources such as hyperfine interaction with nuclei spins, dipole interaction with other electron spins and interactions with defects and other chemical species can cause shifts in the observed g-factor.

3.2 Transmission Electron Microscopy

Transmission electron microscopy (TEM) is a technique where a beam of electrons is transmitted through an ultra thin specimen, interacting with the specimen as it passes through. TEM can be used to visualize and understand the structural properties of carbon nanotubes and peapods. Any study of peapod systems should include a TEM study as it provides high resolution visual evidence of fullerenes filled inside nanotubes. TEM can also be used to determine the structural properties of nanotubes and also analyse nanotube purity, by measuring the levels of impurities such as amorphous carbon and catalyst particles.

Ernst Abbe demonstrated that the resolution of optical microscopes are dependent upon the wavelength of the illumination source and calculated the maximum

resolution that could be obtained using optical microscope. The resolution limit of optical microscopes, typically 300nm, restricts any use of visible light microscopy to investigate nanoscale materials. Given Louis de Broglie's (1925) theory that the electron has wave-like characteristics, with a wavelength substantially less than visible light, electrons should provide resolutions suitable to investigate nanometer samples. The use of an electron beam source, as opposed to optical light, was first developed in a working microscope by Ruska in 1932 [144], later awarded the Nobel prize in 1986. Accelerated electrons, in vacuum, behave like light but have a much smaller wavelength, potentially offering sub-angstrom resolution [145]. The higher resolution power has made electron microscopy a powerful tool to study the lattice structure, defects and dynamics of nanomaterials.

TEM operates by focusing the electron beam, typically generated from a tungsten or LaB_6 source, onto a single pinpoint spot on the sample specimen. The electron beam passes through electromagnetic lenses to focus the beam. The first lens, shown in Figure 3.4, is the condenser lens, which makes the electron beam into a parallel beam and illuminates it onto the specimen. The electrons interact with the sample, and are either diffracted, scattered or pass through unobstructed. The electrons which have passed through the specimen are brought in focus through the objective lens. As this point in the TEM different apertures can be used to diverge or converge the electron path through the lens. The objective aperture can enhance contrast by blocking high-diffracted electrons, while the selected area aperture enables the investigation of the periodic diffraction of electrons by ordered arrangements of atoms in the sample. The electron beam is magnified and focused and then detected by a phosphorescent or fluorescent screen on the other side forming an image, which can be connected to a CCD camera.

In High Resolution TEM (HRTEM) contrast in the image is produced by phase contrast. When the electron beam penetrates the sample, electrons will either pass through the samples or interact with the sample and scatter. Considering electrons as waves, the interaction between the sample and the electron beam will cause the wave to shift in phase. Phase contrast is generated by the recombination of the scattered and primary un-scattered waves. With additional phase shift it is possible to ensure the scattered wave and primary wave are either in or out of phase with each other, creating amplitude contrast. The phase shift is affected by the spherical aberration of the objective lens or by controlling the defocus of the objective lens.

Performing HRTEM exposes carbon nanomaterials to a high energy electron beam source which can cause damage to the carbon material structure, due to carbon's low knock-on threshold [146]. Even a low accelerating voltage of 80 kV prolonged exposure to accelerating electrons can damage SWCNTs. Dirty, defective and narrow diameter, less than 1nm, are unstable, while clean large diameter SWCNTs are stable against exposure to accelerated electrons [125]. Performing HRTEM at 80 kV limits the resolution which can be obtained in non-aberattion corrected microscopes, but the samples will be more stable when exposed to the electron beam. The high energy electron beam can be employed to cause modification of carbon nanomaterial structures to form hybrid structures, C_{60}@SWCNT peapods upon exposure to high energy electrons formed novel C_{300} structure.

Image resolution is limited by optical aberrations, in particular spherical and chromatic aberration, which arise due to increased scattering of electrons at the edge of the intrinsically imperfect electron lenses. Equipped with a new generation of aberration correctors it has been demonstrated that spherical aberration can be overcome and atomic resolution can be achieved [147, 148]. This opens a new path

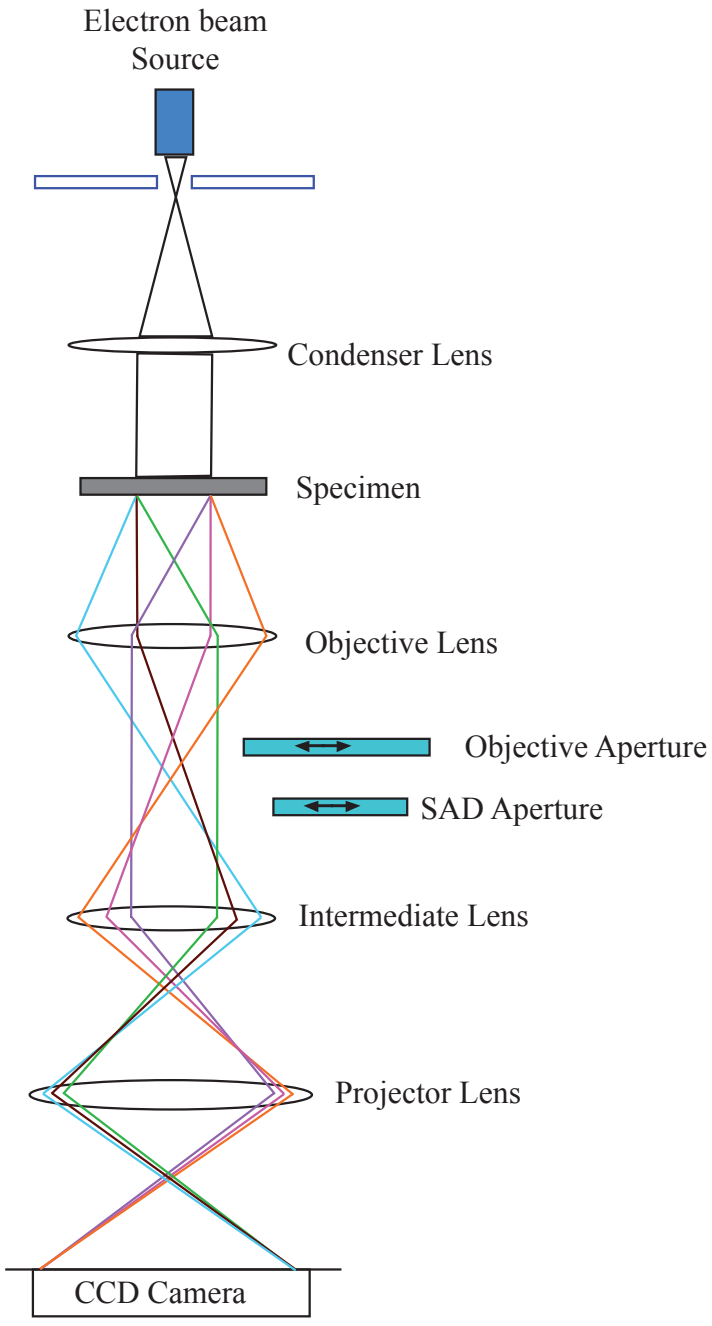


Figure 3.4: Schematic diagram of transmission electron microscope

to investigate carbon nanomaterials as observation of hexagonal lattice structures and individual carbon atoms can allow for greater study of carbon nanotubes and graphene [149, 145].

HRTEM was employed to understand the structure and behaviour of carbon nanomaterials. SWCNTs samples can be studied to comprehend the composition of the samples in terms of defects, impurities, catalyst particles and nanotube diameter. HRTEM can directly provide visual evidence of successful filling of endohedral metallofullerenes inside the hollow interior of SWCNTs, and provide an idea of the degree of filling. HRTEM will only image a certain area of the nanotube or peapod samples, therefore it can provide a good estimate regarding factors such as filling ratio, nanotube diameter and nanotube defects, and should be used in conjunction with other analytical techniques.

3.3 Optical Absorption

Optical properties of carbon nanotubes are unique due to the optical transitions within the one-dimensional density of states (DOS), leading to sharp van Hove singularities, as depicted in Figure 3.5A. The van Hove singularities allow certain transitions for semiconducting and metallic nanotubes, where the transitions between the valence band and the conduction band occur in the UV-Vis region [150].

Figure 3.5A shows the transitions from the valence band to the conduction band for metallic and semiconducting SWCNTs. These transitions can be detected by optical absorption spectroscopy. Optical absorption of heterogeneous SWCNTs will detect the first and second semiconducting absorption peaks referred as S_{11} and S_{22} respectively and the first metallic absorption peak refereed to as M_{11}. The

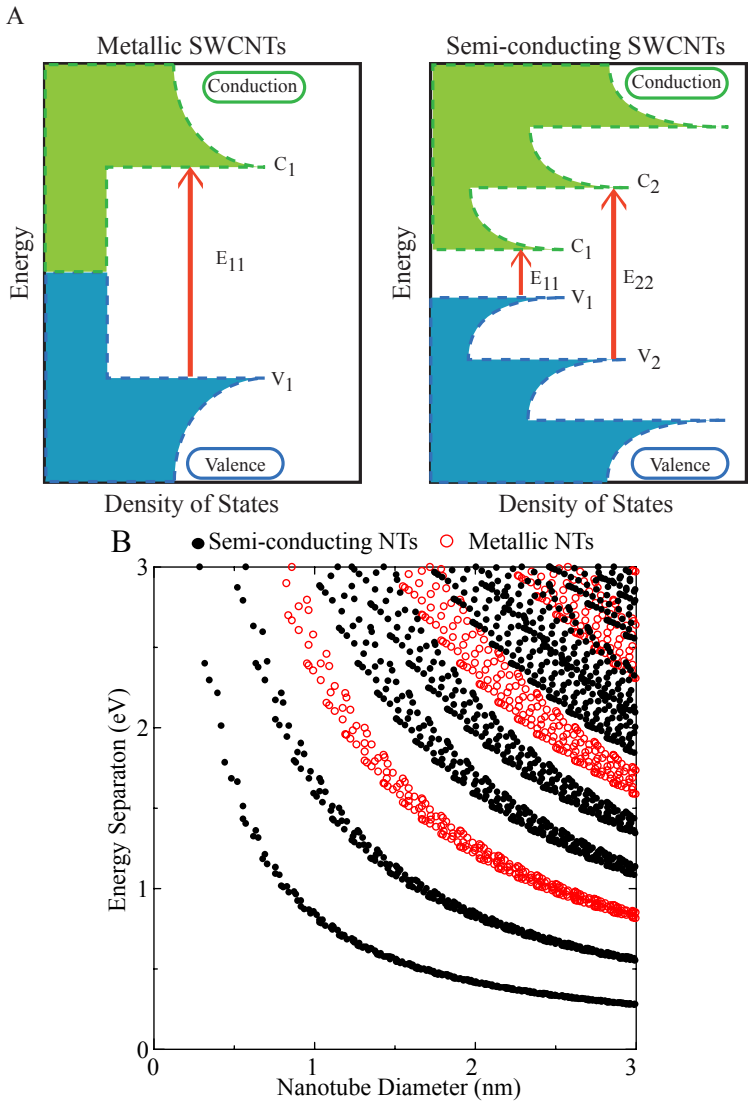


Figure 3.5: (A) Diagram representing the DOS for SWCNTs (*left*) DOS for metallic nanotubes, with the first transition E_{11} occurring at high energy. (*right*) DOS for semiconducting SWCNTs show a small band gap and a number of transitions, with the E_{11} and E_{22} occurring at lower energy than the metallic transition (B) Kataura plot [151] showing the correlation between the diameter of semiconducting and metallic nanotubes and their respective calculated energy

semiconducting and metallic transitions occur in the near infra-red visible region between 2200 nm and 400 nm. The optical properties of nanotube vary depending upon their structure, in terms of electronic type and diameter. As the diameter of the SWCNTs decreases the optical transitions shift to a higher energy. Since most SWCNTs contain a distribution of nanotube diameters the optical transition will become broadened. Kataura *et al.* [151] calculated the energy of the semiconducting and metallic nanotube transitions, for all (n,m) chiral values, referred to as the Kataura plot. The Kataura plot, shown in Figure 3.5B can be used to relate the optical absorption spectra with the SWCNT chiral indices.

Optical absorption spectroscopy can be employed to analyse the fundamental structural and electronic properties of SWCNTs. Analysis of the observed semiconducting S_{11} and S_{22} and metallic M_{11} peaks can provide information regarding the mean diameter and the diameter distribution for different SWCNT samples. Amorphous carbon impurities contribute to the overall π-plasmon background detected for SWCNT samples, therefore comparing the ratio of the individual semiconducting and metallic peak to the overall spectra should provide a relative guide to purity of the SWCNTs [152]. Optical absorption is critical for any investigation regarding separation of semiconducting and metallic SWCNTs as comparisons of the ratio of metallic and semiconducting peaks provides a guideline for the level of separation.

3.4 Raman Spectroscopy

Raman spectroscopy can be employed to measure the vibrational properties and electronic structure of carbon nanotubes and can yield information regarding the diameter of the carbon nanotubes and the quality of the nanotube sample [153].

Raman spectroscopy measures the inelastic scattering of a material when radiated by a monochromatic light source, such as a laser [154]. The scattered photon can either be of similar energy to incident photon, Rayleigh Scattering, or can differ in energy, Raman scattering. Raman scattering involves the energy exchange between the photon and the molecule, with the affect that the scattered photon differs higher or lower in energy to the incident photon. This change in energy, Raman shift, can be attributed to the change in the rotational and vibrational energy of the material and can provide information regarding energy levels [153]. Raman spectroscopy plots the intensity of the Raman shift against frequency.

Carbon nanotubes with different (n,m) values will scatter light differently, as such, it is possible to observe these difference in the Raman spectra, with Figure 3.6 showing the Raman spectroscopy of PtRhRe SWCNTs.

At low frequencies, between 75 and 300 cm^{-1} carbon nanotubes exhibit Radial Breathing Modes (RBM) corresponding to the radial contraction and expansion of the nanotube. The frequency of the RBM (V_{RBM}) is directly linked to the reciprocal nanotube diameter (d_t),

$$V_{RBM} = 224/d_t$$

allowing the nanotube diameter to be calculated for SWCNTs from the Raman spectra. Other important features detected through Raman spectroscopy are the D and G peaks. The D peak ($\sim$1330 cm^{-1}) corresponds to defects in sp^2 carbon network and the G peak ($\sim$1590 cm^{-1}) corresponds to the planer vibrations of carbon atoms i semiconducting and metallic carbon nanotubes. The ratio of the D peak ($\sim$1330 cm^{-1}) and the G peak ($\sim$1590 cm^{-1}) is used to measure the degree of disorder in the SWCNTs [155]

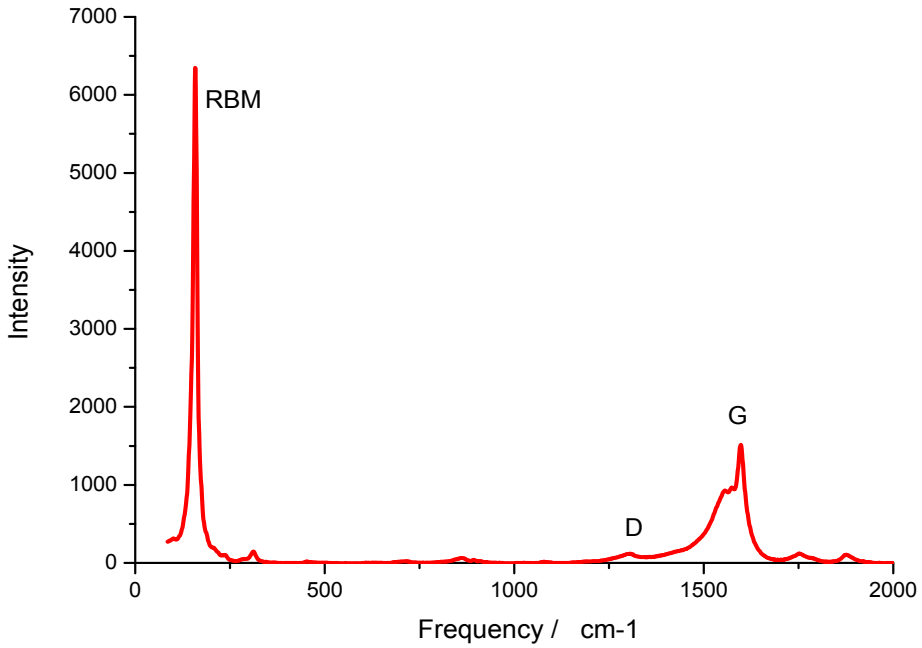


Figure 3.6: Raman spectra of PtRhRe SWCNTs showing the RBM, the G and D peaks.

Chapter 4

Purified Carbon Nanotubes Spin Properties

4.1 Introduction

Carbon nanotubes are ideal for the production of spintronic [5] devices owing to the long electron spin lifetimes [156] and high Fermi velocity [156] and their ability to be filled with metallofullerenes to produce 1D ordered arrays of spins. It is vital to understand the magnetic properties of electrons in single walled carbon nanotubes (SWCNTs) in order to effectively utilize them in spintronics devices. Electron paramagnetic resonance (EPR) can provide an insight into the spin properties of SWCNTs as it can probe conduction electrons and unpaired spins.

EPR of SWCNTs was reported by Petit *et al.* [157] and a strong signal attributed to conduction electrons was observed. Bandow *et al.* [158] reported experiments on multi-walled nanotubes and SWCNTs that indicated a relationship between contacting nanotube bundles and the EPR lineshape. Contrary to the experiment by

Petit, no signal associated with the presence of conduction electrons was detected. Salvetat *et al.* [159] irradiated SWCNTs with 2.5 MeV electrons, inducing defects, in order to detect conduction electron spin resonance. However, the EPR spectrum was dominated by magnetic catalyst impurities. In an attempt to solve this problem of magnetic catalyst particle impurities Corzilius *et al.* [160] used carbon nanotubes grown using chemical vapour deposition (CVD). These vertically aligned forests of nanotubes can be removed from the substrate, leaving behind the residual catalyst. Low temperature measurements found sharp EPR lines that were attributed to conduction electrons trapped inside nanotube defects. However, the lack of in-depth structural characterization by high resolution transmission electron microscopy (HRTEM) makes it difficult to link EPR properties with specific structural features of the SWCNTs. EPR has also been employed to study SWCNT peapod structures [161, 162] elucidating charge transfer between metallofullerenes and SWCNTs, and hydrogen absorption [163] of nanotubes preferentially at defect sites, causing the EPR signal to diminish.

These often discordant results of SWCNT EPR highlight the need for ultra-pure samples free from metal impurities and the application of multiple characterization techniques in order to build a balanced and deep picture of the structure-EPR relationship. SWCNTs have generally been grown using magnetic transition metal catalyst particles,[157, 158, 159] which contribute strong EPR signals and efforts to remove magnetic particles often leave the SWCNTs highly defective [160]. Preparation of high quality pristine SWCNTs is essential for the investigation of the origin of SWCNT EPR. Processing of SWCNTs requires the removal of amorphous carbon and catalyst particles with minimal damage to the nanotube structure.

4.2 Purification of Carbon Nanotubes

Different purification methods were utilized to remove amorphous and graphitic carbon, and catalyst particle impurities, based upon high vacuum high thermal annealing and ultracentrifugation [164, 165]. Kitaura *et al.* [164] annealed raw SWCNTs at 1200 °C for 24 hours under high vacuum to remove amorphous carbon and vaporise Fe catalyst particles. Superconducting quantum interference device (SQUID) magnetometry of the thermally annealed SWCNT sample showed minimal magnetic susceptibility over the temperature range, demonstrating the removal of Fe catalyst particles while retaining nanotube structure. Ultracentrifugation allows for facile separation of nanotubes and catalyst particles without damaging the carbon nanotube structure. The traditional approach to purify laser ablation PtRhRe catalyst SWCNTs was to use microwave digestion followed by aqua regia treatment, [77]. This purification process is relatively harsh and some of the catalyst particles remain resistant to the treatment process. Centrifugation was explored to purify carbon nanotubes by removing heavy catalyst particles without damaging the intrinsic nanotube structure. Density gradient ultracentrifugation (DGU) has been developed as a large scale method for the separation of SWCNTs into semiconducting and metallic chiralities and has primarily focused on smaller diameter nanotubes [107, 166]. Larger diameter SWCNTs are more challenging to separate into different chiral forms due to the broad overlap of diameters for semiconducting and metallic species. Larger diameter SWCNTs have been used because they can be filled with spin-active metallofullerenes to form 1D peapod systems [161].

4.2.1 Principles of centrifugation

Particles of different densities can be separated by applying a force, such as the earth's gravity, however, particles of similar density may take a long time to achieve separation. To encourage separation, particles can be rotated at a certain speed or revolutions per minute (RPM), which applies a centrifugal g-force, causing the particles to move rapidly away from the axis of rotation. Particles with larger mass will experience a greater centrifugal force and thus move more quickly to the bottom of the container. For SWCNTs centrifugation could potentially force heavy catalyst particles to sediment, while isolated nanotubes would be located in the supernatant. An advanced centrifugation technique is density gradient ultracentifugation (DGU). A media, such as sucrose [167] or iodixanol, is used to build a gradient with the heaviest density at the base and incrementally decreasing the density as increasing vertically. The sample to be separated will be placed in the gradient media and undergoes centrifugation over a long period. Particles will sink during centrifugation until they reach a position where their buoyancy matches the buoyancy of the surrounding density gradient. DGU can be employed to separate out semiconducting and metallic nanotubes and has been shown to be able to isolate individual chiralities of nanotubes. Competing surfactants, sodium cholate and sodium dodecyl sulphate, have different binding affinities for semiconducting and metallic nanotubes and thus these nanotubes will have different buoyant densities, allowing them to be separated in DGU.

4.2.2 Experimental Methods

SWCNTs were grown using laser ablation with non-magnetic catalyst particles (PtRhRe), using a ratio of the catalyst as previously reported in reference [77]. Laser ablation production of SWCNTs was performed at the IFW Dresden in collaboration with Dr. M. Rümmeli. For optimal production of SWCNTs the laser ablation setup, schematic shown in Figure 4.1, an oven temperature of 1430 °C and a nitrogen gas flow was used. The setup produced high quality carbon nanotubes with mean diameter 1.4 - 1.6 nm, which are ideal for filling of endohedral metallofullerenes.

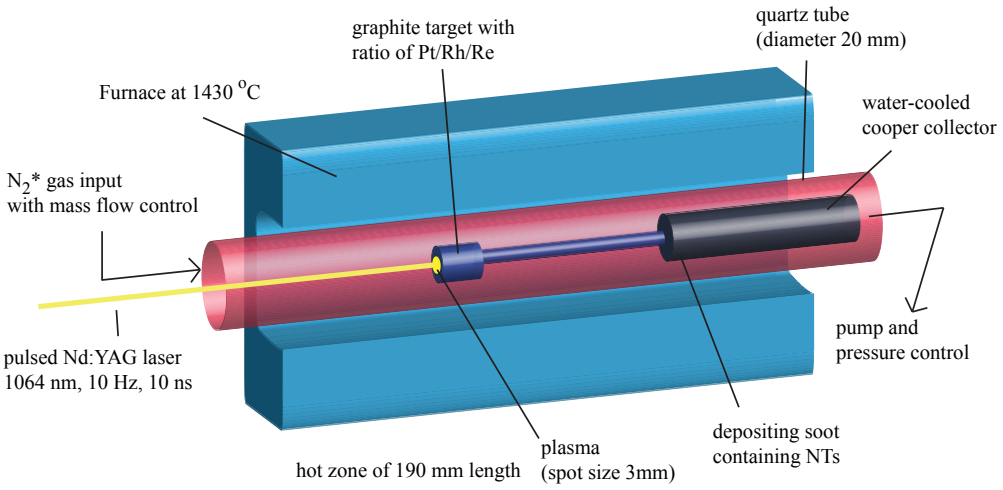


Figure 4.1: Schematic diagram of the laser ablation setup used to produce PtRhRe catalyst SWCNTs at the IFW Dresden

Raw laser ablation PtRhRe catalyst SWCNTs were purified by aqua-regia microwave digestion [92] or ultracentrifugation. Ultracentrifugation was performed using a swing bucket SW41Ti rotor and Beckman Coulter ultracentrifuge model L100-XP at 41krpm (g-force 288,000). For centrifuge samples which required slower

revolutions a Labofuge 200 Heraues was used at 5 krpm. SWCNTs aqueous solutions were produced using surfactants, sodium cholate (SC), sodium dodecyl sulphate (SDS) and deoxy cholate (DOC) and sonicated using a horn tip sonicator (Cole Parmer ultrasonic processor). While sonicating the SWCNT, between 1-4 hours, samples were placed in an ice bath to prevent thermal damage to the SWCNT. Density gradient centrifugation layers were produced using an iodixanol (60% density) gradient media and Beckman Coulter 14 x 89 mm Ultra clear tubes.

The ultracentrifugation purification process involved multiple steps to purify the raw PtRhRe SWCNTs, as shown in the schematic diagram in Figure 4.2. The initial step was to anneal the raw SWCNTs in air at 300 °C for 2 hours in order to remove amorphous carbon. Annealed SWCNT were dispersed in an aqueous solution of 2% sodium cholate (SC) / deoxy cholate (DOC) [ratio 4:1] (or 2% SC/SDS ratio 3:2) to a concentration of 0.5 mg ml^{-1}. To improve the solubility of the SWCNTs in water the SWCNT 2% SC/DOC solution was sonicated for 4 hours using a horn-tip sonicator, shortening the nanotubes and resulting in a disperse nanotube solution. The sonicated SWCNT solution was centrifuged for 1 hour at 41 krpm to separate nanotubes from the catalyst particles. The upper 85% of the solution was collected and was termed 'SWCNT supernatant'. The material at the bottom of the centrifuge tube was also collected and was termed 'SWCNT sediment'. The obtained supernatant was very dilute and at its current concentration would be ineffective for DGU. The SWCNT supernatant was concentrated using centrifugal filters (Amicon 30 kDa, Millipore), for 7 minutes at 5 krpm, filtering out part of the 2% SC/DOC aqueous solution, repeating the process till a dark black SWCNT solution was visible, as shown in Figure 4.3. The concentrated SWCNT supernatant sample was further centrifuged for 17 hours at 41 krpm using an iodixanol density

gradient (20-40% linear gradient with 2% SC/SDS [ratio 2:3]). A step gradient was prepared by layering different iodixanol density layers, the base contained 40% iodixanol 2ml, a SWCNT layer 35% iodixanol 3ml was added on top, then subsequent layers of 1.5 ml of 27.5%, 25%, 22.5% and 20% iodixanol were placed on top. For 20%-60% gradients, the base contained 60% iodixanol 2ml and subsequent layers of 1.5ml of 50%, 40%, 30%, 20% and 0% with a 2ml SWCNT layer 35% iodixanol layered in between. The gradient was left about 4-6 hours to allow the layers to form a linear gradient. The process of using density gradient ultracentrifugation (DGU) was employed with the primary function of isolating catalyst free SWCNTs. The separated fractions from the DGU were isolated, and the bulk black nanotube suspension was collected and termed 'DGU SWCNT'.

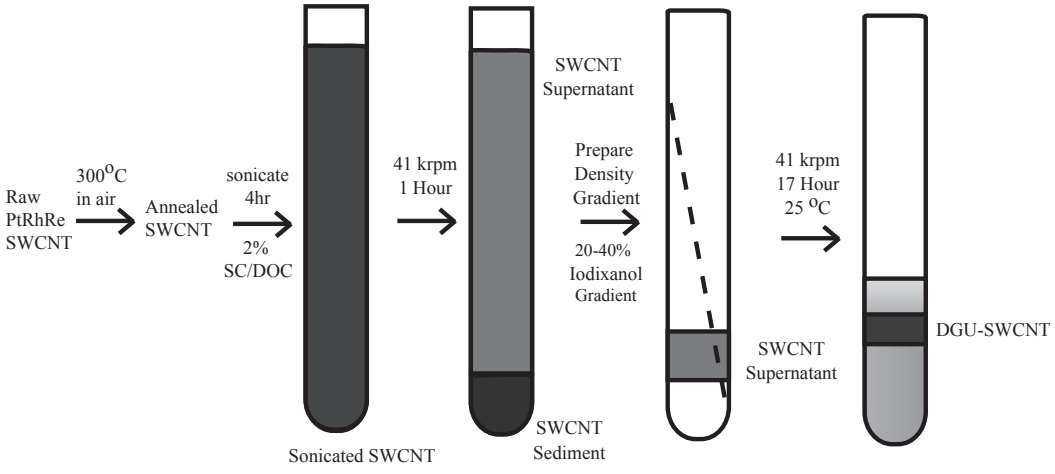


Figure 4.2: Schematic diagram indicating the multiple steps involved in the purification process of the SWCNTs

Meijo FHP and SO SWCNTs were produced by Meijo Nano Carbon inc, via arc-discharge using magnetic catalyst particles Fe and Ni/Y respectively [168]. As grown arc-discharge SWCNTs were air oxidized at 400 °C and further purified in

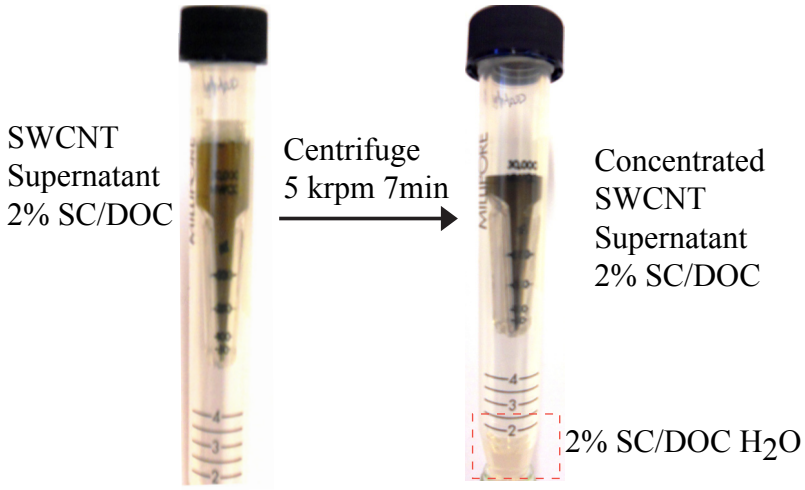


Figure 4.3: Photos illustrating the concentration of SWCNT solutions using microfilters. After centrifugation aqueous surfactant solutions pass through the microfilter to the base of the tube, leaving a concentrated SWCNT solution.

hydrochloric acid. High temperature annealing [164] was performed between 1100-1400 °C at a vacuum pressure of 10^{-3}-10^{-4} Pa for 6-24 hours. To understand the affect of nanotube defects on the EPR signal Meijo FHP SWCNTs were refluxed in nitric acid HNO_3 for 2.5 hrs at 130 °C in order to induce defects.

Ultrapure (95%) semiconducting (IsoNanotube-S) and metallic (IsoNanotube-M) SWCNTs (in buckypaper form), separated by commercial DGU, were purchased from Nanointegris. These nanotubes were produced by arc-discharge and have gone through a repeated centrifugation process, giving high purity and have a diameter distribution of 1.2 - 1.7 nm, suitable for filling of metallofullerene species to form peapods.

A Vibrating sample magnetometer (VSM) (Lakeshore 7400 VSM and EM4-HVA electromagnet) was used for magnetization measurements. Atomic force microscopy

(AFM) was performed, by Evan Wang, using a Park Scientific instrument CP-II AFM. AFM samples were prepared by spin coating SWCNTs solutions on functionalized Si/SiO substrates [169]. All samples for EPR were pumped to remove oxygen and sealed in a quartz tube under vacuum. EPR measurements were performed using a Bruker EMX spectrometer at 9.4 GHz at 5 K in an Oxford ESR900 cryostat. Raman spectroscopy was measured, by Alex Robertson, using a JY Horiba Labram Aramis Raman microscope using a frequency doubled Nd:YAG laser at 532 nm.

High resolution transmission electron microscopy (HRTEM) was performed, with the assistance of Jamie Warner and Franziska Schäffel, on a JEOL 4000EX operating at 80 kV. I prepared all the HRTEM samples and processed and analysed all of the HRTEM images. SWCNT powders or buckypaper samples were sonicated in dichloroethane to form a dispersion and then drop coated onto a lacey carbon grid. SWCNT solutions coated by surfactants required washing with methanol to remove the surfactants. A preparation process, shown in Figure 4.4, was developed where methanol was added to the SWCNT surfactant solution and sonicated to destabilize the bonds between surfactants and nanotubes, and therefore cause the hydrophobic nanotubes to aggregate. The aggregated SWCNTs were collected and washed again till a clear solution containing the aggregated nanotubes was obtained, as shown in Figure 4.4. Ensuring that all the surfactants were removed was important for HRTEM analysis of SWCNTs, as the HRTEM image in Figure 4.4A shows heavy coating of surfactants, making it difficult to visually analyse the SWCNTs and would be detrimental to the identification of any peapods in any filling experiments. Figure 4.4B shows a HRTEM image of the SWCNTs having be processed through several methanol washes showing clean SWCNTs.

UV-Vis absorption spectroscopy was measured for SWCNT films between 400

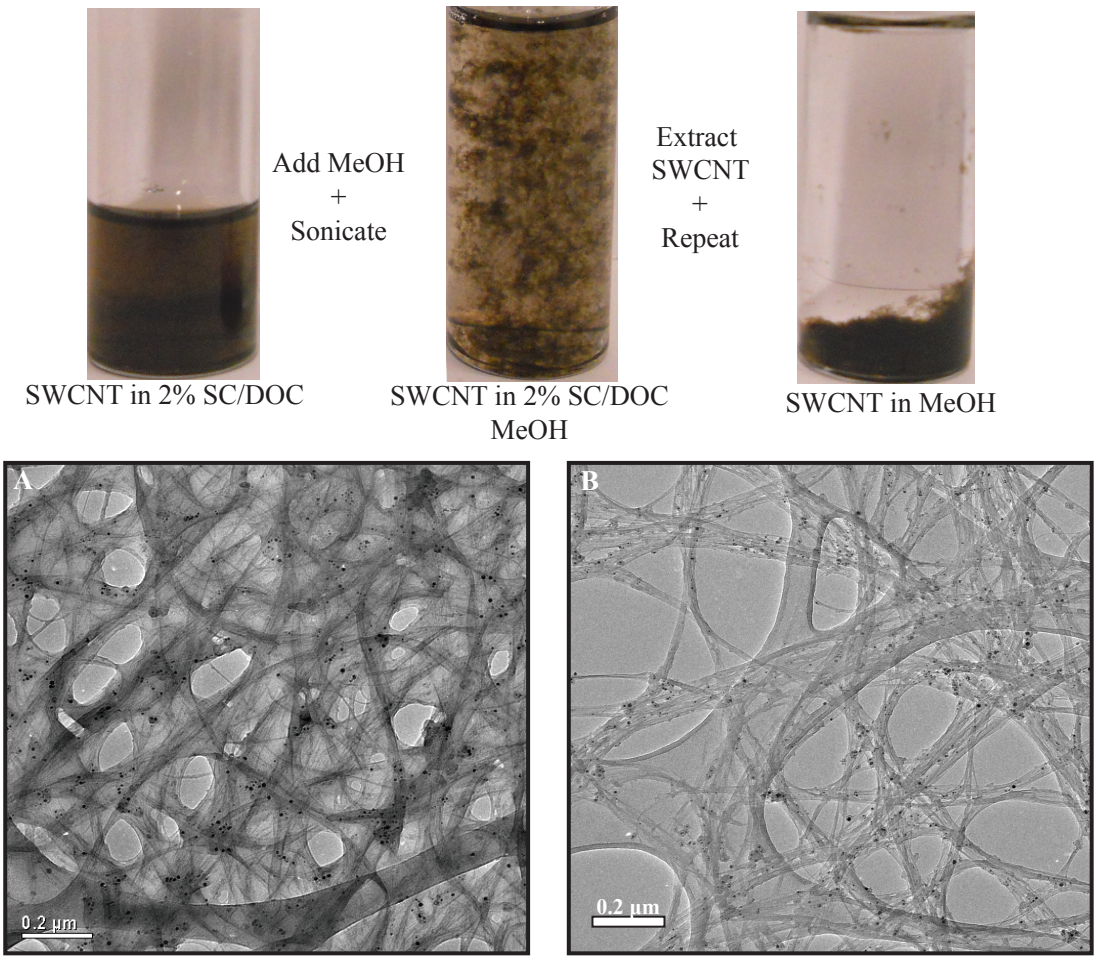


Figure 4.4: (*top*) Images of the SWCNT in 2% surfactant solution, sonicated in MeOH and final MeOH wash (*bottom*) (A) HRTEM image of SWCNT in 2% surfactant solution (SC/DOC) showing SWCNT heavily coated with surfactants (B) HRTEM image of SWCNTs washed in MeOH, showing clean nanotubes

nm and 2200 nm using a Jasco V-570 UV/Vis/NIR spectrometer. SWCNT aqueous solutions would often yield poor optical spectra as the strong absorption of water, between 970-1070 nm and 1130-1290 nm, overlapped with the S_{22} peak for the large diameter of the laser ablation SWCNTs. This limited the purity and separation analysis that could be conducted on the semiconducting peaks after ultracentrifugation. To counter this problem the S_{33} peak could be used as a comparison, but this is often weakly observed, or D_2O, which absorbs in different regions, could be used. Instead a process was developed to produce homogeneous thin films of SWCNTs which could be analysed over a wider wavelength range and provide data which could be easily analysed. SWCNT films were prepared through vacuum filtration using a nitrocellulose microfilter. SWCNT solution was deposited on the 0.025 μm nitrocellulose microfilter (Millipore), a narrow pore size was essential since nanotubes may have been sonicated shortening their length, rendering 0.22 μm microfilters ineffective. The SWCNTs microfilter was placed in an acetone bath, dissolving the nitrocellulose filter, leaving a nanotube thin film. The thin film would be transferred to another acetone bath to ensure the complete removal of the microfilter, before being transferred on to a quartz substrate (15mm diameter, 2mm thickness, Edmund optics). The sample was be left to dry to remove excess acetone and then were ready for use in the UV-Vis spectrometer. The complete protocol for the formation of SWCNT thin films is illustrated in Figure 4.5 which shows the optical absorption of the SWCNT thin film, with the semiconducting and metallic peaks clearly observed.

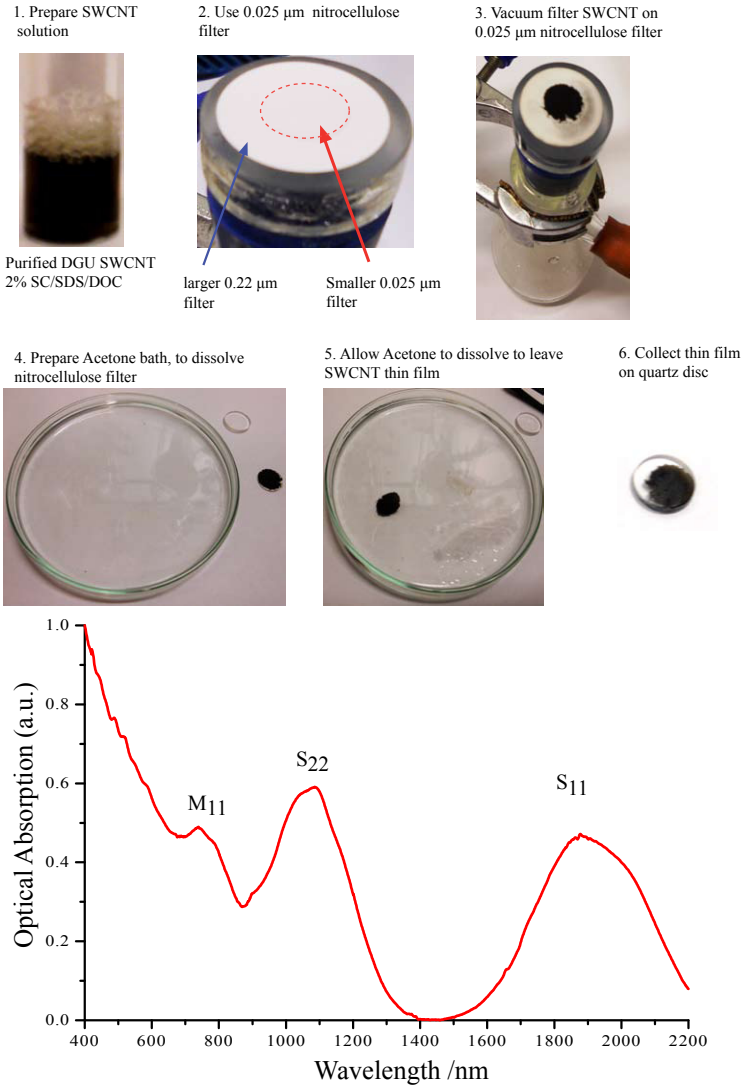


Figure 4.5: Procedure for producing SWCNT thin films for UV-Vis spectroscopic detection (1) Prepare SWCNTs H_2O surfactant solution (2) 0.025 μm nitrocellulose microfilter (indicated in red) was used on top of the larger 0.22 μm microfilter (3) SWCNTs were vacuum filtered through the 0.025 μm nitrocellulose microfilter for about 1 hour (4) The obtained SWCNT nitrocellulose filtered sample was placed into a acetone bath (5) The nitrocellulose membrane dissolved in acetone, leaving a thin SWCNT film (6) Ensuring all the nitrocellulose membrane was removed the SWCNT film was captured onto a quartz disc and was ready for optical detection. UV-Vis absorption spectra, performed between 2200 nm and 400 nm, of a laser ablation PtRhRe catalyst SWCNT thin film shows the semiconducting (S_{11}) and (S_{22}) and metallic (M_{11}) peaks.

4.2.3 SWCNT Ultracentrifugation

The primary aim for using centrifugation was to purify carbon nanotubes from residual catalyst particles and a secondary aim was to obtain separated semiconducting and metallic carbon nanotubes. DGU has been successfully employed as a separation method in biological samples, such as separating proteins. Arnold *et al.* [107] first employed the method to sort out heterogeneous carbon nanotubes, separating nanotubes by diameter and by metallic or semiconducting electronic nature. Other separation techniques have been explored, but DGU has received much attention due to its scalable approach and potential to extract individual chiral (n,m) nanotubes. Nanotubes are separated in DGU due to variation in buoyancy and difference in surface functionalization. Arnold *et al.* determined that nanotube buoyancy increased with diameter and that different surfactants would preferentially bind to nanotubes of specific electronic type.

The original separation procedure and methods since developed [166] have proved effective at separating narrow diameter nanotubes by chirality. Narrow diameter SWCNTs appear to be easier to separate as they can be detected by individual coloured bands and show isolated narrow peaks in optical absorption spectroscopy, allowing individual chiral SWCNTs to be identified. Laser ablation PtRhRe catalyst SWCNTs are larger in mean diameter than the HiPCO nanotubes, used in the described experiments [107, 166], and show considerable overlap of nanotube diameters in the optical absorption, with broad semiconducting and metallic peaks observed.

The first attempt at separating the laser ablation PtRhRe SWCNTs, following the method described in Arnold *et al.* [107] using 2% SC/SDS [3:2 ratio], failed to

show any separation between semiconducting and metallic nanotubes. Figure 4.6A shows the ultracentrifuged laser ablation SWCNTs, with 2% SC/SDS [3:2 ratio], separated into two distinct dense black bands with no visible coloured layers and UV-Vis spectra further confirming no apparent differences in semiconducting metallic nanotube ratios. Attempting the same process on HiPCO nanotube, separation between the bands was visually observed in Figure 4.6B with a narrow blue band observed above the dense black nanotube layer [1], indicating that a small amount of the HiPCO SWCNTs had been separated. However, the narrow blue band limited the volume of separated HiPCO SWCNTs which could be extracted, making it difficult to perform UV-Vis spectra to identify the ratio of semiconducting and metallic SWCNTs. Since HiPCO SWCNTs have a diameter unsuitable for filling, no further investigations were performed using these nanotubes.

Although the initial ultracentrifugation process failed to separate laser ablation nanotubes by electronic type the process could still be optimized for nanotubes to undergo purification. In order to produce high quality purified nanotubes, isolated from catalyst particles and amorphous carbon impurities, a multi-step purification process was developed, as described in detail in the experimental methods in section 4.2.2, using 2% SC/SDS. The process first involved annealing the SWCNTs at 300 °C to remove any amorphous carbon impurities. The SWCNT solution, 2% SC/SDS, was the sonicated for 4 hours to debundle and shorten the average SWCNT length, resulting in increasing the overall concentration of soluble SWCNTs. A short centrifugation step was employed to remove the bulk of heavy catalyst particles and heavy bundles and extract the isolated SWCNTs in supernatant. The next step in the purification process involved concentrating the SWCNT supernatant using

[1] The observed blue layer was visually more distinct than captured by the camera

centrifugal filters. The highly concentrated shortened SWCNTs should maximise the amount of SWCNTs that could undergo ultracentifugation in a single batch. A density gradient was prepared from 20%-40% iodixanol and Figure 4.6C shows the result of DGU performed on the concentrated SWCNT supernatant, with only a dense black band observed near the top of the centrifuge tube and some weaker grey layers formed lower down. This dense black band was extracted and termed "DGU-SWCNT". At each step in the process nanotube samples were extracted to compare their structural properties, diameter distribution, purity and magnetic properties and details of the analysis is given in section 4.3. The development of the multi-step purification could be applied to assist separation of semiconducting and metallic SWCNTs.

There are a number of factors which could influence the success of the separation process, the solubility of the nanotube, availability of ultracentrifuge and suitable fractionating equipment, the layering of the density gradient and the ratio of competing surfactants. The problem of solubility has been solved by the developed multi-step purification procedure and a combination of sonication, centrifugation and filtration has allowed highly concentrated soluble SWCNTs precursors to be produced. Restrictive factors for our DGU experiments were the limited time available on the ultracentrifuge and the fractionation process. For the separation of HiPCO SWCNTs a weak blue coloured band was observed, but insufficient volume could be extracted using a syringe, without cross contamination, to allow analysis of the band. The fractionation tools used by Arnold *et al.* would allow for precise extraction and would greatly improve the purity of isolated fractions. Performing continuous ultracentrifugation should allow bulk quantities of material to be produced and repeating the process on the separated samples would further improve

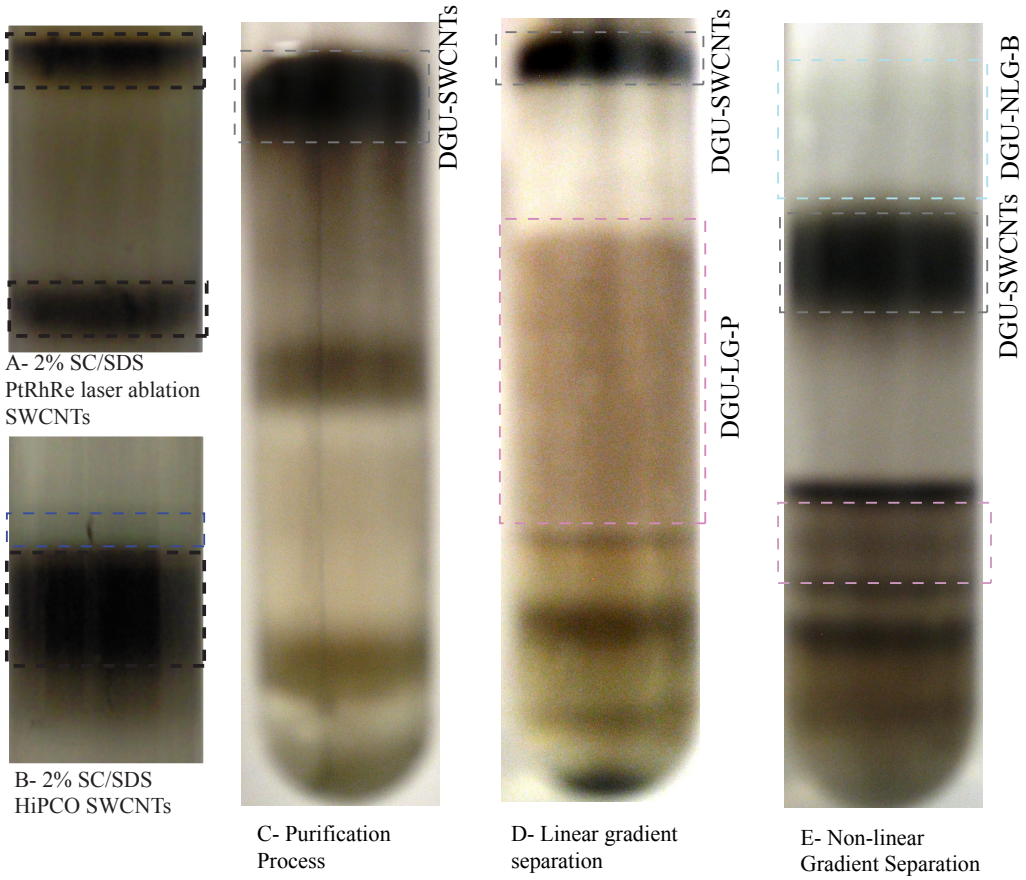


Figure 4.6: Visual images of the DGU process on (A) laser ablation nanotubes and (B) HiPCO SWCNTs (C) Employing purification protocol on 2% SC/SDS SWCNTs with 20%-40% gradient (D) Using linear gradient with combination of SC/DOC/SDS surfactants (E) Using a non linear gradient with with combination of SC/DOC/SDS surfactants

the purity. Yanagi *et al.* [166] successfully separated many different nanotubes with diameters up to 1.4 nm and their research suggested the additional use of another surfactant, deoxycholate (DOC), which is similar in structure to sodium cholate.

A density gradient was built from 20-40% iodixanol, containing a base 40% iodixanol layer 2ml, the nanotube layer was made up to 35% iodixanol layer volume 3ml, and the subsequent layers, 27.5%, 25%, 22.5% and 20% were all equal 1.5 ml layers. To attempt separation of laser ablation SWCNTs various combinations of surfactants, SC/DOC/SDS were exploited with varying results.

The most effective combination was using a 2% SC/DOC solution [ratio 4:1] in the SWCNT 35% iodixanol layer, and then building the linear gradient based upon 2% SDS/DOC [4:1 ratio]. A dense black band was visible near the top of the centrifugation tube. This dense black band was extracted and combined with DGU-SWCNTs sample. A weak purple coloured band was visible near the middle of the centrifuge tube, shown in Figure 4.6D, and was extracted and labelled DGU-LG-P. UV-Vis detection of DGU-LG-P showed an increase in the semiconducting band relative to the purified black DGU-SWCNT layer, however, there still remained signal from the M_{11} peak, as shown in Figure 4.7A. Comparing the metallic peak to the purified SWCNTs layer, the isolated DGU-LG-P layer showed a considerable decrease in the intensity of the metallic peak. Comparing the ratio of the S_{22}:M_{11} and S_{22}:M_{11} peaks, using the area of the curve, the purple DGU-LG-P layer had four times greater semiconducting content than that of the purified black SWCNT layer. Although the technique of DGU allowed separation to occur the limitation on the fractionation process which was employed resulted in some contamination between the layers, which may explain the remnants of metallic nanotubes in the observed purple DGU-LG-P layer.

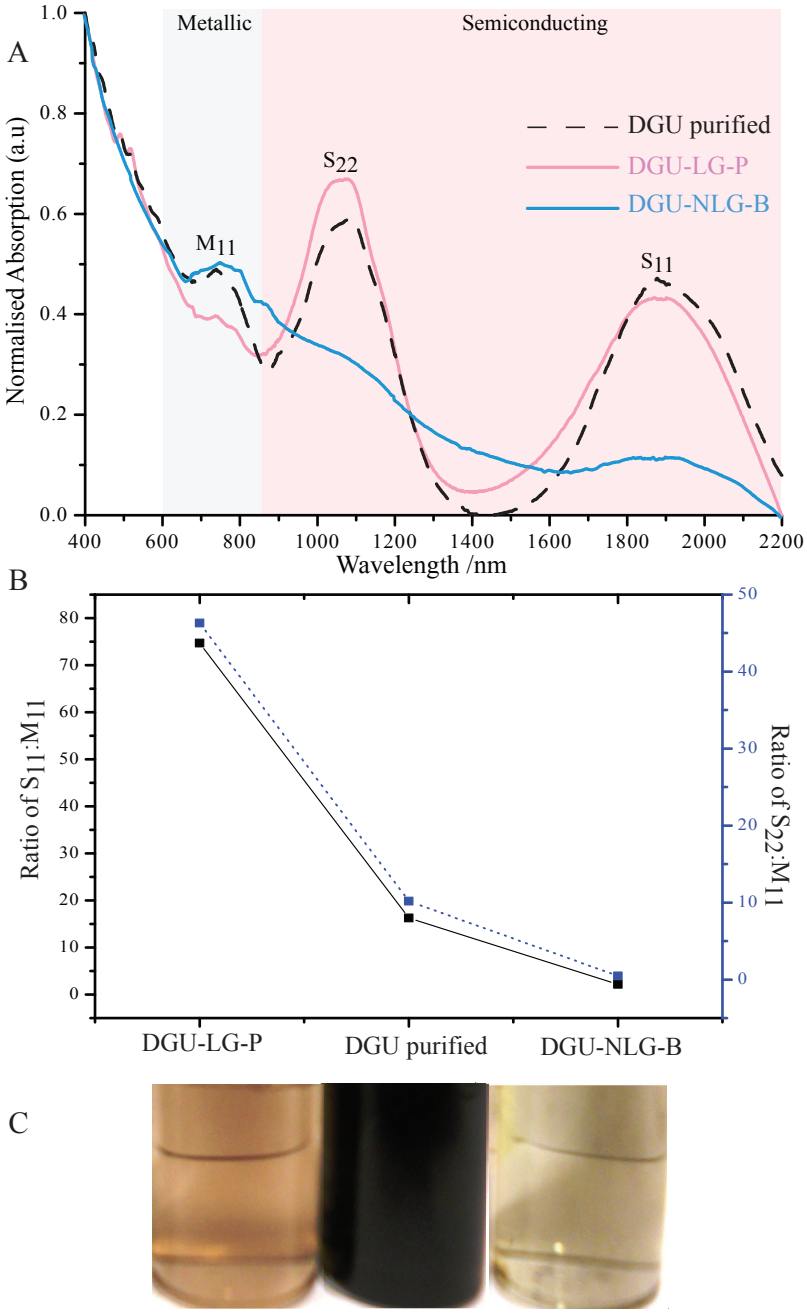


Figure 4.7: (A) UV-Vis normalized absorption of the separated purple DGU-LG-P and blue DGU-NLG-B layers compared with the purified DGU black nanotube layer. (B) Comparative analysis of the ratio of the semiconducting, S_{11} and S_{22}, and metallic, M_{11} peaks for the three samples (C) Image of the separated solutions showing difference in visual colour.

Another variation on the original density gradient centrifugation process is to use a non-linear gradient [170], which has much promise in providing further separation between materials with similar buoyancy. Ghosh *et al.* [170] showed that a tailored non-linear gradient could separate out enantiomers of chiral nanotube forms. Modifying our approach with a non linear gradient, the gradient ranged from 20-40% but the volume of each subsequent layer was modified to, 30% 1.2ml, 27.5% 1.4 ml, 25% 1.5 ml, 22.5% 1.6 ml and 20% 1.8 mL. The result of employing the non-linear gradient was the observation of a weak blue coloured layer, labelled DGU-NLG-B, appearing towards the top of the centrifuge tube, a dense black layer, extracted as DGU-SWCNTs, then a faint purple layer near the base of the tube (not clearly visible in photo), shown in Figure 4.6E. The nonlinear gradient increased the distance between each layer, allowing slightly easier fractionation with our limited tools. UV-Vis of the blue DGU-NLG-B layer showed considerable reduction in the observable S_{11} and S_{22} peaks, shown in 4.7, and the relative ratio of the S_{11}, S_{22} and M_{11} peaks were much lower than purified DGU SWCNTs, indicating that the majority of nanotubes are metallic.

Although DGU has shown to be effective to separate the semiconducting and metallic SWCNTs this approach did not seem feasible for the long term and the emergence of commercially available separated SWCNTs was an attractive alternative. The separation achieved in these experiments was hindered by the fractionation method, availability of ultracentrifuge and the overall yield. The fractionation approach employed by other groups requires specific equipment, which was unavailable, therefore a crude extraction was employed, which naturally resulted in some contamination of the layers. The approach around this was to repeat the DGU process on the obtained samples, however, due to limited experimental time on the cen-

trifuge it was difficult to explore the path. The separated SWCNT solutions were washed in MeOH and filtered and only a small amount of SWCNT powder was produced, not enough to go through the peapod production process. Since the primary objective of centrifugation was to obtain purified catalyst free samples, priority for centrifugation time was on producing purified material. Since the desired separated materials using laser ablation produced SWCNTs could not be produced, separated semiconducting and metallic nanotubes were purchased from Nanointegris.

The SWCNTs from Nanointegris were grown from arc-discharge using a combination of nickel, yttrium and iron metal catalysts. Figure 4.8 shows pictures of the isolated samples and the UV-Vis absorption spectra of semiconducting and metallic SWCNT thin film samples. The pictures of the samples, in 2% SC/SDS solution, show visual colour difference, with the semiconducting samples exhibiting a purple colour and the metallic samples exhibiting a blue colour. Semiconducting SWCNTs show strong S_{11}, S_{22} and S_{33} peaks and weak M_{11} peak. From the UV-Vis absorption spectra the mean diameter of the semiconducting has been calculated to be 1.38 nm, and a FWHM diameter distribution of 1.21 - 1.57 nm. The metallic SWCNTs show a strong M_{11} peak, with a mean diameter of 1.40 nm and a FWHM diameter distribution of 1.22 - 1.60 nm.

Centrifugation offers a direct strategy to purify SWCNTs, using the basics of centrifugal force to cause heavier catalyst particles to sediment. Although the separation of SWCNTs into semiconducting and metallic species was limited in success, the process is a proven method and in our case the option of purchasing samples was more feasible. There have been further improvements to the original DGU separation, with investigations into self generating density gradients, [171], which have isolated individual chiral form of nanotubes. Again these results are focused

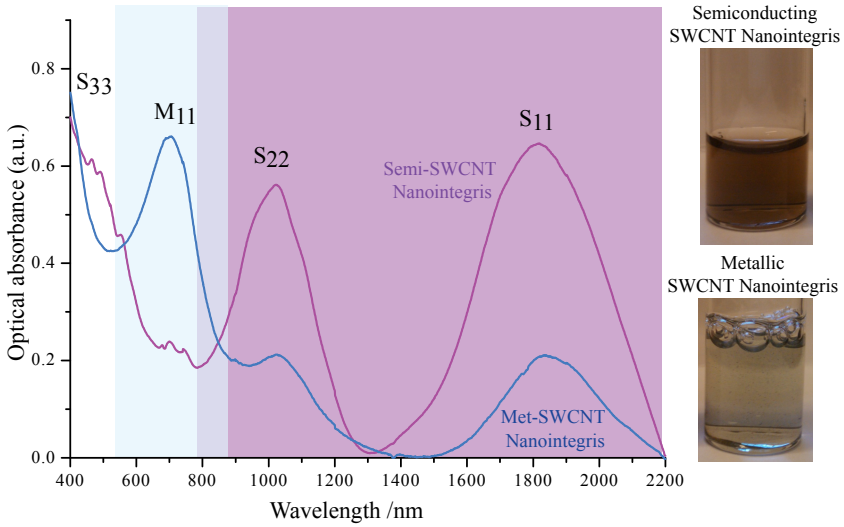


Figure 4.8: UV-Vis absorption spectra (normalized) of the separated semiconducting (purple) and metallic (blue) samples obtained from Nanointegris. Optical absorption was conducted on SWCNT thin films

upon narrow diameter CoMoCat or HiPCO nanotubes, where minimum overlap in optical absorption spectra can identify individual chiral NTs. Having obtained purified samples from different sources the structure and magnetic properties of these SWCNTs samples can be compared and the affects of filling the nanotubes with spin active metallofullerenes can be explored.

4.3 Analysis of Purified SWCNTs

SWCNTs purified by either ultracentrifugation or thermal annealing have been analysed by HRTEM, UV-Vis, AFM, EPR, VSM and Raman spectroscopy to understand the structure and composition of the purified nanotubes and compare the spin properties of SWCNTs with varying degrees of purification.

4.3.1 Nanotube Composition

HRTEM was performed to image the composition of all SWCNT samples in each of the purification methods, comparing the nanotube structure and the level of catalyst particles, amorphous carbon and defects present. Figures 4.9A-i and 4.9A-ii show the HRTEM images from the raw PtRhRe SWCNTs containing catalyst particles, amorphous and graphitic carbon. The SWCNTs were annealed in air at 300 °C for 2 hours to remove the carbon impurities surrounding the nanotubes. Figures 4.9B-i and 4.9B-ii show the annealed PtRhRe SWCNTs with reduced amounts of amorphous carbon either on the surface of the nanotube or surrounding the catalyst particles.

A solution of annealed SWCNT in 2% SC/DOC [4:1 ratio] was prepared and then sonicated for 4 hours. HRTEM presented in Figure 4.10A shows SWCNTs and catalyst particles coated with surfactant. Centrifuging the sonicated SWCNT sample for 1 hour at 41 krpm resulted in the supernatant (top 85%) containing dilute SWCNT solution and the bottom containing a residue of sediment SWCNTs. The "supernatant SWCNT", Figure 4.10B, shows a reduction in the amount of catalyst particles and more isolated SWCNTs. In contrast, Figure 4.10C, the "sediment SWCNT" sample, showed considerable increase in the level of catalyst particles. The supernatant SWCNT sample was further purified through a 17 hour ultracentrifugation using a 20-40% iodixanol density gradient based upon the DGU method explained in ref [107]. The resulting sample, Figure 4.10D, contains many isolated SWCNTs with almost no visible catalyst particles. The centrifuge purification process has been developed as an alternative method to the currently employed aqua regia purification method [92, 77].

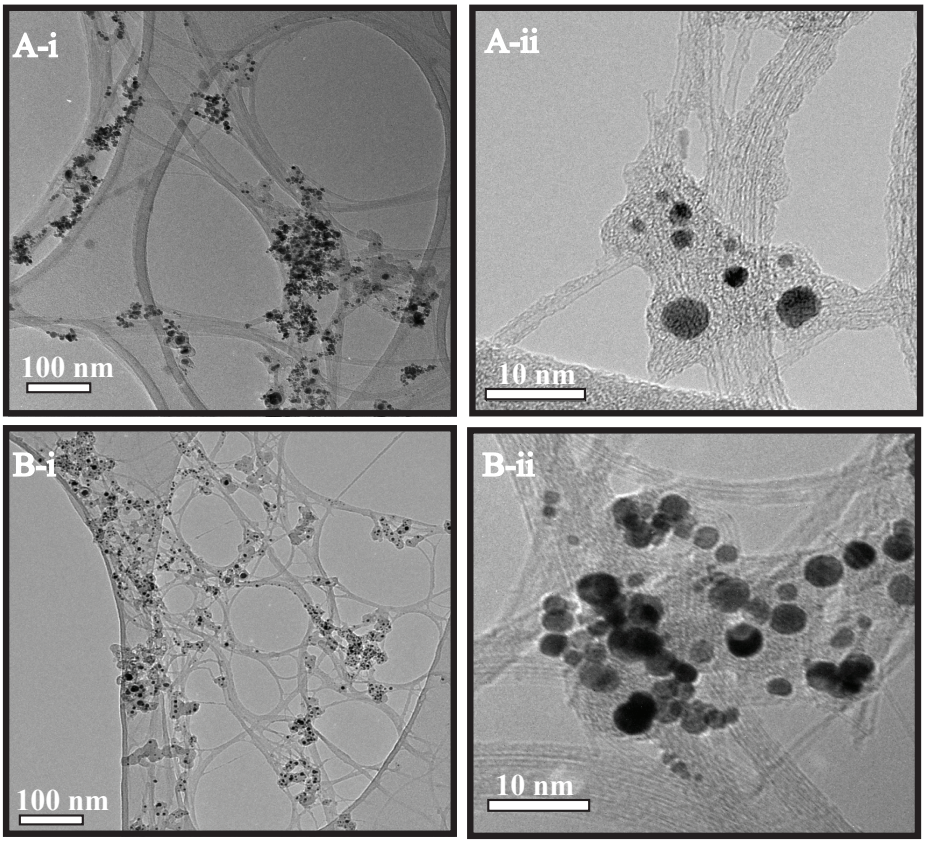


Figure 4.9: HRTEM images illustrating the composition of the SWCNT samples through the initial steps in the purification process.(A-i) Low magnification image of raw laser ablation PtRhRe SWCNTs (A-ii) High magnification image of raw SWCNTs showing amorphous carbon coating the nanotube surface (B-i) Low magnification image of annealed PtRhRe SWCNTs (B-ii) High magnification image of annealed SWCNTs showing clean nanotubes and catalyst particles

Aqua regia purified SWCNTs undergo microwave digestion to break down the graphitic carbon shells surrounding catalyst particles allowing aqua regia treatment to remove the catalyst particles. The purified SWCNTs contain clean nanotube bundles, as shown in Figure 4.11, but also contain a significant amount of catalyst particles.

Hot thermal annealing has been previously employed as a purification method for

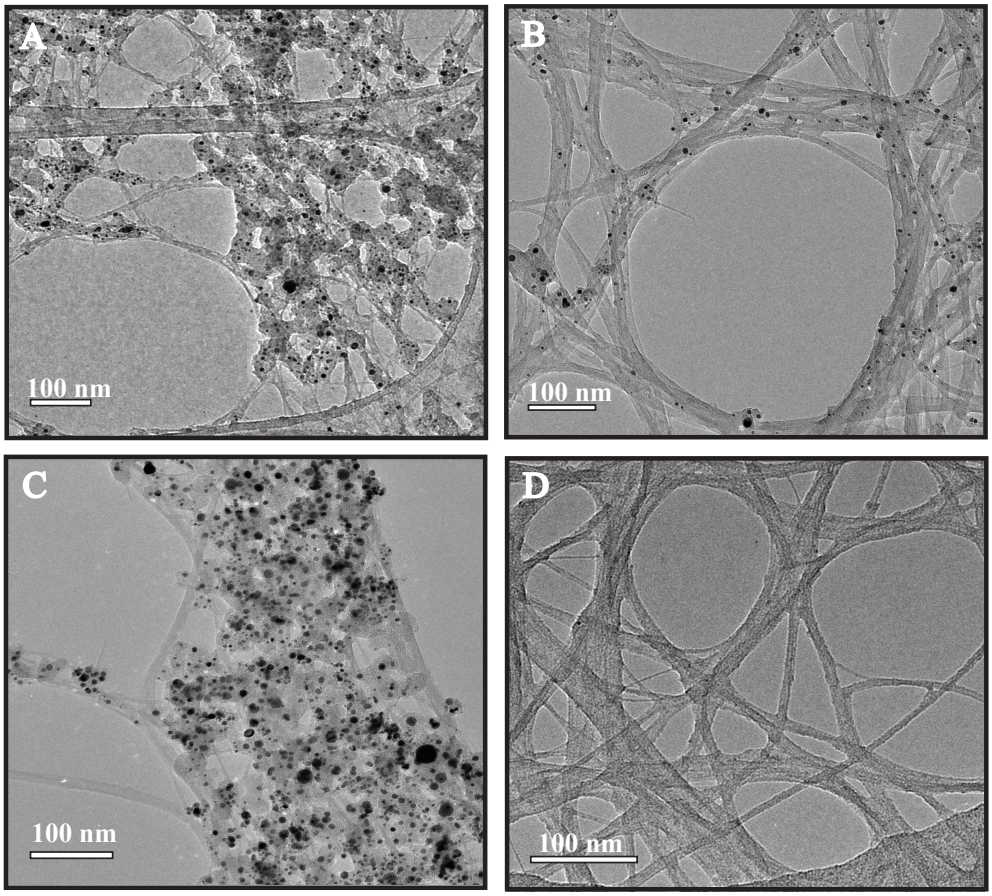


Figure 4.10: HRTEM images illustrating the composition of the SWCNT samples through each step in the purification process. (A) Sonicated PtRhRe SWCNTs coated with surfactant (B) Centrifuged SWCNT supernatant showing a reduction in catalyst particles (C) HRTEM image of centrifuged SWCNT sediment showing large clusters of catalyst particles (D) HRTEM image of DGU treated SWCNTs showing minimal catalyst particle content

arc-discharge nanotubes [168]. HRTEM of Meijo SO SWCNTs, shown in Figures 4.12A and B, indicates high quality SWCNT with a minute presence of residual catalyst particles. Figure 4.12C shows the HRTEM image of Meijo FHP CNTs with a combination of single walled and double walled nanotubes and almost no magnetic catalyst particles. Several hours were spent using TEM to scan a region of more

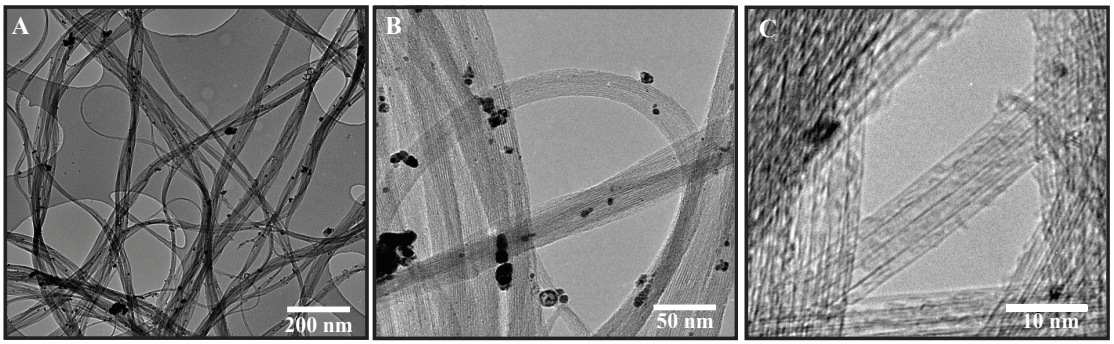


Figure 4.11: (A-C) HRTEM images illustrating the composition of the aqua regia purified SWCNT samples with increasing magnification. Samples show clean nanotube bundles with clusters of catalyst particles.

than 0.01 mm^2 of FHP SWCNT networks, and was found to be catalyst free. The Meijo FHP CNTs were refluxed in HNO_3 for 2.5 hours in order to produce defects [91] Figure 4.12D shows the refluxed Meijo FHP sample still retaining its nanotube structure and no magnetic particles visible.

4.3.2 Purity analysis using absorption spectroscopy

Van-Hove singularities in SWCNTs produce distinctive absorption peaks from semiconducting and metallic transitions. UV-Vis absorption spectroscopy was used to measure the absorption peaks from the metallic and semiconducting SWCNTs and yield information regarding the diameter distribution and purity of SWCNTs in the ultracentrifugation purification process. UV-Vis absorption of SWCNT films, between 400 - 2200 nm showed two semiconducting peaks, around $S_{11} \approx 1900$ nm and $S_{22} \approx 1050$ nm, and the first metallic peak, around $M_{11} \approx 700$ nm, as shown in Figure 4.5.

Comparison of the semiconducting and metallic peaks is a facile approach to de-

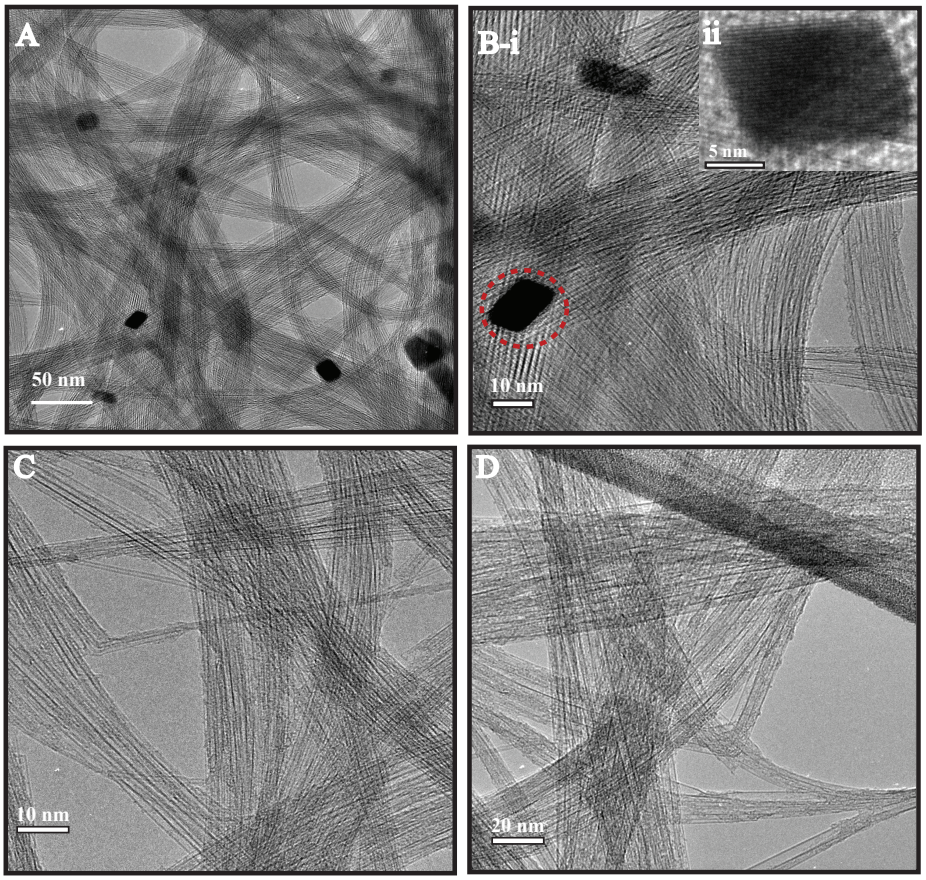


Figure 4.12: (A) Low magnification HRTEM image of Meijo SO SWCNTs showing clean nanotube bundles with some catalyst particles (B-i) HRTEM image of Meijo SO SWCNTs showing a residual catalyst particle, highlighted with dotted circle (B-ii) High magnification HRTEM of highlighted catalyst particle showing lattice fringes (C) Low magnification HRTEM image of large bundles of Meijo FHP CNTs with no visible catalyst particles (D) HRTEM image of Meijo FHP CNTs refluxed in HNO_3, showing bundles of CNTs maintaining pristine structure.

termine the level of separation from centrifuged samples. However, since the SWCNTs are coated with surfactants in H_2O, the absorption spectra contains a strong background signal from water, which peaks between 1400 and 1100nm, making it difficult to analyse the S_{22} peak. To overcome this problem homogeneous nanotube

thin films were produced which allowed complete analysis of the semiconducting and metallic optical spectra.

For comparative analysis the S_{22} peak was examined for all samples. Figure 4.13A shows the optical absorption spectra of the S_{22} peak for the sonicated SWCNT sample. The relative purity of the SWCNT sample can be calculated by measuring the area of the SWCNT absorption curve against the total area of absorption. A baseline subtraction allows the SWCNT absorption peak to be isolated. The S_{22} peaks for different SWCNT samples are shown in Figure 4.13B. The full width half maximum (FWHM) diameter distribution and the mean diameter can be calculated using the Kataura plot. The mean diameter remained consistent, approximately $\sim$ 1.45 nm, for all SWCNT samples in the purification process. The SWCNT sediment has the broadest FWHM diameter distribution of 0.45 nm, shown in Figure 4.13C, corresponding to SWCNTs between 1.23 - 1.68 nm. The SWCNT supernatant and DGU SWCNT material have narrower FWHM diameter distributions, 0.29 and 0.28 nm respectively, corresponding to SWCNTs between 1.36 - 1.65 nm and 1.37 - 1.65 nm respectively. The SWCNT sediment and sonicated SWCNT contain narrow nanotubes with diameter $\leq$ 1.2 nm. These narrow diameter nanotubes may bundle together and cause them to sediment. Centrifugation of SWCNT solutions should force heavy nanotube bundles to sediment, and isolated nanotubes to form in the supernatant.

The calculated SWCNT purity, shown in Figure 4.13D, measured the corresponding absorption of SWCNTs against impurities in the sample [152] and compared relative to the sonicated SWCNT sample. The relative purity increased for the centrifuged supernatant and DGU SWCNT sample. The sediment SWCNT sample has the lowest relative purity, which is reflective of the high levels of catalyst particles as

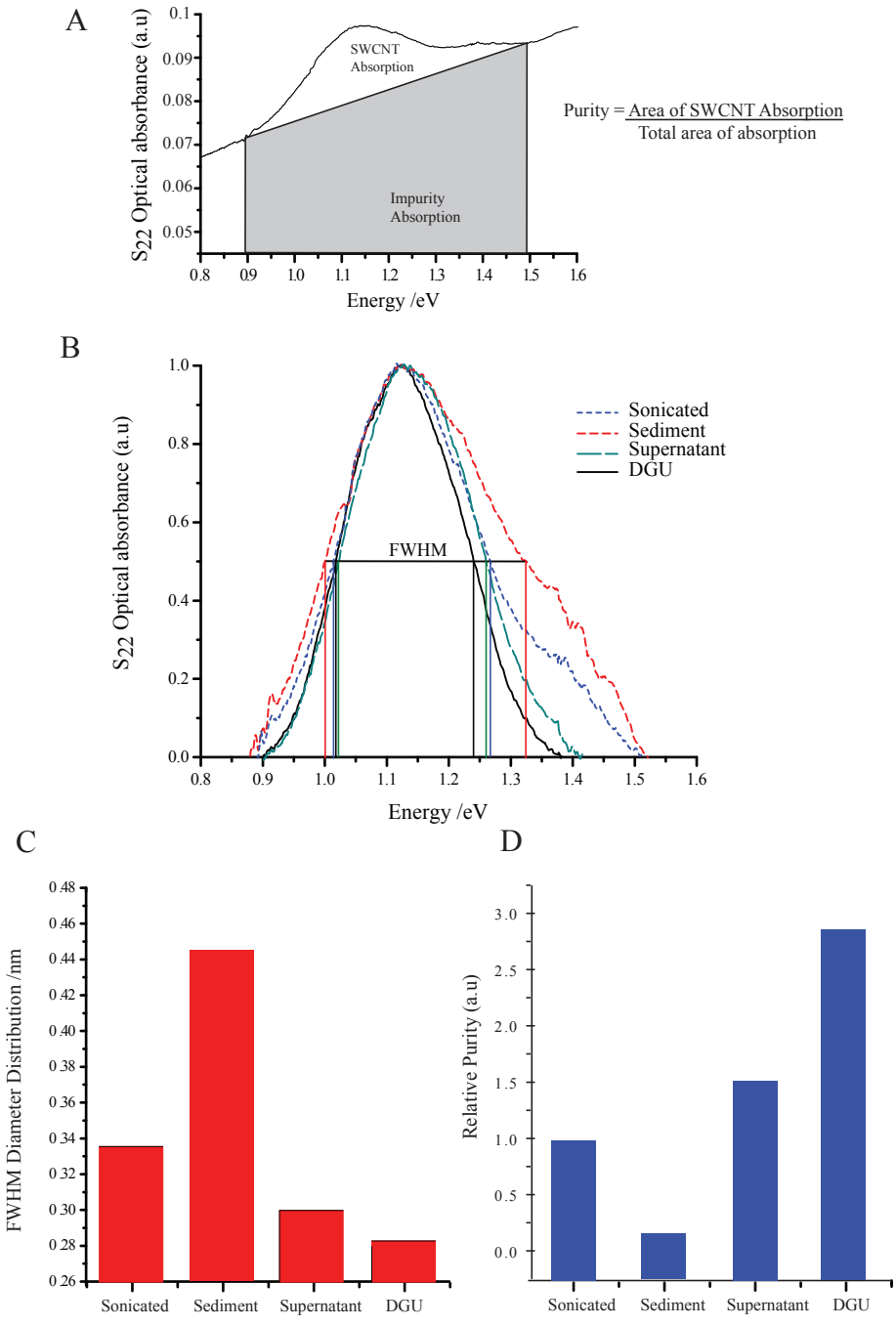


Figure 4.13: (A) Measure of the S_{22} peak of the sonicated SWCNT sample, showing the absorption from the SWCNT and impurities. The relative purity is determined by comparing the relative area of the SWCNT absorption against the total absorption. (B) UV-Vis absorption showing the normalised S_{22} peak for the SWCNT samples, indicating the FWHM for each sample. (C) FWHM diameter distribution for SWCNTs samples (D) Purity of SWCNT samples relative to sonicated SWCNTs sample

illustrated in the HRTEM, Figure 4.10C. Meijo FHP CNTs produced a broad UV-Vis absorption spectra due to a very large diameter distribution, therefore FWHM and purity could not be determined.

4.3.3 Structural Analysis

Atomic force microscopy (AFM) provided a further insight into the affects of the centrifugation purification process on the length and bundling of the PtRhRe SWCNTs. HRTEM only provides a qualitative idea of the length distribution of the SWCNTs samples, so it is important to use AFM as an additional analytical technique.

AFM of raw PtRhRe SWCNT, centrifuged SWCNT supernatant and Meijo FHP SWCNT are shown in Figures 4.14A-C respectively and analysed in Figures 4.14D and 4.14E. All samples were prepared in 2% SC/DOC [4:1 ratio] solution and to ensure good dispersions raw PtRhRe SWCNTs and Meijo FHP CNTs were sonicated for 1 hour. Raw PtRhRe SWCNTs have a mean length of 1.41 microns and the majority of nanotubes with length between 1-2 microns. For the SWCNT supernatant the distribution of nanotube lengths peaks at 0.5-1 microns with an average nanotube length of 0.77 microns. The shorter nanotube length is due to the 4 hour horn-tip sonication of the nanotube which is known to cut and shorten SWCNTs [172, 93]. The height profile distribution for raw PtRhRe peaks between 2-4 nm (i.e bundles), compared to the lower value of the SWCNTs supernatant, with the majority of the height profile distribution less than 2 nm. This indicates that the SWCNT supernatant contains principally isolated nanotubes, which is a direct result of the surfactant encapsulation and centrifugation of the SWCNT. Meijo FHP CNTs are much shorter in length than Raw PtRhRe SWCNTs, with a mean length of 0.57

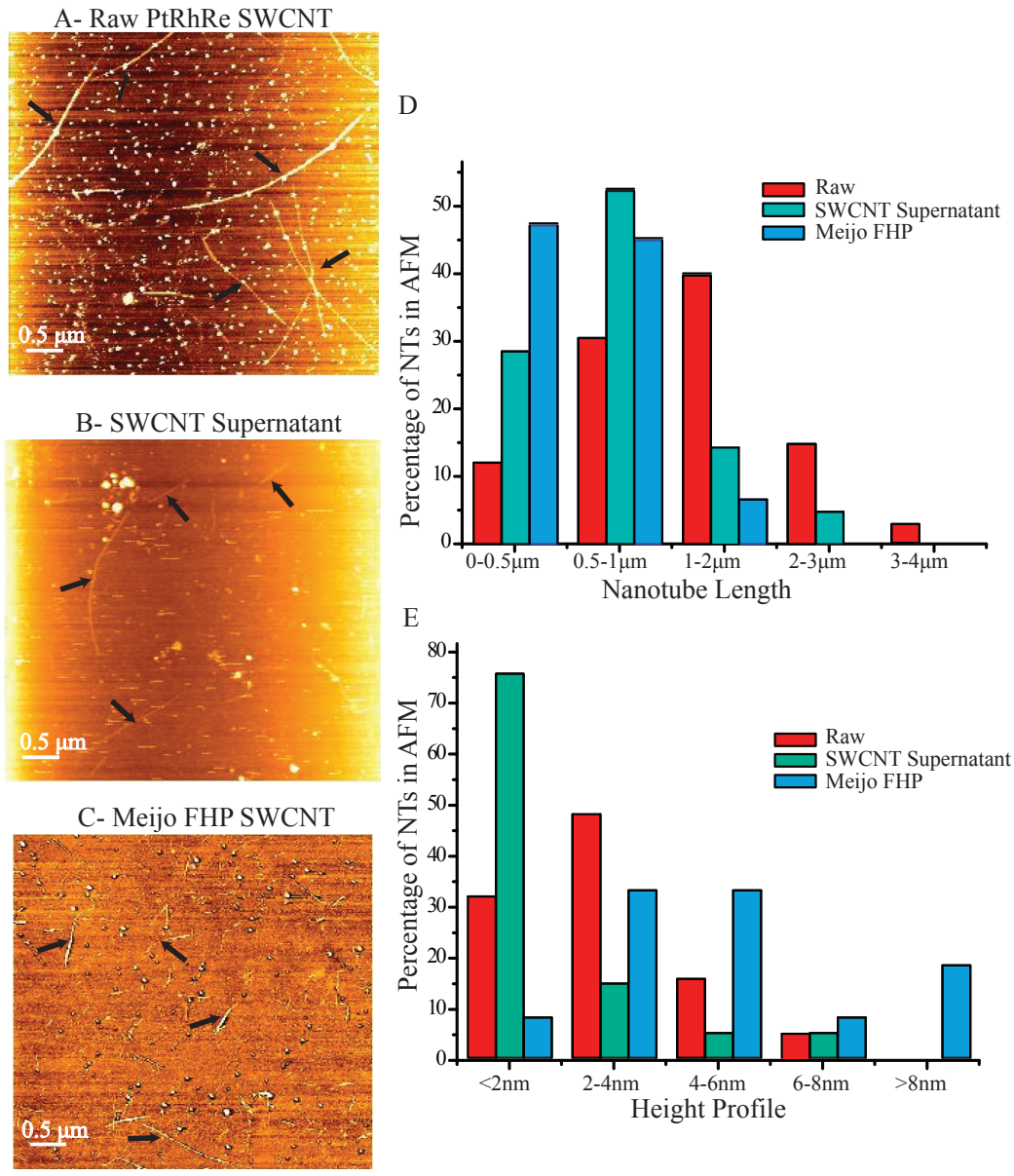


Figure 4.14: (A) AFM image of raw PtRhRe SWCNTs (B) AFM image of SWCNTs supernatant (C) AFM image of Meijo FHP nanotubes (D) Distribution of nanotube length for nanotube samples (E) Height profile distribution of nanotubes

microns. Meijo FHP CNTs have a larger height profile distribution compared to raw PtRhRe SWCNT, due to the larger diameter of the Meijo FHP CNTs and the presence of both single walled and double walled nanotubes. AFM data indicates that both supernatant SWCNTs and Meijo FHP NTs have sufficient mean length to produce isolated NT field effect transistor (FET) devices [137]. Percolated networks of short NTs, $\sim$ 200 nm mean length, have been employed to produce thin film transistors [173].

4.4 Spin properties

4.4.1 Electron Paramagnetic Resonance

X-Band CW EPR measurements for each of the SWCNT species in the centrifugation purification process were performed at 5 K using microwave power of $\sim$ 1 mW (below the saturation power of $\sim$ 2 mW). EPR samples were prepared with a similar quantity of SWCNTs in order to compare the relative number of spins. Figure 4.15 compares the EPR intensity of the various SWCNT samples. Raw PtRhRe SWCNTs, shown in Figure 4.15A, gave a strong single peak in the EPR, with a g-factor of 2.0034 $\pm$ 0.0005 and linewidth $\sim$ 3.0 $\pm$ 0.1 G, but when the SWCNTs were annealed this signal was greatly reduced and scarcely visible above the noise level. The loss of EPR signal was attributed to the removal of amorphous carbon in the annealing process.

Centrifugation of the sonicated PtRhRe SWCNT sample decreased the catalyst content and improved the purity of the SWCNT supernatant sample compared to the SWCNTs sediment. The sonicated and sedimented SWCNT samples show an

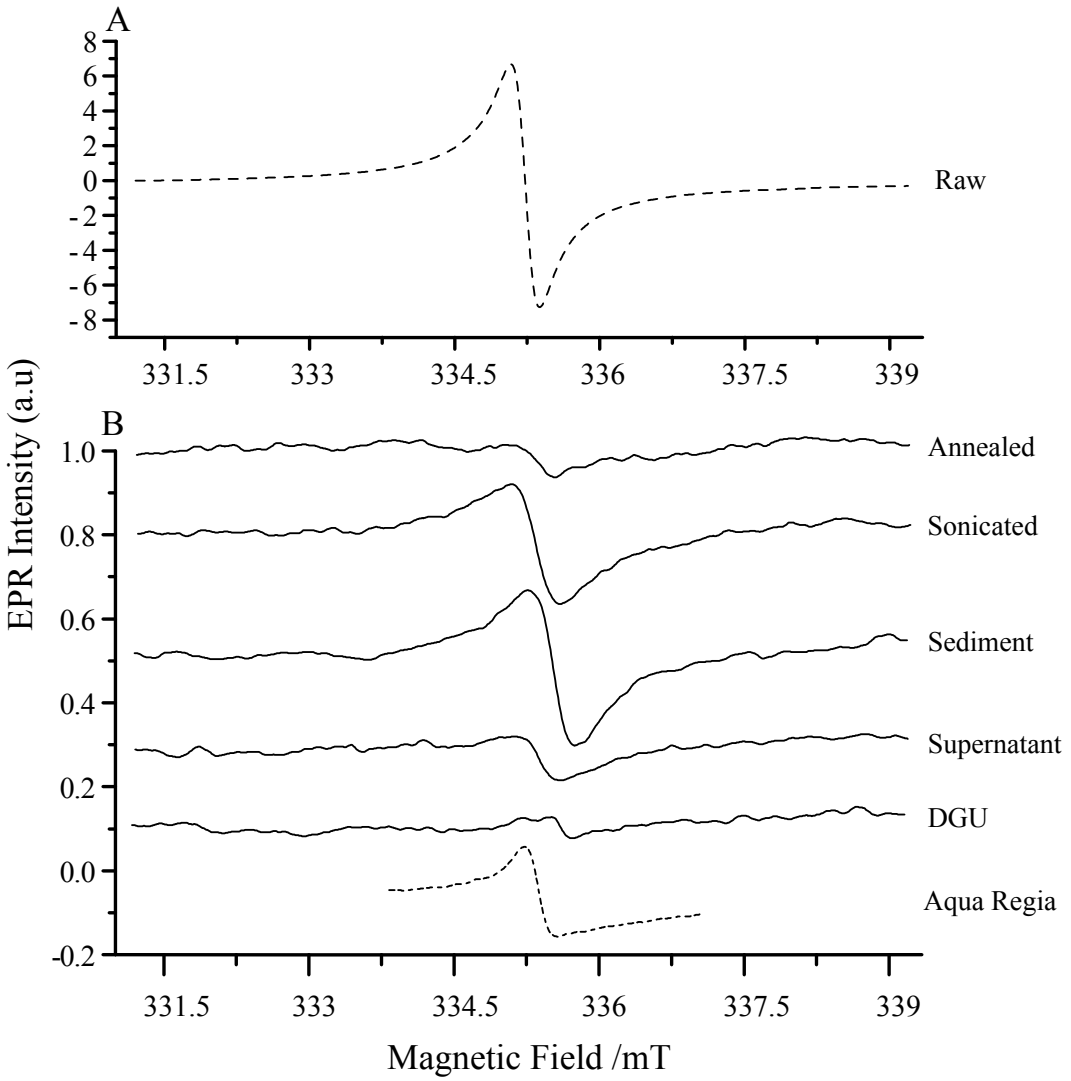


Figure 4.15: (A) 5K EPR spectra of raw PtRhRe SWCNTs. (B) 5K EPR spectra of annealed, sonicated, sediment, supernatant, DGU and aqua regia SWCNTs. (Microwave power: 1 mW; modulation frequency: 100 kHz; modulation amplitude: 1 G)

EPR signal, Figure 4.15B, with a Lorentzian lineshape and similar linewidths of $\sim$ 5.0 $\pm$ 0.1 G. The g-factor for sonicated and sediment SWCNTs are 2.0029 $\pm$ 0.0005 and 2.0017 $\pm$ 0.0005 respectively. The marginal difference is possibly due to bundling of nanotubes in the SWCNT sediment. The centrifuged supernatant shows negligible EPR signal with a similar g-factor of 2.0026 $\pm$ 0.0005 and linewidth of $\sim$ 5.0 $\pm$ 0.1 G. It can be deduced that the EPR signal is linked to the presence of catalyst particles present in the sonicated and sediment samples. DGU SWCNTs showed minimal EPR signal, further indicating that the observed EPR signal is related to presence of catalyst particles. SWCNTs purified by aqua regia microwave digestion have been shown to contain catalyst particles through HRTEM in Figure 4.12A. Figure 4.15B shows the EPR signal of the aqua regia treated SWCNTs, which is similar to the sonicated and sediment catalyst containing SWCNTs, emphasising the relationship between the catalyst particle impurities and EPR.

To further understand the nature of the spin signal observed for the raw, sonicated and sediment SWCNTs the power dependence was measured at 5 K. Figure 4.16 compares the susceptibility of raw, sonicated and sediment SWCNTs samples as a function of the microwave power. Raw SWCNTs saturate at a low power $\sim$ 1 mW, while the sonicated and sediment SWCNTs saturate at much higher microwave powers, indicating different spin relaxation times between the raw SWCNT and the sonicated and sediment samples. This difference maybe due to amorphous carbon impurities present in the raw SWCNT sample, while the EPR signal in the sonicated and sediment samples is attributed catalyst particles.

Figure 4.17 shows the EPR from Meijo SO SWCNTs, Meijo FHP and refluxed Meijo FHP CNTs. Low temperature (5 K) EPR measurements of Meijo SO SWCNTs show a large single peak with Lorentzian lineshape and a g-factor of 2.0012

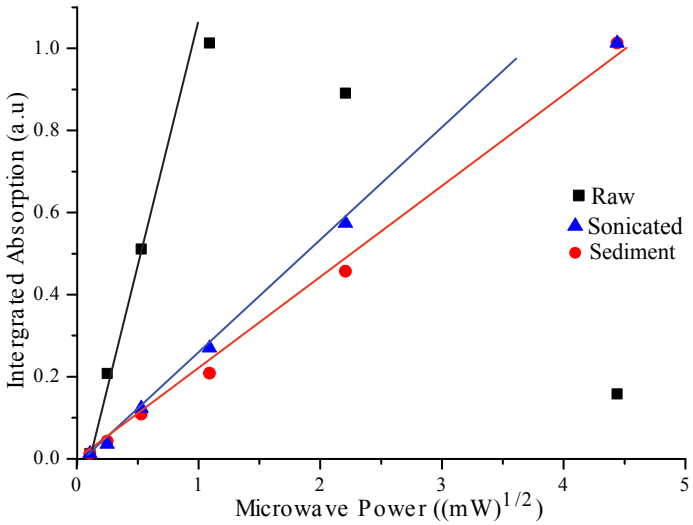


Figure 4.16: Comparison of the power dependence of the raw, sonicated and sediment SWCNTs (varying microwave power; modulation frequency: 100 kHz; modulation amplitude: 1 G)

$\pm$ 0.0005 and 5.1 $\pm$ 0.1 G linewidth. This EPR signal can be attributed to the presence of residual magnetic catalysts particles.

Meijo FHP CNTs have negligible magnetic catalyst particle content and contain a combination of primarily SWCNTs and some double and triple walled nanotubes and show no observable EPR signal. This further supports the notion that the SWCNT EPR signals observed at X-band are linked to the presence of catalyst particles. Meijo FHP NTs are clean catalyst free graphitic systems, differing from DGU SWCNTs as they are larger in diameter and contain double walled and triple walled nanotubes. Since no EPR signal is observed at X-band for either nanotube sample this suggests that changes in nanotube diameter and the number of walls does not produce an observable X-band EPR signal. Meijo FHP CNTs were refluxed in HNO_3, which is known to induce defects, and showed no EPR signal at low temperature, similar to the raw Meijo FHP sample, indicating the minimal effect of

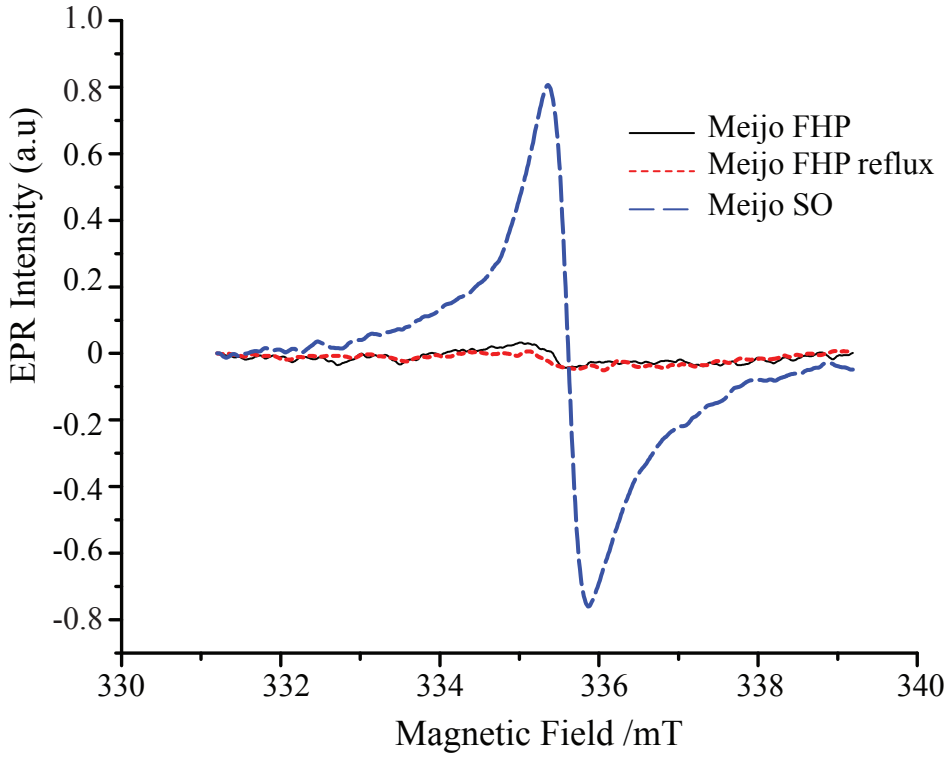


Figure 4.17: (A) 5K EPR of Meijo SO (dashed), Meijo FHP (solid) and refluxed Meijo FHP (dotted). (Microwave power: 1 mW; modulation frequency: 100 kHz; modulation amplitude: 1 G)

the induced defects on the EPR signal.

To further confirm the notion that ultra-pure SWCNTs do not produce an observable signal in low temperature (5K) EPR at X-band, 95% purified semiconducting and 95% purified metallic SWCNT samples, produced by Nanointegris using the DGU method [107], were examined. No signal was observed from these samples as shown in Figure 4.18. This reveals that the EPR associated with possible conduction electrons is not seen at X-band and may require larger field strengths and higher microwave frequencies.

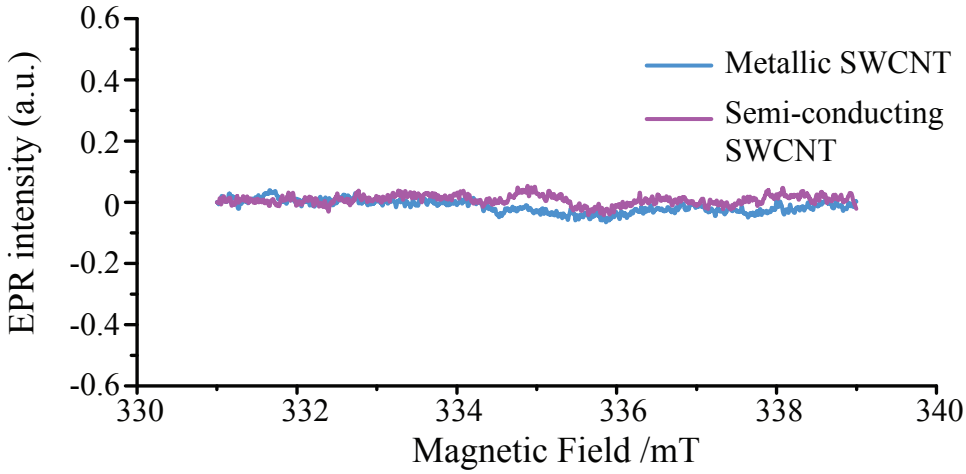


Figure 4.18: 5K EPR of metallic SWCNT (blue) and semiconducting SWCNT (purple). (Microwave power: 1 mW; modulation frequency: 100 kHz; modulation amplitude: 1 G)

4.4.2 Vibrating Sample Magnetometer

A vibrating sample magnetometer (VSM) was used to characterize the magnetic properties of the nanotube samples by measuring any magnetization arising from magnetic catalyst particles and to further demonstrate that Meijo FHP nanotubes were free from magnetic catalyst particles. Figure 4.19 shows the VSM of raw PtRhRe, Meijo FHP and Meijo SO SWCNTs. The PtRhRe catalyst particles are non-magnetic and therefore no magnetization curve is observed in the VSM. Meijo SO and FHP CNTs are synthesized using ferromagnetic catalysts, Ni/Y and Fe respectively and undergo high vacuum thermal annealing with the aim of removing catalyst particles [168]. Meijo SO SWCNTs are single walled and have a similar diameter distribution to raw PtRhRe SWCNTs. VSM of Meijo SO SWCNTs shows trace amounts of catalyst particles, as determined by the weak hysteresis curve.

As a comparison, the inset in Figure 4.19 shows the VSM of Carbolex SWCNTs heavily coated with ferromagnetic catalyst particles; the strong hysteresis curve is indicative of the presence of soft magnetic catalyst particles (cf. ref [174]). Meijo FHP nanotubes are of a larger diameter and contain single walled and double walled nanotubes. They are more stable to higher temperature annealing, resulting in maximum removal of magnetic catalyst particles. They therefore show no magnetic signals in VSM. These observations account for the origin of the detected EPR signal in Meijo SO SWCNTs, which contain magnetic catalyst particles, and the absence of any EPR signal for catalyst particle free Meijo FHP NTs.

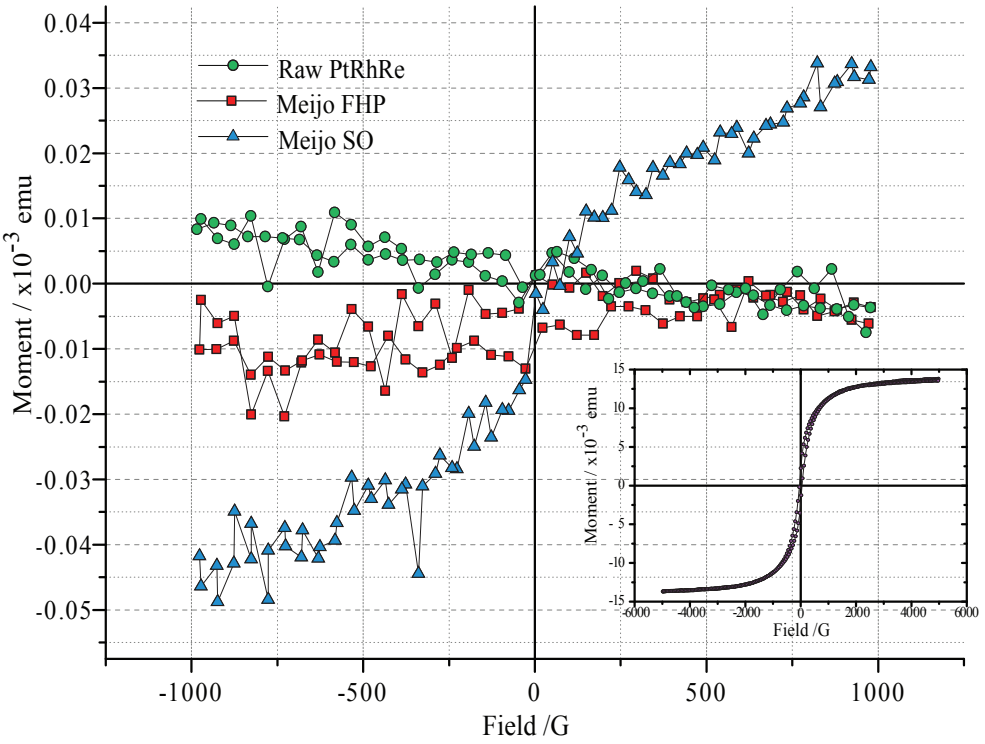


Figure 4.19: VSM of raw PtRhRe (circle), Meijo FHP (square) and Meijo SO (triangle) SWCNTs. Inset VSM of Carbolex raw SWCNTs containing many catalyst particles

4.4.3 Raman Spectroscopy

Raman spectroscopy, shown in Figure 4.20, was performed at 532 nm to measure the G and D peaks of the SWCNT samples to determine any effects the centrifugation purification process had upon SWCNTs defects. The ratio of the D peak (∼1330 cm^{-1}), defects in sp^2 carbon network, and the G peak (∼1590 cm^{-1}), arising from semiconducting and metallic nanotubes, is used to measure the degree of disorder in the SWCNTs [155]. D/G ratios were obtained for DGU SWCNTs, 0.059, and raw SWCNTs, 0.058, while smaller D/G ratios were obtained for Aqua regia treated SWCNTs, 0.028, and Meijo SO SWCNTs, 0.032. The D peak for DGU SWCNTs maybe slightly higher due to the horn-tip sonication process which may create defects in the process of cutting nanotubes. The relatively low D/G ratio for all the SWCNTs samples illustrates the high quality of the SWCNTs [155, 175].

4.4.4 Paramagnetic Properties

Purified DGU SWCNTs and Meijo FHP NTs free from catalyst particles show negligible EPR signals at the X-band. EPR signals were only detected in samples containing catalyst particles indicating there may be some interactions between the metal catalyst and the surrounding carbon which contributes to the EPR signal. Nicolau *et al.* [176] investigated the paramagnetic behaviour of platinum catalyst deposited on charcoal. They investigated several compositions of platinum and charcoal and found that mixed Pt-C complexes produced EPR signals, with linewidths between 3.9 and 5.4 G and a g-factor of 2.0034. This is around that of a free electron and is similar to the observed g-factors in Figure 4.15 and 4.17. The observed EPR signal was attributed to interaction between charcoal and the platinum, and a rela-

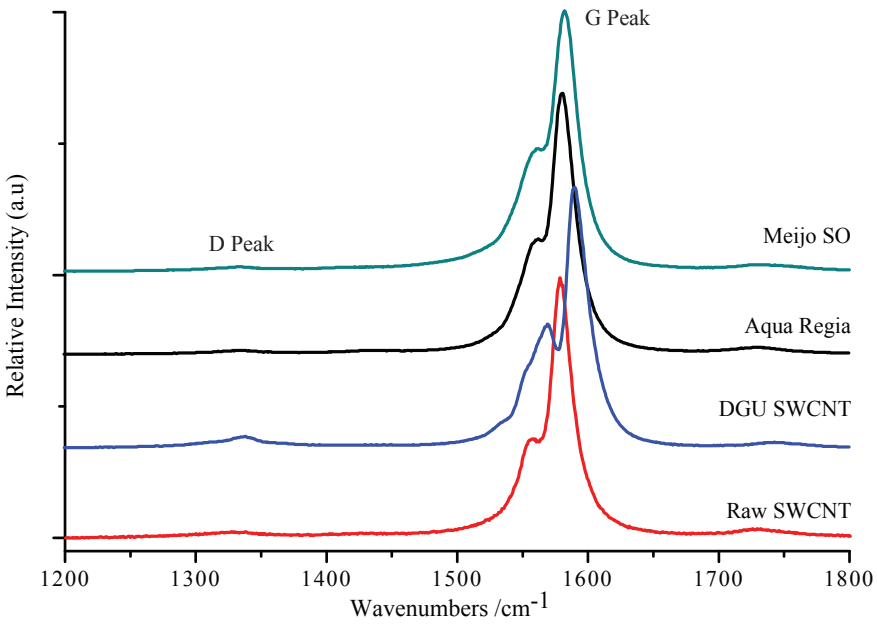


Figure 4.20: Raman spectroscopy of Raw SWCNTs, DGU SWCNTs, Aqua regia SWCNTs and Meijo SO SWCNTs showing the G peak ($\sim$1590 cm^{-1}) and D peak ($\sim$1340 cm^{-1})

tionship between the EPR intensity and platinum content was observed, indicating that electrons remain unpaired on the platinum catalyst. These observations facilitate an understanding of the obtained EPR signals in our experiments. Annealing raw PtRhRe SWCNTs removes amorphous carbon surrounding the nanotube and catalyst particle surface. The cleansed catalyst particles have reduced Pt-C interactions with the removed amorphous carbon, explaining the absence of an observable EPR signal for annealed SWCNTs. Wang *et al.* [177] performed density functional theory (DFT) calculations to ascertain the binding energies of Pt clusters on carbon nanotubes. Binding energies on point defects on CNTs were determined to be more than three times higher than on defect free CNTs. Stronger orbital hybridization between Pt atoms and carbon in defective CNTs was determined to cause the in-

crease in the binding energy. Importantly Wang *et al.* elucidated that larger charge transfer occurred between Pt and carbon in defective CNTs. Sonication of SWCNT surfactant solution has been shown to cut nanotubes and Lu *et al.* elucidated the mechanical damage that can potentially arise from ultrasonication, producing defects in the nanotube structure [178, 177, 93]. Shorter nanotubes with potential defects could provide more preferential binding sites for Pt catalyst particles to interact with the CNT and provide an explanation of the reappearance of an EPR signal for the sonicated SWCNTs sample. The sonicated SWCNT sample was centrifuged, producing two SWCNTs systems with varying Pt catalyst content, as determined by HRTEM. An EPR signal is observed for sediment SWCNTs, heavily coated with catalyst particles, due to the Pt-C interactions. Supernatant and DGU SWCNTs, containing predominantly nanotubes, yielded no observable EPR signals at X-band frequencies due to the absence of Pt-C interactions. Observed EPR signals arise from the interaction between the Pt catalyst particle and the CNTs and centrifugation has successfully demonstrated an avenue to reduce catalyst content from the nanotube system [175, 176]. High vacuum thermal annealing of magnetic catalyst particles from Meijo FHP CNTs highlighted another approach to remove catalyst particles, which otherwise produce a EPR signal as seen for Meijo SO SWCNTs [168, 164]. Meijo FHP CNTs have been shown to be a pure graphitic system, an ideal nanotube structure which has been lacking in preceding EPR studies, and showed no trace of conduction electrons. Theoretical calculations predict a doublet peak for SWCNTs EPR due to spin-charge separation, however, neither of our purified samples show this phenomenon at X-band frequencies [179]. Kuemmeth *et al.* [180] measured spin orbital coupling of 84 GHz for a single 5 nm diameter SWCNT [180]. Based upon their measurement of the spin orbit (SO) coupling and the theoretical study

of ref [181], the SO coupling can be estimated for the nanotubes studied here (DGU SWCNTs diameter $\sim$ 1.4–1.6 nm, and Meijo FHP NTs, diameter $\sim$2nm) to be approximately 260–300 GHz and 190–230 GHz respectively. Given these values for SO coupling, no EPR signal is expected from the conduction electrons at X-band frequencies (10 GHz) and at a modest magnetic field. Furthermore the range of nanotube diameters could lead to substantial broadening and therefore make it difficult to observe any signal. Studying aligned SWCNTs at higher EPR frequencies could reveal the conduction electron spin resonance. Attempts to perform high frequency EPR experiments were carried out at the IFW Dresden with Dr. V. Kataev and Ferdinand Lipps. Using their custom setup, a range of frequencies between, 249–498 GHz were measured at low temperature, sweeping a field of 14 T. However, no signal could be resolved from metallic SWCNTs against the strong background noise generated at low temperatures.

4.5 Summary

The multi-step centrifugation purification process has successfully produced highly pure SWCNTs which can be implemented in spintronic devices. Centrifugation of SWCNT solutions provides an effective approach to remove catalyst particles compared to aqua regia treatment. HRTEM, UV-Vis and AFM provided evidence for the significant improvements of the SWCNTs through each step in the purification process. EPR tracked any modifications the purification methodology had on the spins in the SWCNT sample. The comparative analysis of the sediment and supernatant SWCNT samples has revealed that metal catalyst carbon complexes were the cause of the observable EPR signal. HRTEM and UV-Vis established the difference

between the two samples. The SWCNT sediment contained a substantial amount of catalyst particles and the SWCNT supernatant contained more isolated SWCNTs with considerable reduction in catalyst particle content and a narrower diameter distribution. EPR of the two contrasting SWCNT samples highlights a strong correlation between the level of catalyst particles and the detected EPR signal. Purified supernatant and DGU SWCNTs show no EPR signal at X-band frequencies, where as the sonicated and sediment SWCNTs, containing higher levels of catalyst particles, both produced an EPR signal. Aqua regia purified SWCNTs contained residual catalyst particles and therefore produced an EPR signal. Ultracentrifugation of raw PtRhRe is a viable method to obtain catalyst free SWCNTs. Meijo SO and FHP NTs illustrate analogous results. High thermal annealing of Meijo FHP NTs purged magnetic catalyst particles, as shown in VSM, whereas Meijo SO still showed the presence of remnant magnetic particles in VSM. Meijo FHP nanotubes are highly pure, with HRTEM and VSM giving no indication of any catalyst particle present in the sample. The presence of catalyst particles in Meijo SO is linked to the EPR in Figure 4.17A, with the magnetic catalyst free Meijo FHP CNTs showing no EPR signal. Ultracentrifuged separated metallic and semiconducting SWCNTs did not show any detectable EPR signal at X-band frequencies either. In general high-quality ultra-pure SWCNTs do not exhibit an EPR signal at X-band frequencies, and that signals detected arise from metal catalyst particles interacting with carbon or in poor quality SWCNTs samples.

Chapter 5

Metallofullerene Spin Properties

5.1 Introduction to Metallofullerenes

Metallofullerenes (MFs), encapsulated metal atoms inside a fullerene cage [27, 43] shown in Figure 5.1, have many unique properties due to the charge transfer from the metal atom to the fullerene cage. In the case of La@C_{82}[182], Sc@C_{82} [37, 42] and Y@C_{82} [42], an unpaired electron is delocalized across the cage and interacts with the metal atom. This results in hyperfine coupling between the electron spin and the nuclear spin of the metal atom, which can be detected through electron paramagnetic resonance (EPR) spectroscopy. The hyperfine splitting in the EPR signal is highly sensitive to the changes in the local environment and can reveal interactions such as inter-fullerene exchange coupling or dipole-dipole interactions. The relatively long spin lifetimes of Sc@C_{82}, and La@C_{82} [7] makes them promising candidates as spin qubits for quantum information processing (QIP) [6] and in spintronic applications. The wavefunction of the unpaired electron in Sc@C_{82} and La@C_{82} extends out partially from the fullerene cage and this makes it prone to inter-fullerene

spin interactions such as exchange coupling that occur with wavefunction overlap between neighbouring spins [183, 184]. Inter-fullerene exchange interactions can be enhanced by forming solid state systems that force nearest neighbour interactions. Understanding the inter-fullerene spin dynamics in spin-active metallofullerenes is important for their future integration into solid-state devices.

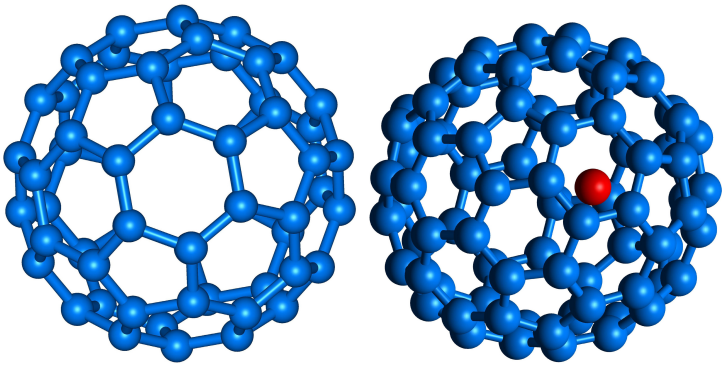


Figure 5.1: Schematic diagram of a empty caged C_{60} and a M@C_{82} metallofullerene

Macroscopic fullerene crystals and single-walled carbon nanotube (SWCNT) peapods are two possible avenues for assembling solid-state architectures to induce spin interactions in 3D (crystals) and 1D (peapods). Previous studies on pure macroscopic MF crystals have shown very broad EPR spectra resulting from strong inter-fullerene spin interactions [185]. The majority of research about the EPR properties MFs has been carried out in solution [186], where spin interactions are minimal and the MFs can be easily interpreted as an isotropic spin system, and then frozen in solution to probe the anisotropic behaviour. Diluting the spin-active MFs in a C_{60} crystal effectively dopes the crystal with spins and should lead to increased separation between neighbouring spins and consequently a reduction in the inter-MF spin interactions. This approach should enable control of the spin dynamics of isolated MFs in a diamagnetic C_{60} matrix and provides a deeper understanding of the nature

of spin interactions.

5.1.1 MF Spin Properties

Electron transfer to the carbon cage facilitates the study of the paramagnetic nature of endohedral metallofullerenes. Group 3 (Sc, Y and La) metallofullerenes exhibit hyperfine structure in the EPR spectrum, in the forms; Sc@C_{82}, Y@C_{82} and La@C_{82}. Johnson *et al.* [50] investigated the paramagnetic nature of La@C_{82} metallofullerenes. The observed g value, 2.0010, was consistent with a fullerene anion and a La atom in the 3^+ state. From the EPR spectrum it was deduced that La ($5d^26s^1$) donates its three valence electrons to the fullerene cage, occupying the LUMO and LUMO^{+1}, with the unpaired electron in the LUMO^{+1} of the fullerene cage, forming a $La^{3+}@C_{82}^{3-}$ complex, illustrated in Figure 5.2. Analogous work has been produced for Y@C_{82} [187, 54], the EPR spectrum consisting of two strong lines from the hyperfine coupling, where the nuclear spin of yttrium is 1/2. Again a g value of 1.9999, similar to a fullerene anion, indicated the presence of the unpaired electron on the fullerene cage and also the 3^+ state of the yttrium atom. The Sc($3d^14s^2$) atom will donate two 4s electrons to the LUMO of the fullerene cage and shows strong hybridization between the 3d electron and the π orbital of the C_{82} cage. Most other metallofullerenes are EPR silent or show very fine structure at low temperatures.

5.1.1.1 Spin Interactions

The main interactions which may be observed from conducting EPR of endohedral metallofullerenes are hyperfine, exchange and dipole-dipole interactions. A schematic representation of each of the interactions is shown in Figure 5.3.

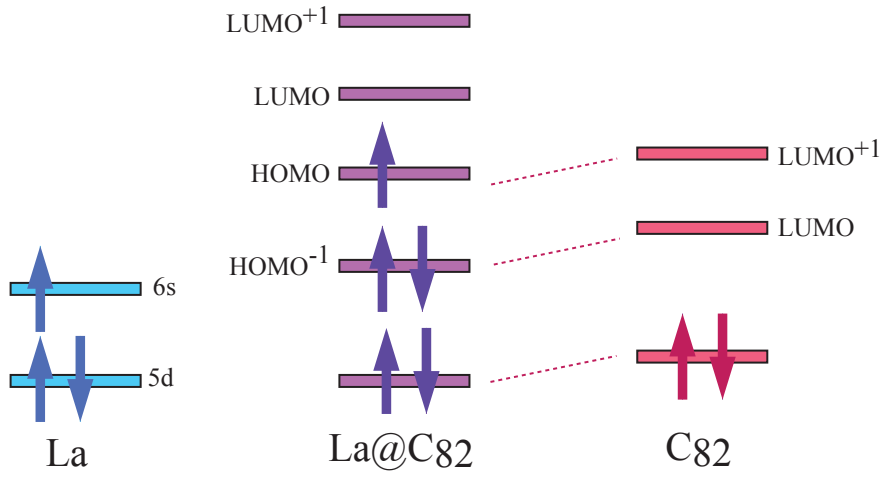


Figure 5.2: Schematic diagram of interaction between the La ($5d^26s^1$) electrons and the C_{82} fullerene cage

Hyperfine interaction

The unpaired electron from the La@C_{82} cage will interact with the nuclear spin of the La atom, which is 7/2 (the same as with Sc). This interaction will split the electron spin Zeeman levels into a further 8 energy levels. The allowed transitions are seen in the EPR spectra as eight evenly spaced lines, as experimentally determined by by Johnson *et al.* [50], split evenly by a hyperfine constant *a*.

Exchange Interaction

The Heisenberg exchange interaction, J, occurs between two electrons from neighbouring metallofullerene cages. The exchange interaction results from the overlapping wave functions of the unpaired electrons. Since the exchange interaction is brought about by wave function overlap this interaction is short range. The phenomenon of exchange narrowing [188], predicts that large exchange coupling will cause the signal to narrow and the hyperfine to be lost.

Dipole-Dipole Interaction

Dipole-dipole interactions can occur between the electron magnetic moments of interacting electron spins and can considerably alter the observed EPR spectra, often leading to the broadening of the EPR signal [189]. The energy of the dipole-dipole interaction is governed primarily by distance of the magnetic dipoles of the two electrons, which is proportional to $1/r^3$ and has an angular dependence.

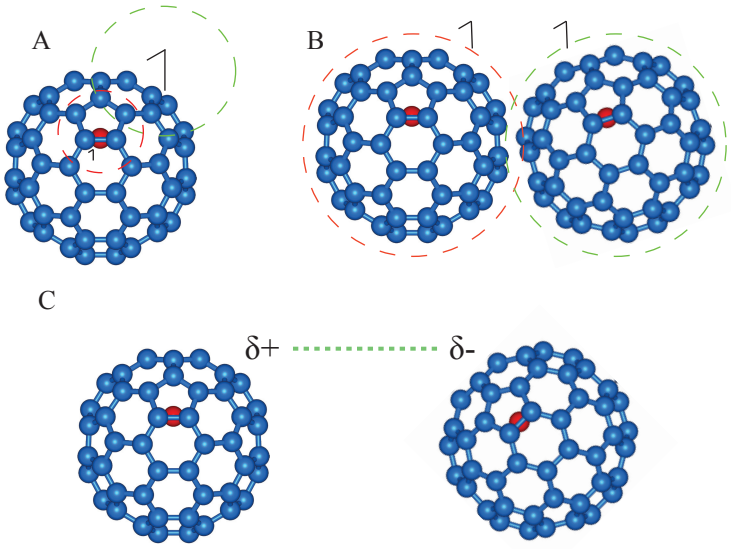


Figure 5.3: Schematic representation of interactions which can occur in metallofullerene systems (A) hyperfine interaction (B) exchange interaction and (C) dipole-dipole interaction

5.2 EPR investigations

EPR investigations look to understand the nature of the interactions between metallofullerene spins within different carbon environments. This was addressed by first analysing spin-spin interactions between metallofullerenes in 3D crystals, which will ultimately aid in the understanding of the spin properties in peapods. Previous studies on pure macroscopic crystals have shown very broad EPR spectra resulting

from strong inter-fullerene spin interactions [185], or investigated the dilute spin limit in solution, where spin interactions are negligible [190, 191]. To explore the region between these limits, spin-active fullerenes were diluted within a matrix of diamagnetic C_{60}. This permits the tuning of mean fullerene separation and thus inter-fullerene spin interactions. The results demonstrate that exchange interactions between MFs occur in C_{60} crystals and can be controlled by varying the molar concentration of MFs in C_{60} from 0.8% to 100%.

5.2.1 Experimental methods

Metallofullerenes (MFs) of La@C_{82} [27], Sc@C_{82} [45, 16, 32] Ce@C_{82} and Y@C_{82} [54], consisting of a fullerene cage and encapsulated metal atom, possess many unique electronic and optical properties due to the charge transfer from the metal atom to the fullerene cage [192]. Metallofullerenes M@C_{82} [M=La, Sc, Ce and Y] were produced using the arc-discharge method [192]. The MFs were purified by HPLC and characterized using MALDI-TOF mass spectroscopy. For experiments, the concentrations of the various MFs sample were determined through UV-Vis absorption spectroscopy [60]. UV-Vis spectra of Sc@C_{82}, showed different absorption peaks to La@C_{82} and Y@C_{82} due to the difference in charge transfer from the metal atom to the fullerene cage. MF doped C_{60} crystals were formed by slowly removing the solvent from a CS_2 solution of known C_{60}:MF concentration under vacuum. All samples for EPR were degassed and sealed in a quartz tube under vacuum. The number of MFs was kept constant and the amount of C_{60} varied to obtain different concentrations. EPR measurements were performed using a Bruker EMX spectrometer at 9.4 GHz in the 5 - 300 K temperature range using an Oxford ESR900 cryostat.

5.2.2 EPR results La@C_{82}

Figure 5.4A shows EPR spectra of La@C_{82} diluted in C_{60}, with a molar La@C_{82}:C_{60} concentration range between 0.8% and 100%. At a low concentration of 0.8% hyperfine structure of the La@C_{82} is well resolved and as the concentration increases the hyperfine structure becomes broader and a single narrow peak emerges from the center. At concentrations over 20%, all of the hyperfine structure is lost and only the single peak remains. At a concentration of 100%, the EPR spectra consisted of a single broad peak with linewidth of 12 G, contrary to previous reports [133]. This may be due to a difference in purity of the La@C_{82}, which significantly influences the spectrum.

In order to understand the EPR spectra observed in Figure 5.4A, the EPR spectrum of La@C_{82} was simulated using the MATLAB Easyspin software [193]. Since exchange interactions are strongly dependent upon wave function overlap, exchange coupling will most likely only occur in clusters of MFs within the C_{60} crystal. Isolated MFs, surrounded by empty caged C_{60} should show the hyperfine interaction between the nuclear (La or Sc) and electron spin of the MF. The ratio of clustered MFs to isolated MFs should increase with concentration of MF species within a C_{60} crystal. With increasing concentration of MFs it is expected that the dipole-dipole interaction should increase due to a decrease in the average inter-MF separation, leading to broadening of the EPR signal, as shown in the pure case.

5.2.2.1 Simulating the spin

Simulation of the metallofullerene spin system assumed that any exchange coupling between MF clusters is a constant J, since the largest J value arises from MF nearest

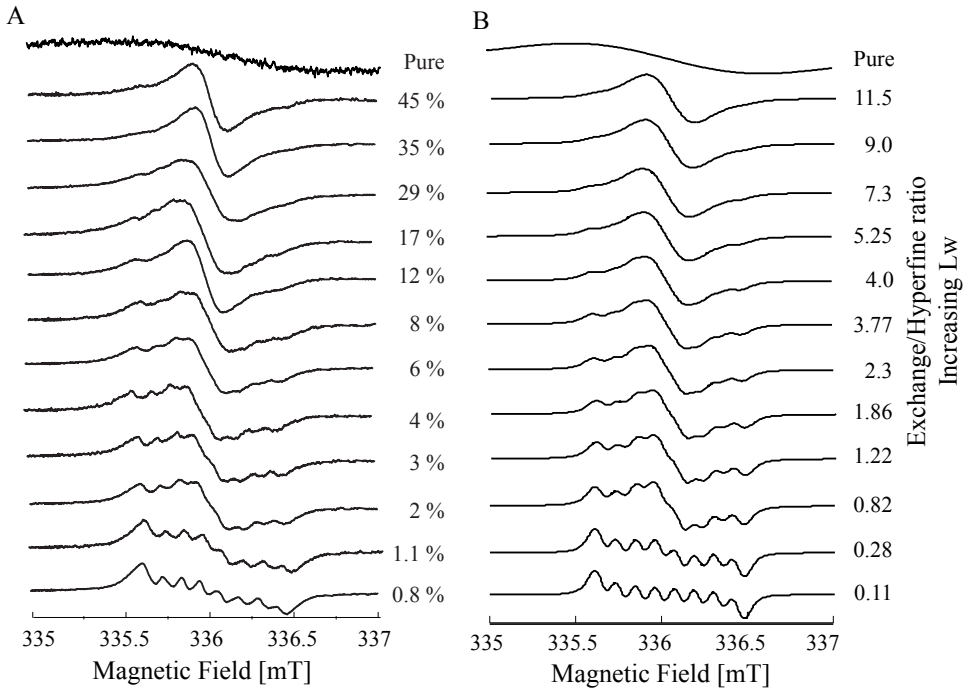


Figure 5.4: (A) CW EPR of La@C_{82} with varying molar concentration in C_{60} crystals (B) Simulation of La@C_{82} with increasing exchange/hyperfine ratio and increasing linewidth. Experimental parameters: Field modulation 100 kHz, 1 G; Microwave power 1.976 mW; Temperature 300 K.

neighbours, therefore smaller couplings can be ignored. To account for the dipole-dipole interactions the linewidth is increased with concentration. Two systems were simulated, a two-spin exchange-coupled system to represent MF clusters and a single spin hyperfine interaction system for isolated MFs. By combining different ratios of the exchange coupled and hyperfine interaction system, the experimental results were successfully reproduced as shown in Figure 5.4B.

The exchange interaction J coupling strength for the MF clusters is set to 13 MHz, and the linewidth for each component is shown in Table 5.1. The ratio of exchange coupled MF clusters and hyperfine interaction was determined to match

$La@C_{82}$			
MF Molar Content (%)	Ratio Exchange/Hyperfine	Hyperfine LW/mT	Exchange LW/mT
Pure	Pure	0.801	1.221
45	11.50	0.105	0.183
35	9.00	0.102	0.178
29	7.33	0.099	0.175
17	5.25	0.093	0.166
12	4.00	0.089	0.160
8	3.17	0.085	0.153
6	2.70	0.082	0.149
4	2.03	0.078	0.143
3	1.50	0.076	0.139
2	1.22	0.072	0.134
1.1	0.28	0.067	0.126
0.8	0.11	0.064	0.122

Table 5.1: Line width parameters used in the simulation relating to produce the simulated spectra in Figure 5.4B for $La@C_{82}$

the experimental results for each concentration.

5.2.3 EPR results $Sc@C_{82}$

Similar experiments were performed on $Sc@C_{82}$, Figure 5.5A, for dilutions between 0.4% and 71% again using the same preparation methods and the same amount of $Sc@C_{82}$ in each case to keep the total number of spins constant. The stronger hyperfine interaction in $Sc@C_{82}$ than $La@C_{82}$ makes it more robust against exchange narrowing and the hyperfine structure is retained up to a concentration of 46% [49].

A similar simulation was used to effectively reproduce the concentration dependence of the $Sc@C_{82}$ EPR spectrum and is presented in Figure 5.5A. The J coupling for the MF clusters is set to 60 MHz, and the linewidth for each component is shown in Table 5.2. The stronger hyperfine of $Sc@C_{82}$ makes it more robust against ex-

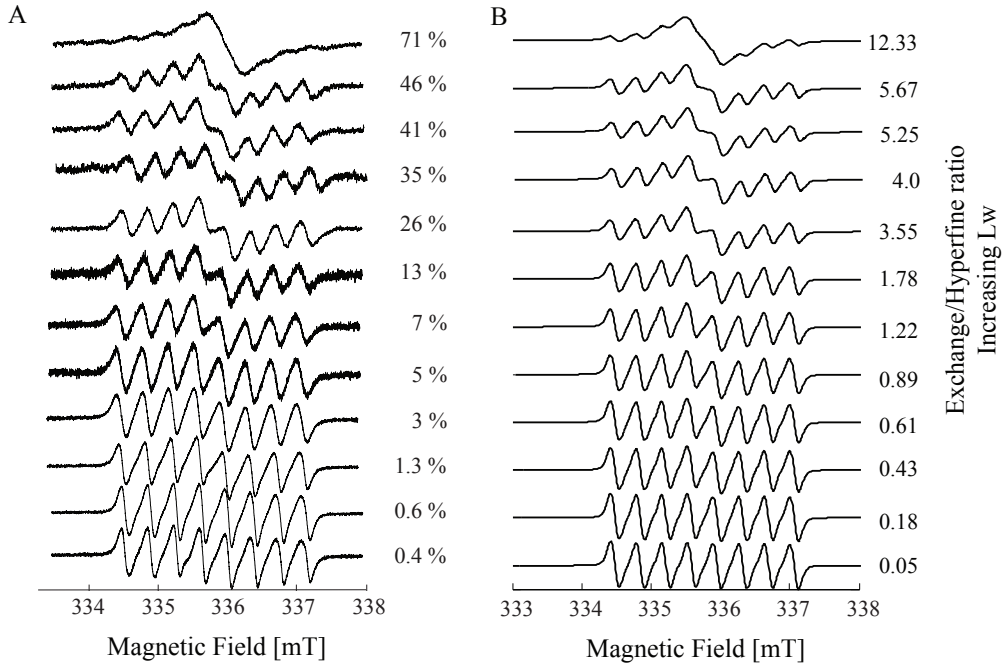


Figure 5.5: (A) CW EPR of $Sc@C_{82}$ with varying molar concentration in C_{60} crystals (B) Simulation of $Sc@C_{82}$ with increasing exchange/hyperfine ratio and increasing linewidth. Experimental parameters: Field modulation 100 kHz, 1 G; Microwave power 1.976 mW; Temperature 300 K.

change narrowing; as demonstrated through the value of exchange coupling used in the simulation in Figure 5.5B compared to that mentioned above for $La@C_{82}$.

5.3 Discussion

The EPR analysis of $La@C_{82}$ and $Sc@C_{82}$ has demonstrated how the environment of the endohedral metallofullerenes can affect the interactions in the system. From the EPR the concentration at which each of the three competing interactions are dominant has been identified. At low concentrations, where the endohedral metallofullerenes will be largely isolated the hyperfine interaction for both $La@C_{82}$ and

$Sc@C_{82}$			
MF Molar Content (%)	Ratio Exchange/Hyperfine	Hyperfine LW/mT	Exchange LW/mT
71	12.33	0.139	0.406
46	5.67	0.136	0.376
41	5.25	0.136	0.368
35	4.00	0.135	0.358
26	3.55	0.133	0.339
13	1.78	0.130	0.299
7	1.22	0.126	0.268
5	0.89	0.125	0.252
3	0.61	0.122	0.230
1.3	0.43	0.118	0.198
0.6	0.18	0.115	0.172
0.4	0.05	0.113	0.160

Table 5.2: Line width parameters used in the simulation relating to produce the simulated spectra in Figure 5.5B for $Sc@C_{82}$

$Sc@C_{82}$ is detected in the EPR spectra. As the concentrations increases, metallofullerenes will begin to come into contact with each other leading to the rise in exchange interaction, therefore leading to narrowing of the EPR spectra. In complete metallofullerene crystals the dipole-dipole interaction become dominant and leads to an overall broadening of the spectra. Simulation of the experimental data may indicate that the metallofullerenes powders may form clusters of metallofullerenes and clusters of empty caged fullerenes. Work by Ito *et al.* [194] investigated the EPR of $La@C_{82}$ systems using different empty cages fullerenes, C_{60}, C_{70}, C_{78}, C_{82} and C_{84}, in the crystal matrix. Their findings indicated that dipole-dipole and exchange interactions could be controlled by concentration but also by controlling the fullerene environment. $La@C_{82}$:C_{82} gave the most ordered structure and as a result the most observable hyperfine structure, while $La@C_{82}$:C_{60}, which had the largest difference in solubility, produced more clusters and showed more exchange

and dipole-dipole interactions in the EPR. This suggests that for metallofullerene 3D crystal structures the concentration and the empty caged fullerene environment are important factors to control the spin interactions.

These results have demonstrated that metallofullerene spin properties can be controlled by diluting spin active metallofullerenes in a 3D crystal matrix of empty caged fullerenes. The dilution of metallofullerenes in 3D crystals offers a route to control the main spin interaction present in the system, hyperfine, exchange and dipole-dipole interactions. The foundations of metallofullerene spin interactions has been established and the next step is to explore how the metallofullerene spin changes from 3-D crystal to a 1D array inside a nanotube.

Chapter 6

Interactions in Peapods

6.1 Introduction to Peapods

The successful utilization of carbon nanomaterials in future electron spin based technologies is highly dependent upon the ability to control their assembly at the nanoscale to form tailored solid-state architectures. Fullerenes can hold single electron spins with long coherence times and therefore have promise as building blocks for electron spin based technologies [6]. Fullerenes can be inserted into the interior of single-walled carbon nanotubes (SWCNTs) to form peapods [111], offering a way to non-covalently produce highly ordered 1D spin chains [124, 183], with possible applications in quantum information and nanoscale spintronics [6, 5]. Understanding the nature of the spin and spin-spin interaction in such systems will be key to their future integration in devices. The spin-spin interactions between metallofullerenes in a 3D crystal matrix of empty caged fullerenes, discussed in Chapter 5, highlighted the regions where the hyperfine, exchange and dipole-dipole interactions dominate. Peapods of spin active endohedral metallofullerenes should produce a highly or-

dered 1D array of spins and may show different spin-spin interactions compared to 3D crystals. EPR investigation of peapods should provide an understanding of the nature of the interactions between spins within the chain, how it compares to 3D crystals and determine the affect of the surrounding nanotube.

Recent studies on the spin dynamics of peapods have shown that charge transfer between N@C_{60} and SWCNTs is minimal and the N@C_{60} retains its spin-state when encapsulated [195]. Unlike the metallofullerenes, the spin in N@C_{60} is confined to the interior of the C_{60} cage and this reduces the possibility for interactions with other molecular systems [196]. A recent report suggested that the interaction of La@C_{82} with SWCNTs prepared using the super-growth method resulted in the loss of the hyperfine structure in the EPR [133]. This was attributed to a charge transfer mechanism between the La@C_{82} and SWCNTs. Further work is needed to shed more light on the possible interactions of metallofullerenes in SWCNTs. A key component to performing EPR studies on peapods is the use of high quality SWCNTs that have a narrow diameter distribution in order to obtain long range 1D packing of the fullerenes and the SWCNTs also need to be free from magnetic impurities that arise from the catalyst particles containing Co, Ni, or Fe. SWCNTs with narrow diameter distribution (1.37 - 1.65 nm) in the ideal range suitable for filling with metallofullerenes can be produced using laser ablation with the non-magnetic catalyst PtRhRe and are ideal for EPR studies of peapods [77].

6.2 Production of Peapods

Laser ablation PtRhRe SWCNTs, purified by the centrifugation, were coated with surfactants in an aqueous solution and would hinder any fullerene encapsulation.

For successful filling the nanotubes needed to be in powder form and surfactants removed. A cleaning processes was developed which involved washing the purified SWCNTs with MeOH, similar to the process described in 4.2.2. The first step was to centrifuge the surfactant SWCNT solution at 5 krpm using microfilters, removing excess water and surfactant and then adding MeOH to begin the washing process. The small solvent molecules, with assistance of sonication, would destabilize the wrapping of the surfactant and the nanotube, resulting in reduced water solubility, thus causing the SWCNTs to aggregate out of the solution. The water-MeOH solution was removed and fresh MeOH was added and the process repeated to ensure that all the water and surfactant was removed, using typically between 4-5 washes. The SWCNT MeOH solution was vacuum filtered using a 0.22 μm pore size Millipore filter yielding buckypaper.

All nanotube powder samples were heated in air at 450 °C for approximately 20 minutes to open up the end of the nanotubes as well as remove any amorphous carbon impurities. Fullerene samples of $Sc@C_{82}$, $La@C_{82}$, $Y@C_{82}$, C_{60} and $Ce@C_{82}$, prepared at various concentrations, were used to produce peapod samples. Fullerenes in a CS_2 solution were dropped onto a SWCNT buckypaper and the solvent was allowed to evaporate. The samples were then sealed in a quartz tube under vacuum and heated at 500 °C for 4 days to allow filling of the nanotubes via a hot vapour filling method.

Filling of SWCNTs by metallofullerenes is dependent upon the relative diameters of the nanotube and the fullerene. Hodak *et al.* [197] calculated the optimum ratio of the nanotube to fullerene diameter and the energy of fullerene encapsulation. The encapsulation of fullerenes proceeds exothermically if the separation between the fullerene and the nanotube wall is around the van der Waals distance,

0.33 nm. Based on these findings, Lu *et al.* [86] performed DFT calculations on (17,0), (14,7) and (19,0) nanotubes with calculated diameters, 1.31, 1.44 and 1.50 nm respectively. Using La@C_{82} the (14,7) and (19,0) nanotubes were filled exothermically while the narrower (17,0) was calculated to be filled endothermically. This suggests that the DGU-SWCNTs, with FWHM diameter distribution 1.37–1.65 nm should all fill exothermically. The separated metallic and semiconducting SWCNTs have a larger FWHM diameter distribution, 1.2–1.6 nm, and therefore some of the nanotubes may be too narrow to allow successful filling under the current conditions. Upon encapsulation the fullerenes are stabilised by van der Waals forces making the peapods thermodynamically stable systems.

To ensure that the spin properties of the metallofullerene are retained during sublimation under thermal conditions, a sample of Y@C_{82} powder was sealed under vacuum in a quartz EPR tube and heated at 450 °C for 24 hours. The thermally treated Y@C_{82} powder was then dispersed in CS_2 and the EPR was measured, as shown in Figure 6.1, with the doublet hyperfine splitting associated with Y (where I=1/2) observed. This indicated that exposing metallofullerenes to the thermal conditions during the peapod process did not damage the spin.

6.3 Analysis of Peapods Structures

6.3.1 PtRhRe laser ablation SWCNT peapods

Aqua regia and DGU purified laser ablation PtRhRe SWCNTs were used to produce peapods of Sc@C_{82} and La@C_{82} metallofullerenes. Investigations primarily using Sc@C_{82} may offer more insight into the nature of spin-spin interaction, as

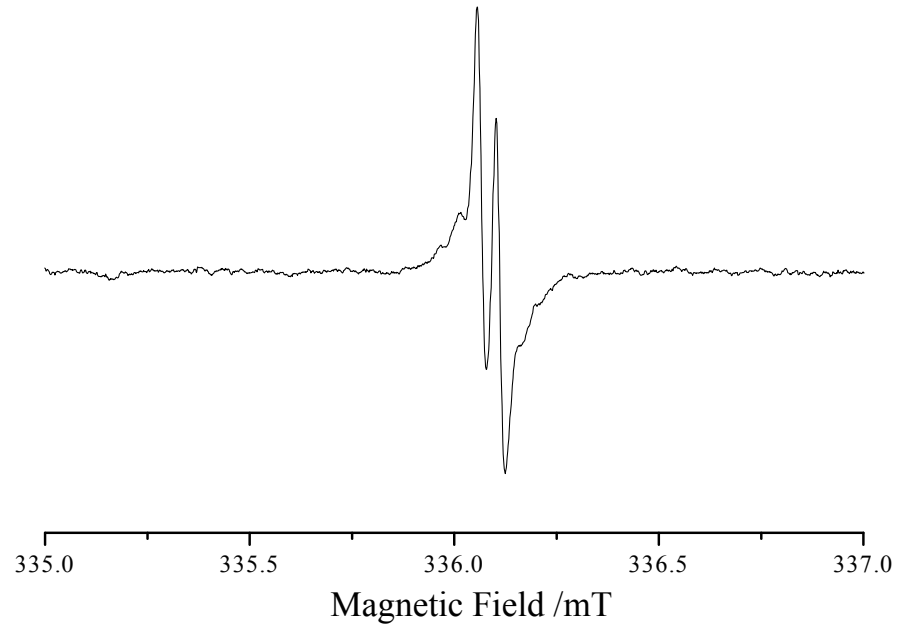


Figure 6.1: EPR of heat treated $Y@C_{82}$ in CS_2 (at 40 dB, Field modulation 100 kHz, 0.1 G, 300K)

the (undisturbed) hyperfine interaction is larger compared to $La@C_{82}$. Peapods of $Sc@C_{82}$ produce a highly ordered 1D array of spins and may show different spin-spin interactions compared to 3D crystals. Visual indication of the filling and purity of $Sc@C_{82}$ peapods was achieved by performing HRTEM. Aqua regia SWCNTs were annealed to remove the high levels of amorphous and graphitic carbon as well as catalyst particles and then filled with a 10% $Sc@C_{82}$:C_{60} solution. HRTEM studies of the 10% $Sc@C_{82}$:C_{60} peapod sample shown in Figure 6.2A indicate a high level of filling of SWCNTs up to approximately 60-80%, with reduced amounts of amorphous carbon and catalyst particles. Figure 6.2B shows a HRTEM image of a typical isolated peapod filled with fullerenes. DGU SWCNTs, which have a reduction in catalyst content, were also filled with $Sc@C_{82}$:C_{60} and filled nanotubes are shown in Figure 6.2C.

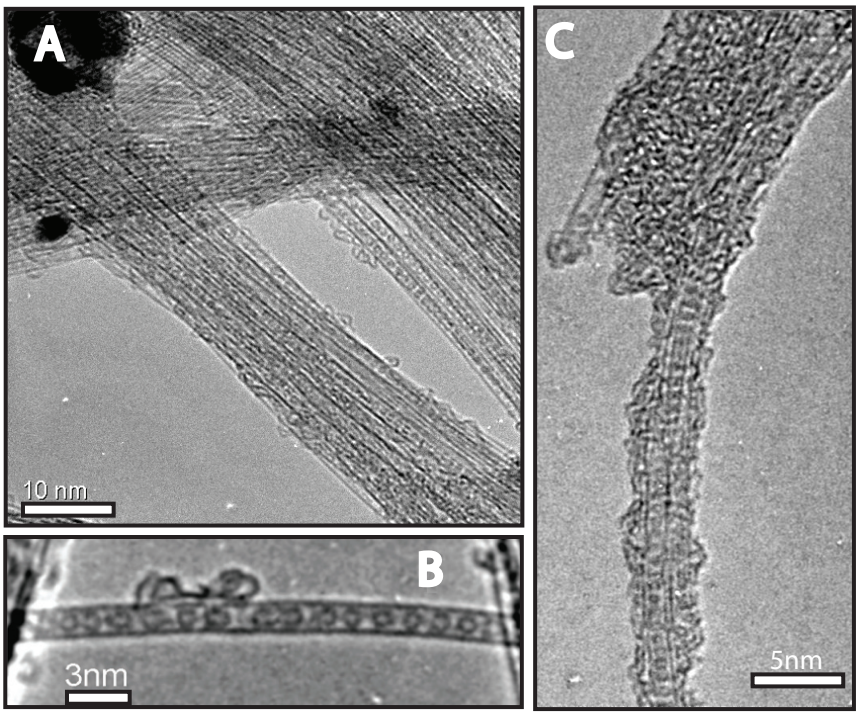


Figure 6.2: (A) HRTEM of aqua regia purified SWCNTs $Sc@C_{82}$:C_{60} peapods (B) HRTEM image of isolated $Sc@C_{82}$:C_{60} aqua regia peapods with higher magnification (C) HRTEM of DGU purified SWCNTs $Sc@C_{82}$:C_{60} peapods

The EPR spectrum of aqua regia purified SWCNTs was measured with the fullerenes first on the outside of the SWCNTs and then filled inside the SWCNTs. These two measurements allow any change in the interactions caused by one dimensional filling to be identified. Peapods were prepared with a molar concentration of 10 % and 0.1% $Sc@C_{82}$. Figure 6.3A shows the CW EPR spectra of the 10% $Sc@C_{82}$:C_{60} sample on the outside of the SWCNTs, with 8 peaks attributed to the hyperfine structure of $Sc@C_{82}$ resolved. The 0.1% $Sc@C_{82}$ sample, Figure 6.3B, shows almost no noticeable structure due to the minimal amount of $Sc@C_{82}$ and the substantial amount of EPR silent C_{60}. Figure 6.3C shows that upon encapsulation of the 10% $Sc@C_{82}$:C_{60} peapods the hyperfine structure disappears. The spectrum

contains a narrow peak with linewidth $\sim$ 1 G and a broader background peak of linewidth 4.5 G.

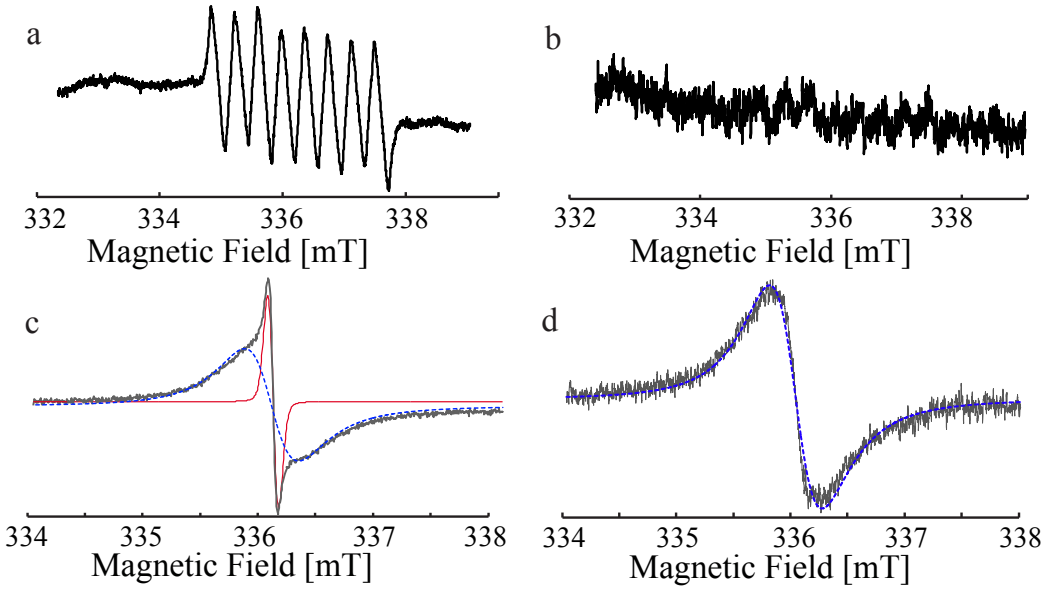


Figure 6.3: (A) CW EPR of 10% $Sc@C_{82}$:C_{60} upon the surface of the SWCNT (B) CW EPR of 0.1% $Sc@C_{82}$:C_{60} upon the surface of the SWCNT (C) CW EPR of 10% $Sc@C_{82}$:C_{60} peapods, including a model of the two components, the narrow and broad peak (D) CW EPR of 0.1% $Sc@C_{82}$:C_{60} peapods, with an overlay of a model of the broad feature. Experimental parameters: Field modulation 100 kHz, 1 G; Microwave power 1.973 mW; Temperature 300K

This broad background peak is also present in the diluted 0.1% $Sc@C_{82}$ peapod sample, shown in Figure 6.3D, suggesting it should not be attributed to the metallofullerenes, but arises instead from some other source such as, amorphous carbon or a catalyst-carbon complex. The narrow 1 G peak has two possible origins, charge transfer between the nanotube and $Sc@C_{82}$ resulting in a spin 1/2 electron or hole on the SWCNT with no measurable Sc hyperfine interaction, or the presence of strong metallofullerene exchange interactions that causes narrowing.

To elucidate which of these two possible mechanisms could be responsible for the

narrow peak further dynamics of $Sc@C_{82}$:C_{60} peapods were studied. Temperature dependence of CW EPR was examined between 5 K and 298 K and is presented in Figure 6.4A. The spectra have been normalised, as the intensity of the peaks increased at lower temperatures. Figure 6.4A shows that at as the temperature decreases the broad component dominates and below 50 K the narrow peak could not be resolved. The broad and narrow peaks were fitted, as shown in Figure 6.3C, and the intensity of the two features has been plotted as a function of temperature and recorded in Figure 6.4B. For temperatures lower than 50 K it was difficult to resolve and fit the narrow peak, therefore values were extrapolated. The inability to resolve the narrow peak associated with the metallofullerenes makes it difficult to extract valuable information from the temperature dependent study in Figure 6.4A and B.

Using pulsed EPR, field dependent Hahn echo (t = 240 ns) measurements from the 10% $Sc@C_{82}$:C_{60} peapod were conducted and only a contribution from the broad background signal was observed. The narrow peak showed no contribution to the Hahn echo, indicating it is being narrowed through spin-spin exchange coupling or spin delocalization (such that $T_2 = T_2^{\star}$). ESEEM measurements also showed no signs of coupling to Sc nuclear spins. The inability to probe the EPR signal attributed to the metallofullerenes in SWCNT peapods using pulsed EPR techniques prompted an alternative approach for determining the underlying nature of the spin signal.

The strong background signal from aqua regia SWCNTs has limited the potential to further investigate the observed narrow peak at low temperatures. Aqua regia purification yielded high quality SWCNTs, however, as demonstrated by HRTEM still contained some residual catalyst particles resulting in an observed EPR signal at 5 K. As previously explained, in Chapter 4.4.4, residual Pt catalyst particles can

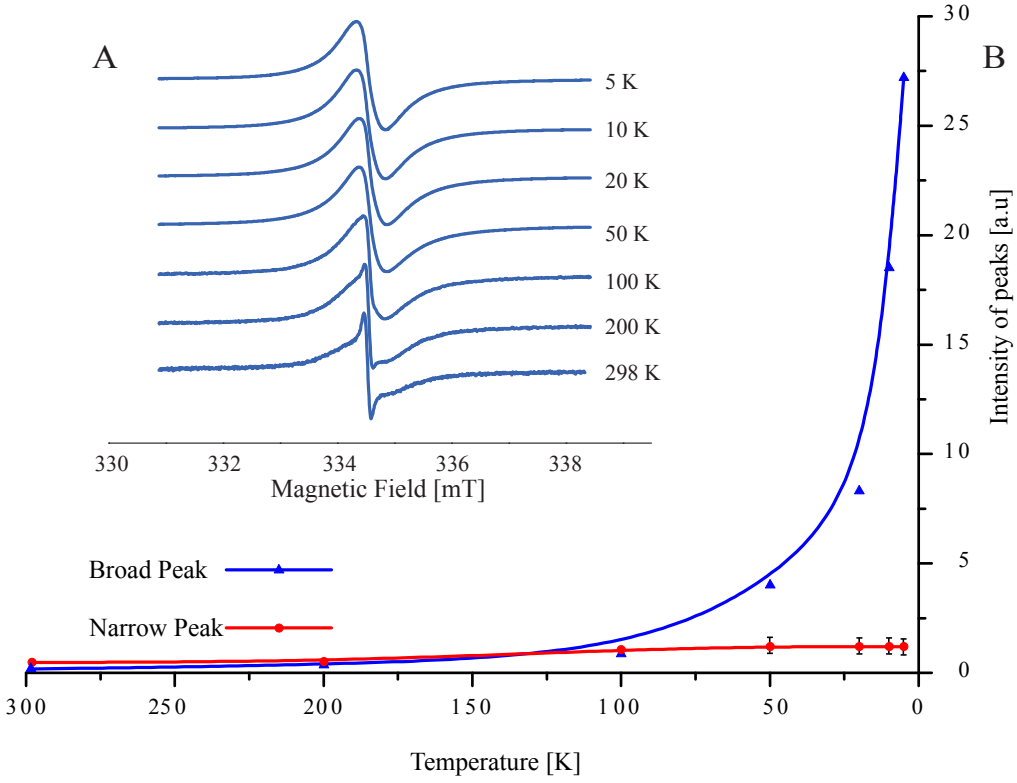


Figure 6.4: (A) Low temperature EPR measurement of 10% $Sc@C_{82}$:C_{60} peapods, indicating the change in intensity of the signal with temperature, where the spectrum has been normalised (B) Intensity of the broad and narrow components, showing the increase in intensity of the broad peak with decreasing temperature.

form complexes with the carbon structure resulting in the observed EPR signal. Ultracentrifugation of SWCNTs has been demonstrated to be an effective purification method to produce high quality catalyst free SWCNTs. The measured EPR at 5 K of the DGU SWCNTs showed no observable signal, making them ideal to study the interesting narrow signal observed in the peapod samples. The purified DGU SWCNTs were annealed to open up the ends of nanotubes before a solution of 10% $Sc@C_{82}$:C_{60} in CS_2 was deposited on the surface, then vacuum sealed and heated to allow thermal filling of the SWCNTs. A controlled DGU SWCNT was also prepared

undergoing the same conditions for peapod production to elucidate any affects upon the SWCNT. Figure 6.5 shows the EPR spectra, at 5 K and 28db, of purified DGU SWCNTs, DGU SWCNT control, 10% $Sc@C_{82}$:C_{60} deposited on the surface of the DGU SWCNTs and 10% $Sc@C_{82}$:C_{60} DGU SWCNT peapods. The EPR spectra indicates that exposing the DGU SWCNTs to the peapod processing conditions results in an observable EPR signal. This observed signal may result from defects being created by the prolonged heat treatment or from other materials entering inside the SWCNT. For aqua regia peapods the observed broad signal was therefore a combination of catalyst effects and thermal degradation to the nanotube structure, and may explain why the intensity of the broad peak dominated the system. By using purified DGU SWCNTs for peapods the EPR from catalyst particles has been reduced but the peapod processing conditions produced an observable EPR signal which can not be controlled.

The 10% $Sc@C_{82}$:C_{60} metallofullerene mixture showed strong hyperfine structure, in the EPR measured at room temperature, when deposited on the surface of the SWCNT. As with the aqua regia 10% $Sc@C_{82}$:C_{60} peapods, the hyperfine structure of $Sc@C_{82}$ is no longer observable upon encapsulation of 10% $Sc@C_{82}$:C_{60}. EPR, at 5K and 28db, of 10% $Sc@C_{82}$:C_{60} DGU peapods, shown in Figure 6.5, shows no sign of the metallofullerene hyperfine structure, instead a two component system, consisting of a narrow $\sim$ 1G and a broad $\sim$ 5G peak, is observed. The combination of broad and narrow peaks was also detected for aqua regia $Sc@C_{82}$ peapods, however, at low temperatures the narrow peak could not be resolved as the intensity of the broad peak dominated. The 5 K EPR spectrum of DGU SWCNT $Sc@C_{82}$:C_{60} peapods was measured as a function of microwave power, between 10 and 40 db, as shown in Figure 6.6A. The change in microwave power could provide more information

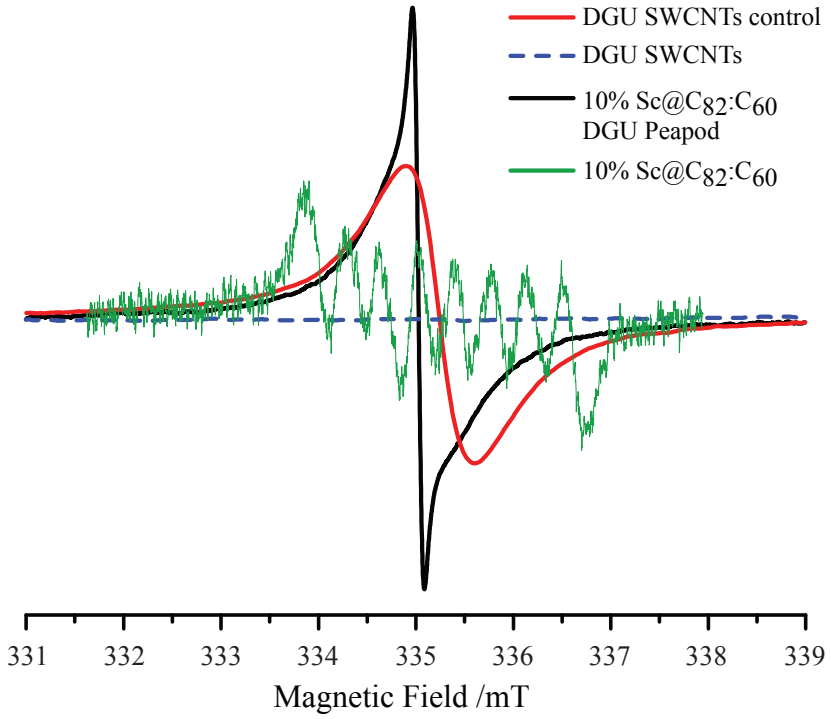


Figure 6.5: Low temperature EPR measurement of purified DGU SWCNTs (blue dotted), DGU SWCNT control (red), and 10% $Sc@C_{82}$:C_{60} peapods (black) performed at 28db. Green line represents the room temperature EPR measurement of 10% $Sc@C_{82}$:C_{60} on the surface of the DGU SWCNTs, performed at 20dB

regarding the nature of the observed signals. For the different microwave powers the EPR spectrum was fitted by combining Lorentzian curves for both the narrow and broad component, as demonstrated in Figure 6.6B for the 28 dB sample. The fits matched well with the experimental data and allowed extraction of quantitative values of the relative intensity of the narrow and broad peak. Figure 6.6C illustrates the change in intensity for both narrow and broad components and the control sample as a function of the root of the microwave power. Unsaturated samples should show a linear increase in susceptibility with the root of the microwave power, as illustrated by the line fits. The broad and narrow components show similar

changes in intensity, saturating at around 0.5 mW, indicating that the spin lifetime of both processes are similar. Although the broad peak has been attributed to the nanotube the power dependence is different to the control sample, which saturates at a higher power, suggesting that upon encapsulation the metallofullerene and nanotube interact, changing the spin environment.

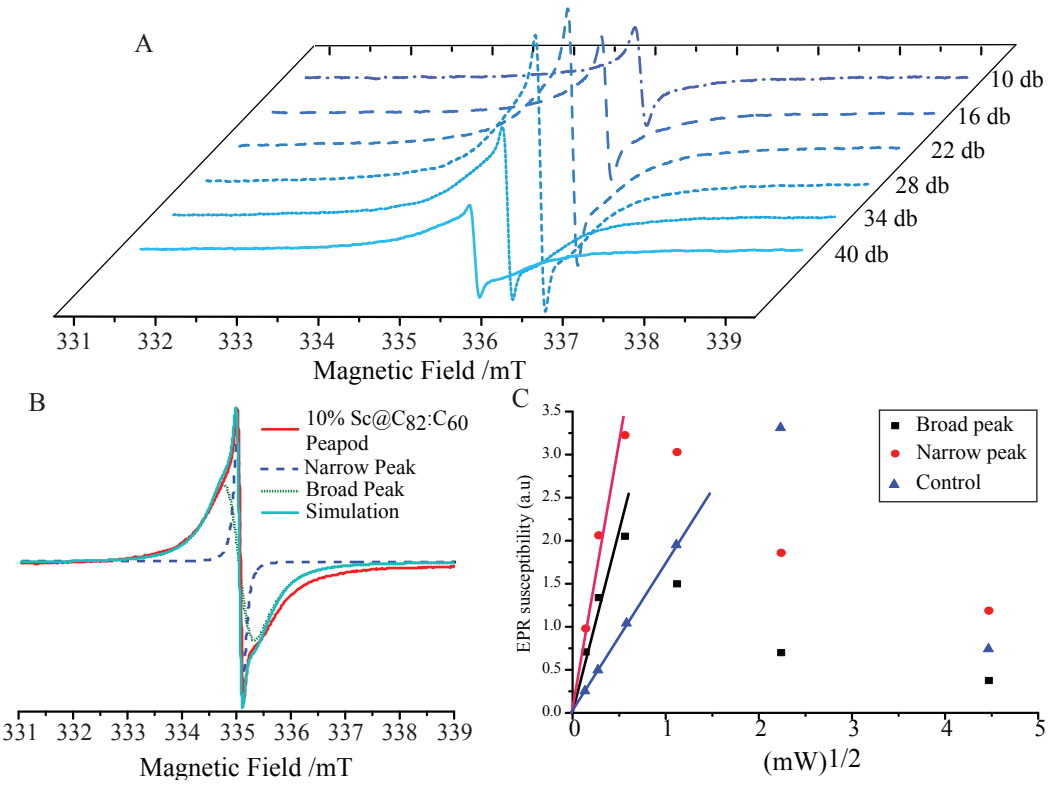


Figure 6.6: (A) Low temperature EPR measurement of DGU 10% Sc@C_{82}:C_{60} peapod with various microwave powers (B) Model to fit the EPR of DGU 10% Sc@C_{82}:C_{60} peapod using a combination of a broad and narrow component (C) Intensity of the broad and narrow components and the control as a function of microwave power, linear relationship shown by line fits.

Peapods of Sc@C_{82} metallofullerene dilutions, prepared with both aqua regia and ultracentrifuged SWCNTs, exhibited a two component EPR signal. Since the observed narrow component originates from the encapsulated metallofullerene, the

overall concentration of the metallofullerene with respect to C_{60} could have an impact on the observed EPR signal. Peapods were prepared with 100% samples of La@C_{82} and Sc@C_{82} metallofullerenes to determine the affects of using pure metallofullerenes in a 1D environment. In 3D crystals pure metallofullerenes samples showed strong dipole-dipole interactions, resulting in the broadening of the EPR signal. Figure 6.7 illustrates the observed EPR signal, at 5 K and 28 db, for 100% La@C_{82} and Sc@C_{82} peapods, 14% Sc@C_{82}:C_{60} peapod and a control DGU SWCNT sample. Each figure includes an inset showing the room temperature EPR of the metallofullerene solution deposited on the SWCNT surface before peapods are formed.

For both the 100% La@C_{82} and Sc@C_{82} samples on the outside of the SWCNT a broaden peak was observed, originating from the dominant dipole-dipole interactions. Upon encapsulation inside the SWCNT the broaden peak was no longer detected and again a two component peak was observed for these peapods. The observed peaks have been successfully simulated to extract the individual broad and narrow components, using the control as a measure to model the broad peak. In both cases the intensity of the narrow peak is weaker, relative to the broad peak, when compared with the 10% Sc@C_{82}:C_{60} peapod sample, shown in Figure 6.5, where the narrow peak was almost twice as strong as the broad at 28 dB. The observed ratio of broad and narrow components may occur due to variation between the samples, as a similar 14% Sc@C_{82}:C_{60} peapod was also prepared with the pure samples and the observed EPR show similar two component peak, with the broad peak dominating.

The preparation of peapod samples was conducted to a high standard, ensuring a uniform production procedure, however, the nature of the multi-step process could result in some variation between SWCNT samples and peapods. These inherent

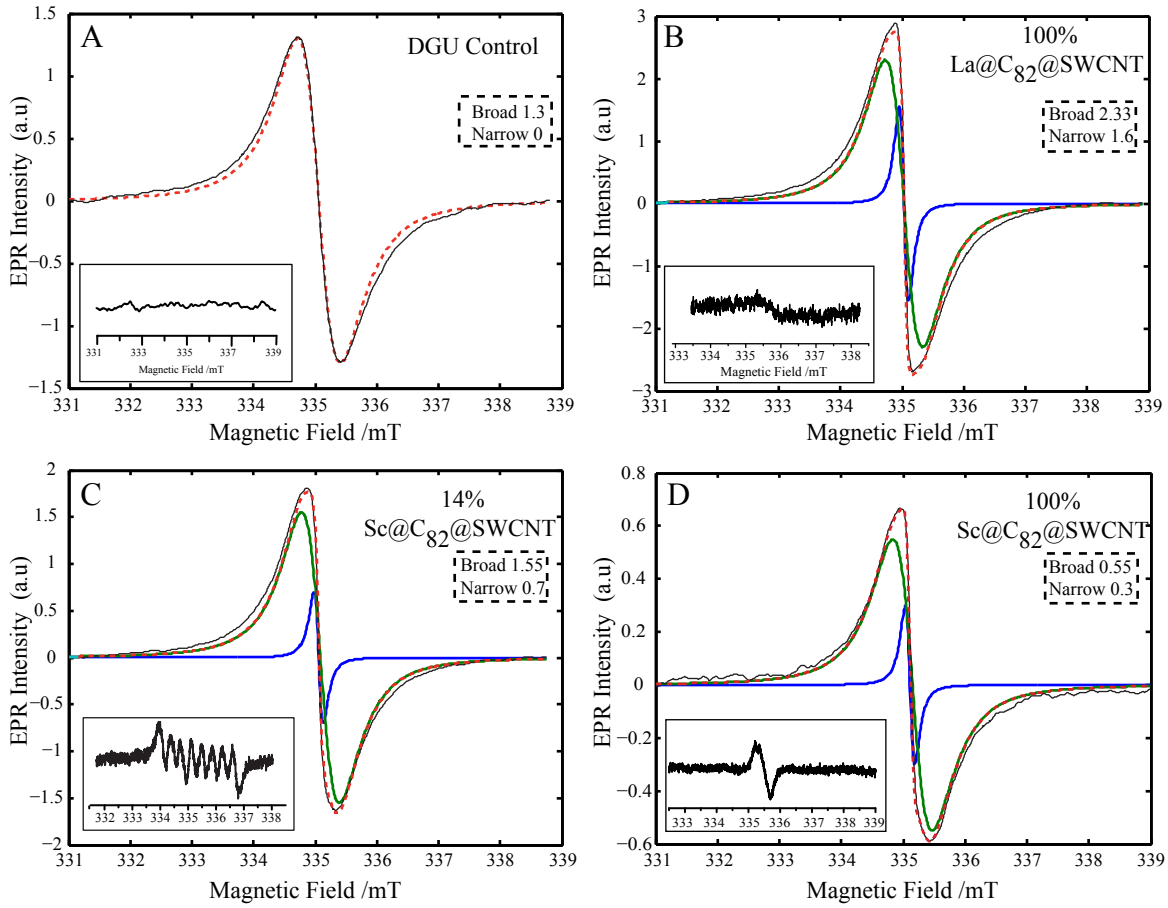


Figure 6.7: EPR spectra (black), at 5 K and 28 db, of (A) DGU control (B) 100% La@C_{82}@DGU-SWCNT (C) 14% Sc@C_{82}@DGU-SWCNT (D) 100% Sc@C_{82}@DGU-SWCNT. EPR spectra have been fitted (red dotted line) by combining two Lorentzian curves corresponding to the broad (green) and narrow (blue) features. The magnitude of the respective broad and narrow components are noted in each figure inside the dashed box. Each figure includes an inset which shows the room temperature EPR, at 20 db, of the samples before undergoing thermal vapour phase filling.

variations may affect the purity of DGU SWCNTs, in terms of residual catalyst particles and surfactant molecules, and the overall filling yield. These factors could explain the observed EPR signals. HRTEM images of both pure La@C_{82} and Sc@C_{82} samples, shown in Figures 6.8 and 6.9, were used to analyse any variations in the

samples. Figure 6.8, contains a series of HRTEM images of pure La@C_{82}@DGU-SWCNT, showing a relatively low filling ratio compared to HRTEM of peapod samples which exhibit strong EPR signals. HRTEM images A and B show bundles of SWCNTs with very few filled with metallofullerenes, highlighted in red and image C shows the periodicity of an 1D array of metallofullerenes in an isolated nanotube. A possible reason for the low filling yield is the presence of foreign solvent molecules, as shown in image D, located on the surface and possibly inside of the nanotube that hinder the encapsulation of any metallofullerenes. HRTEM images of pure Sc@C_{82}@DGU-SWCNTs, shown in Figure 6.9, show a high filling ratio but also show increased levels of catalyst particles. HRTEM images A and B show the level of catalyst particles present in the sample, which may explain the increase in the intensity of the broad peak. Low magnification HRTEM images C, D and E show highly filled SWCNTs with Sc@C_{82}.

Pure Sc@C_{82} and La@C_{82} metallofullerene peapods have shown similar behaviour to the diluted 10% Sc@C_{82}:C_{60} peapods with the observed EPR consisting of a combination of a broad peak and a narrow peak. Again the 3D crystal spin behaviour of La@C_{82} and Sc@C_{82} was no longer observed when the metallofullerenes form a 1D array inside the interior of the SWCNT.

Ce@C_{82} metallofullerenes have similar charge transfer properties from the metal atom to the cage, with 3 valence electrons donated to the C_{82} cage, but Ce@C_{82} does not exhibit measurable room temperature EPR signals [198]. The unpaired electron remaining on the Ce atom is in a 4f orbital, with large angular momentum and spin-obit coupling [198]. This results in the broadening of any EPR signal and explains why it is not observed in our measurements. Ce@C_{82} therefore provides a convenient comparison for the spin active Sc@C_{82}. SWCNTs were filled with Ce@C_{82}

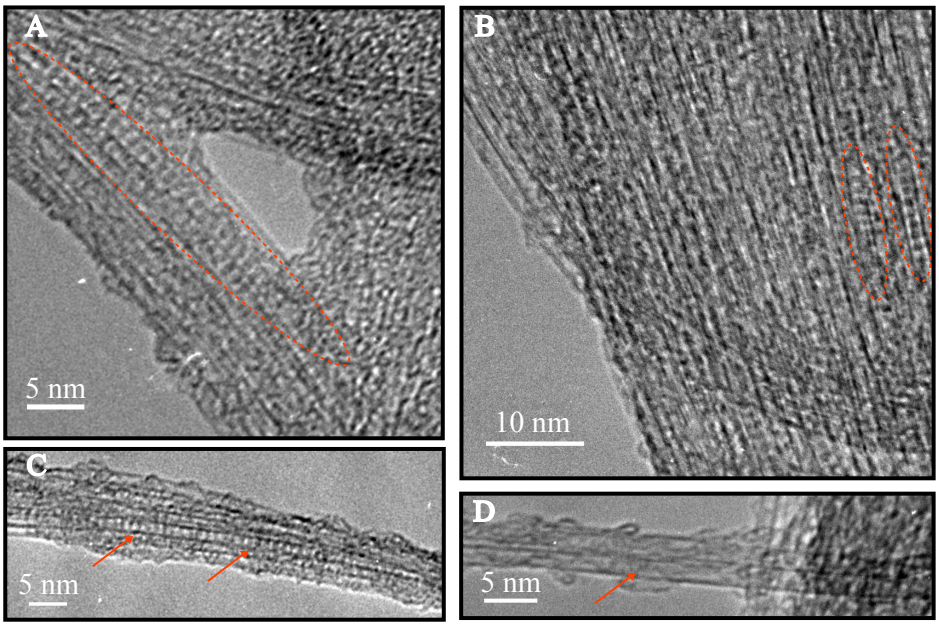


Figure 6.8: HRTEM images of La@C_{82}@DGU-SWCNT. (A/B) Images of large bundles of SWCNTs with few filled, highlighted in red. (C) Nanotube bundles showing periodic packing of metallofullerenes, indicated by arrow (D) Nanotube bundles containing foreign solvent molecules inside or coating the nanotube.

to produce peapods and the room temperature CW EPR spectrum was measured as shown in Figure 6.10. The EPR spectrum of the Ce@C_{82} peapods in Figure 6.10 has been overlaid with the EPR spectrum for Sc@C_{82} aqua regia peapods (blue) and the Sc@C_{82} DGU peapods (red); in all cases a narrow 1 G peak and a broad background peak are present. This provides strong evidence that the narrow peak arises from charge transfer between the SWCNT and MFs and not from exchange narrowing between MFs. This charge transfer results in a delocalized spin on the SWCNT that has no measurable hyperfine interaction with the metal nuclear spin. These results show that when MFs are inserted into SWCNTs the spin dynamics change significantly with strong interactions between the MFs and SWCNT host.

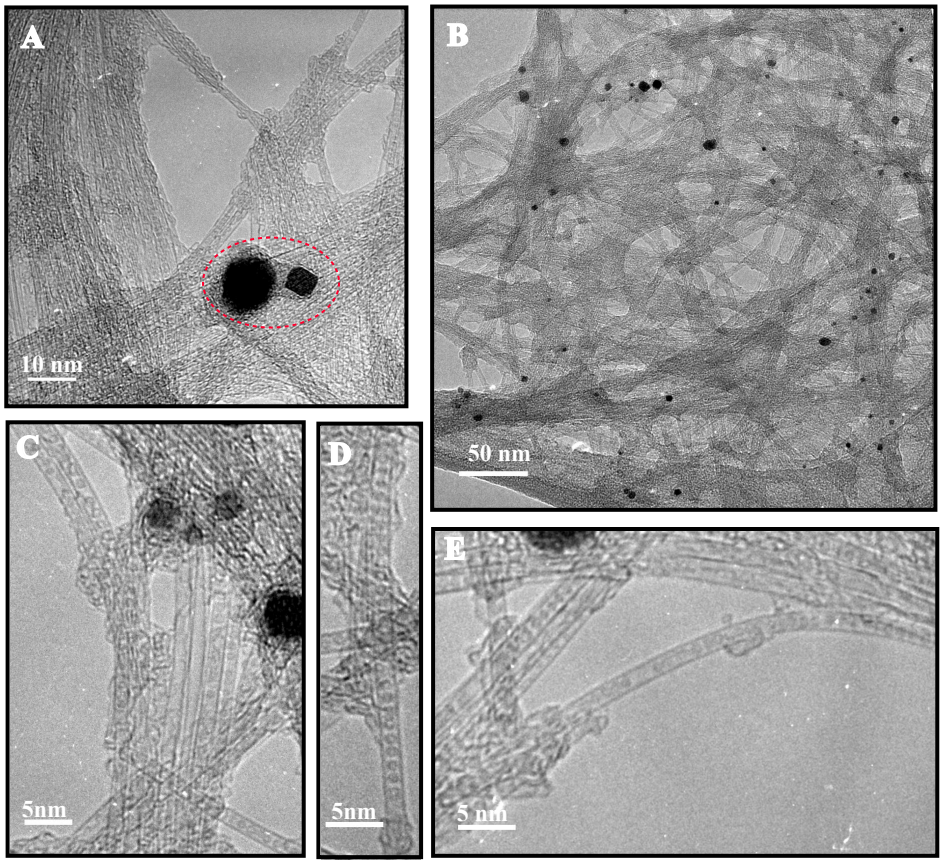


Figure 6.9: HRTEM images of $Sc@C_{82}$@DGU-SWCNT. (A/B) Low magnification images show nanotube bundles containing catalyst particles (C/D/E) High magnification images showing various SWCNT bundles highly filled with $Sc@C_{82}$.

It has been demonstrated that encapsulation of metallofullerene inside SWCNTs, purified by aqua regia treatment or ultracentifugation, resulted in the loss of observable hyperfine structure attributed to charge transfer between metallofullerenes and the host SWCNT. The observed peapod EPR signal can be dissected into two components a broad peak, 5 G, attributed to the nanotube and a narrow peak, 1 G, attributed to the metallofullerene charge transfer. Aqua regia treated SWCNTs have been demonstrated to contain residual catalyst particles and the pristine material

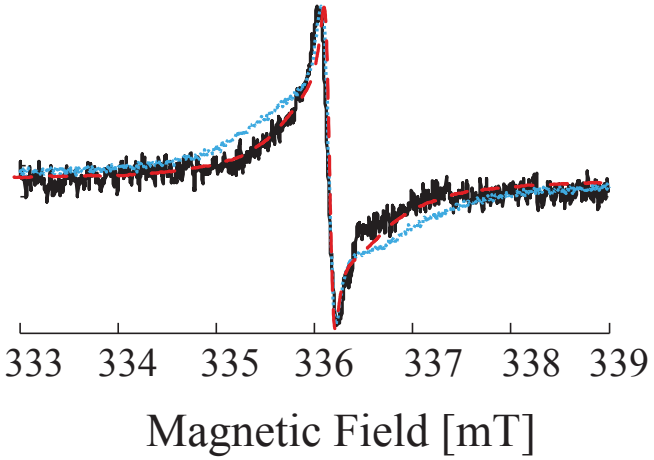


Figure 6.10: CW EPR of $Ce@C_{82}$:C_{60} peapods (black), $Sc@C_{82}$:C_{60} Aqua regia peapods (dotted blue) and $Sc@C_{82}$:C_{60} DGU peapods (dashed red) showing a narrow and broad feature

showed EPR signals at low temperature. As explained in Chapter 4 the origin of the observed EPR signal arises from metal catalyst particles forming complexes with the carbon nanotube. As a result low temperature measurements of aqua regia peapods were dominated by this broad catalyst particle complex signal. Ultracentrifuged SWCNTs have been processed through an alternative purification process, showing reduced amounts of catalyst particles through HRTEM or EPR. DGU SWCNTs exposed to the same thermal conditions, as used for peapod production, produced a broad EPR signal, of 5 G linewidth. The intensity of this broad peak was relatively weak, compared to aqua regia peapods, and allowed both components to be observed at low temperatures. The power dependence of the broad component differed between $Sc@C_{82}$:C_{60} peapod and the control sample, indicating that the nanotube spin environment has been altered by the presence of the metallofullerene. Even with high quality catalyst free SWCNTs an observed EPR signal attributed to the nanotube will be detected as a direct result of the thermal processing employed

to form peapods.

The narrow component has been observed for peapods of Sc@C_{82}, La@C_{82} and Ce@C_{82} metallofullerene samples, both 100% pure and diluted with C_{60}, and has been attributed to the charge transfer between the metallofullerene and the SWCNT. A previous report on La@C_{82} peapods using SWCNTs prepared by super-growth observed similar loss of the hyperfine structure and attributed this to the charge transfer by either n-doping, charge transfer from the fullerene cage to the nanotube, or p-doing, charge transfer from the nanotube to the cage [133]. To elucidate the nature of the charge transfer other experimental and theoretical research on metallofullerene peapods was consulted. Raman spectroscopy of La_2@C_{80}@SWCNT peapods [199] differed from pristine SWCNTs and individual metallofullerene with extra peaks detected between 476-514 cm^{-1} and an up shift of the G band which was attributed to charge transfer from the metallofullerene to the SWCNT. Photoemission experiments on La@C_{82} peapods [200] observe a shift towards the Fermi energy compared to pristine SWCNTs and again was attributed to charge transfer of the SWCNT to the metallofullerene. Theoretical calculations [201] of both C_{82} and La@C_{82} predicts charge transfer from the nanotube to the fullerene cage. Electron density is predicted to move back onto the La atom leading to an asymmetric distribution of charge transfer due to the off centre position of the La atom. Lu *et al.* [86] performed further theoretical measurements using various nanotube diameters on mono, di and tri metallofullerene species. The controlling factor for metallofullerene peapods was determined to be the electron affinity of the metallofullerene, the distance between the nanotube and the metallofullerene and the strain on the nanotube. For La@C_{82} peapods the single occupied molecular orbital of the La@C_{82} overlapped with the valence band of the nanotube, allowing electrons to

transfer from the nanotube to the metallofullerene.

Peapod experiments, which have been discussed, suggest that encapsulation of metallofullerenes results in charge transfer, from the nanotube to the metallofullerene, affecting the properties of both species properties. The observed loss of the metallofullerene hyperfine signal could be explained by the loss of the unpaired spin of the metallofullerene via charge transfer. Electrochemistry experiments on La@C_{82} have been performed [202] and may yield more information regarding the nature of the charge transfer. The first oxidation of La@C_{82} removes the unpaired electron from the HOMO forming La@C_{82}^{+}, which should be EPR silent. The first reduction potential is at a very low energy occurring with relative ease with an electron occupying the HOMO to form a closed shell species La@C_{82}^{-}. Further reductions will result in electrons occupying the C_{82} molecular orbitals, rather than the La atomic orbitals, but are relatively unstable. Vis-near-IR absorption spectra of the different La@C_{82} species [203] has shown that the anion is highly stable compared to the cation. Limited EPR measurements observed no signal from either species suggesting they are diamagnetic. Electrochemistry of Y@C_{82} [204] measured the change in the electropotential, while also measuring the EPR signal. When changing the elctropotential to the first reduction a decrease in the EPR intensity was observed. A complete loss of the EPR signal was not observed since Y@C_{82} cluster may have been non-reactive. These results suggest that the metallofullerene anion, M@C_{82}^{-}, could form with relative ease from charge transfer from the nanotube, resulting in a closed shell system, which should be EPR silent. The observed narrow signal may arise from the resulting unpaired electron on the nanotube, and maybe affected by the diameter distribution of the SWCNTs which has been calculated to effect the amount of electrons transferred [86].

6.3.2 Metallic and Semiconducting SWCNT Peapods

Aqua regia and DGU purified laser ablation PtRhRe SWCNTs contain a mixture of semiconducting and metallic SWCNTs. The presence of both electronic species may hinder the detection of the metallofullerene hyperfine structure. Metallic SWCNTs could potentially interact with the metallofullerene spin resulting in the loss of observable hyperfine structure. Semiconducting SWCNTs should provide an ideal environment, where the nanotube should have minimal interactions with the metallofullerene system. Comparing peapods using separated semiconducting and metallic SWCNTs should provide an idea of how the electronic nature of the SWCNT affects the properties of 1D metallofullerene arrays.

The metallic and semiconducting SWCNTs, purchased from Nanointegris, are 95% pure and grown by arc-discharge. The diameter distribution of these separated SWCNTs has been determined from the UV-Vis spectra, shown in Figure 4.8, indicating that the FWHM diameter distribution of semiconducting and metallic SWCNTs are 1.21 - 1.57 nm and 1.22 - 1.60 nm and have mean diameters 1.38 nm and 1.40 nm respectively. The separated SWCNTs have narrower diameter compared to the DGU-SWCNTs FWHM diameter distribution, 1.37 - 1.65 nm, and mean diameter 1.45 nm. This may result in some of the nanotubes being too narrow to be exothermically filled and may result in a lower filling ratio. The separated SWCNTs have been through several centrifugation steps, producing catalyst free SWCNTs which showed no observable EPR at low temperature, as demonstrated in Chapter 4 Figure 4.18.

Processing the DGU-SWCNT control to thermal conditions for peapod production resulted in the appearance of a EPR signal with a 5 G linewidth. The observed

signal was a direct result of the thermal treatment that may cause defects to be created or some radical groups to form. To further understand the effect of the thermal process on the nanotube, Raman spectroscopy was performed to monitor the level of the D/G ratio of raw, annealed and controlled semiconducting SWCNTs. Figure 6.11 illustrates the Raman spectroscopy performed for the semiconducting samples between 1200 and 1800 cm^{-1}, indicating both the D peak, at ~1330 cm^{-1}, and the G peak at ~1570 cm^{-1}.

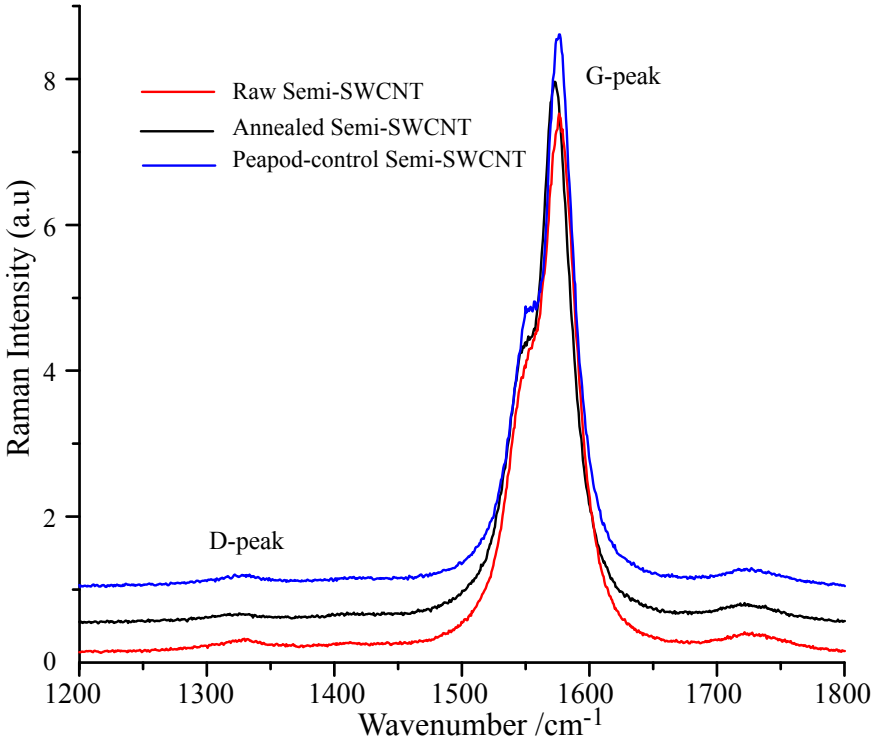


Figure 6.11: Raman spectroscopy of raw, annealed and peapod control semiconducting samples, used to compare the D peak (~1330 cm^{-1}) and the G peak (~1570 cm^{-1}) to determine the relative level of defects in the samples.

Analysis of the area of the D and G peaks for the semiconducting samples is listed in Table 6.1. Comparing the ratio of the D/G peaks gave very similar values

for all the semiconducting SWCNT samples. The peapod control has a minimal increase in the D/G ratio, likely to be a result of the prolonged thermal treatment. However a D/G ratio in this region is indicative of high quality SWCNTs [155, 175]. The observed EPR signals for the semiconducting control, shown in Figure 6.15, is likely to be a direct result of the thermal damage or filling with other molecules during peapod processing and therefore will be observed for any nanotube sample undergoing hot thermal vapour filling.

Semiconducting SWCNT	D peak @ ∼1330 cm^{-1}	G Peak @ ∼1570 cm^{-1}	D/G ratio Ratio
Raw	2.35	40.55	0.0581
Annealed	2.21	38.15	0.0578
Control	2.30	37.82	0.0609

Table 6.1: Analysis of the area of the D peak (∼1330 cm^{-1}) and the G peak (∼1570 cm^{-1}) from the Raman spectroscopy for the semiconducting samples

Peapods of metallic and semiconducting SWCNTs were prepared using 100% metallofullerenes and dilutions of metallofullerenes in C_{60}. Pure and diluted samples have been studied to determine if there any concentration affects on the EPR signal. In addition to Sc@C_{82} and La@C_{82}, a sample of Y@C_{82} was used since it was highly concentrated and should encourage maximum filling inside the SWCNTs, which may enhance detection of metallofullerene spins. For both the semiconducting and metallic samples similar amounts of SWCNTs, approximately 0.1 mg, were used to ensure consistency between samples. Semiconducting and metallic SWCNTs were filled with 100% Sc@C_{82}, 15% Sc@C_{82}:C_{60}, 100% La@C_{82}, 5% La@C_{82}:C_{60} and 100% Y@C_{82}, following the same vacuum thermal processing as detailed for DGU SWCNTs.

To determine the success of the filling process HRTEM visually evaluated the

samples to analyse the level of filling. HRTEM images of semiconducting 100% $Sc@C_{82}$, $La@C_{82}$ and $Y@C_{82}$ peapods are shown in Figure 6.12 and metallic 100% $Sc@C_{82}$, $La@C_{82}$ and $Y@C_{82}$ peapods are shown in Figures 6.13 and 6.14. Low magnification images of semiconducting and metallic nanotubes, shown in Figures 6.12E and 6.14A respectively, show minimal catalyst particle content.

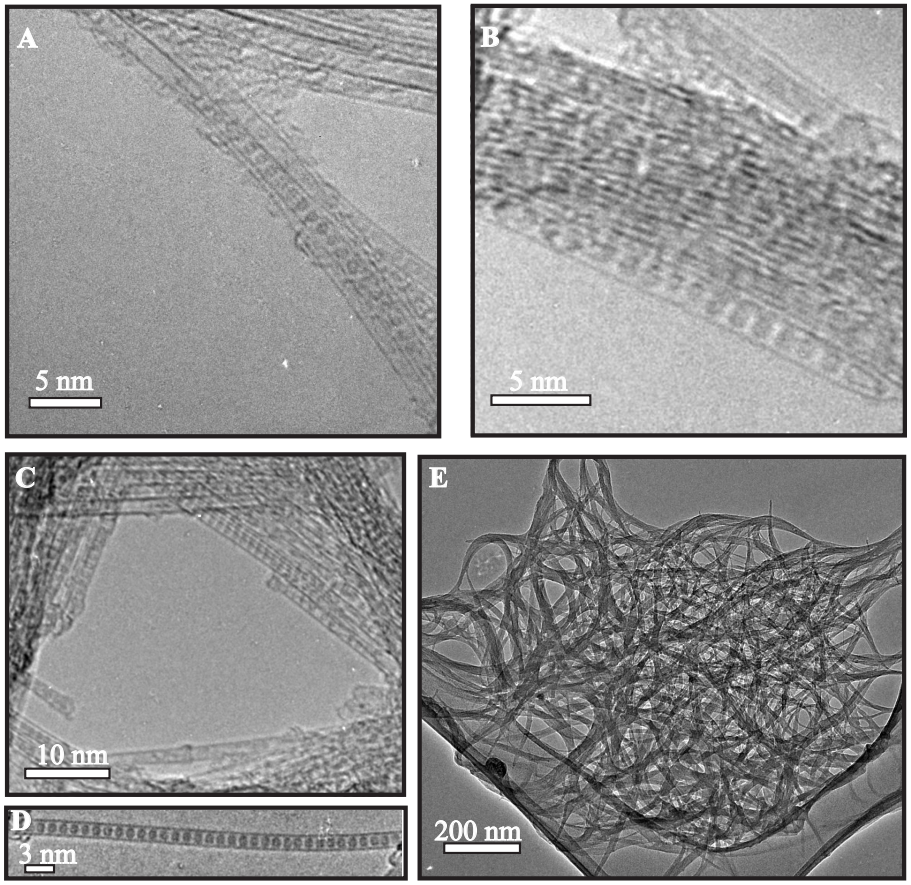


Figure 6.12: HRTEM images of (A) 100% $Sc@C_{82}$ semiconducting SWCNT peapod and (B)100% $La@C_{82}$ semiconducting SWCNT peapod showing an ordered array of metallofullerenes inside the SWCNT (C) and (D) Isolated $Y@C_{82}$ peapod showing well ordered 1D array of metallofullerenes (E) Low magnification image of $Y@C_{82}$ semiconducting SWCNT peapods shown bundles of nanotubes which no visible catalyst particles

All the HRTEM images demonstrate that the SWCNTs are filled with 1-D ordered arrays of metallofullerenes, showing high levels of filling, around $\sim$ 50% for most samples. Fast Fourier transform (FFT) analysis of the highly filled peapods should reveal the average inter-fullerene La@C_{82} spacing.

Figure 6.13E shows the FFT taken of the selected area (highlighted in red) in the HRTEM image in Figure 6.13C. The observed lines, i and ii, correspond to the regular packing of La@C_{82} in metallic SWCNTs. A line profile, the highlighted green box, of the FFT was taken and Figure 6.13F plots the FFT intensity as a function of the periodicity. From the plot an average inter-fullerene La@C_{82} distance has been calculated as d = 1.09 nm $\pm$0.02 nm. The calculated inter-fullerene distance is concordant with previous investigation of La@C_{82} and Sc@C_{82} peapods [141].

Low temperature EPR, 5 K, performed at 28 db, of the semiconducting metallofullerene peapods samples, 100% Sc@C_{82}, La@C_{82} and Y@C_{82}, and a control semiconducting SWCNT sample are shown in Figure 6.15. The EPR of the control is very similar to the 100% metallofullerene peapod EPR, both in the linewidth, approximately around 5G, shown in table 6.2, but also in the overall power dependence. The power dependence, shown in Figure 6.15B, was performed at different microwave powers and shows similar saturation behaviour for the control and the Sc@C_{82} Y@C_{82} and La@C_{82} peapod samples. DGU SWCNTs showed a narrow EPR signal, in Figure 6.6, attributed to the presence of metallofullerenes, while semiconducting SWCNTs show no clear observable signal which can be attributed to metallofullerene presence. The reason for this may be due to the large background nanotube signal, which may dominate any observed nanotube signal, low filling ratio, or may be explained by different charge transfer properties between the metallofullerenes and the semiconducting nanotube. Since the Raman spectroscopy

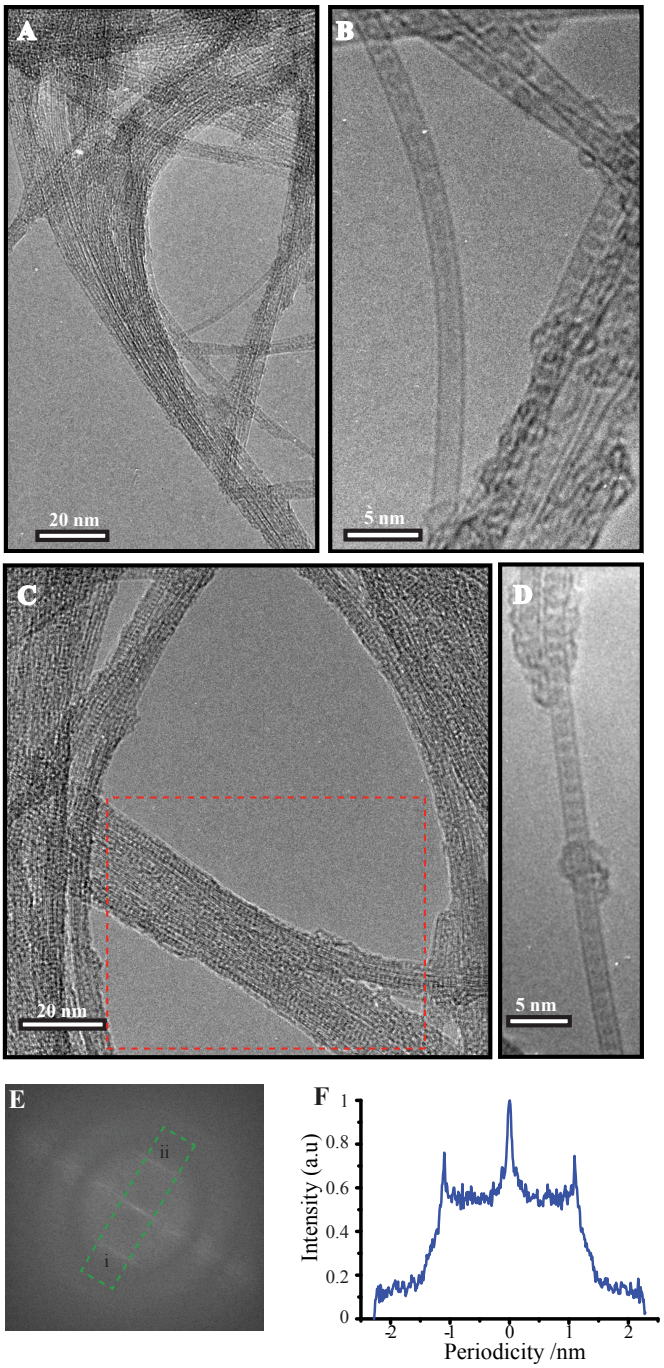


Figure 6.13: HRTEM images showing an ordered array of 100% metallofullerenes inside metallic SWCNT of (A) $Sc@C_{82}$ metallic SWCNT peapod low magnification (B) $Sc@C_{82}$ metallic SWCNT peapod high magnification (C) $La@C_{82}$ metallic SWCNT peapod low magnification, highlighted area in red used for FFT (D) $La@C_{82}$ metallic SWCNT peapod high magnification (E) FFT of HRTEM image C, highlighted area in green used for intensity plot (F) Plot of FFT intensity as a function of periodicity

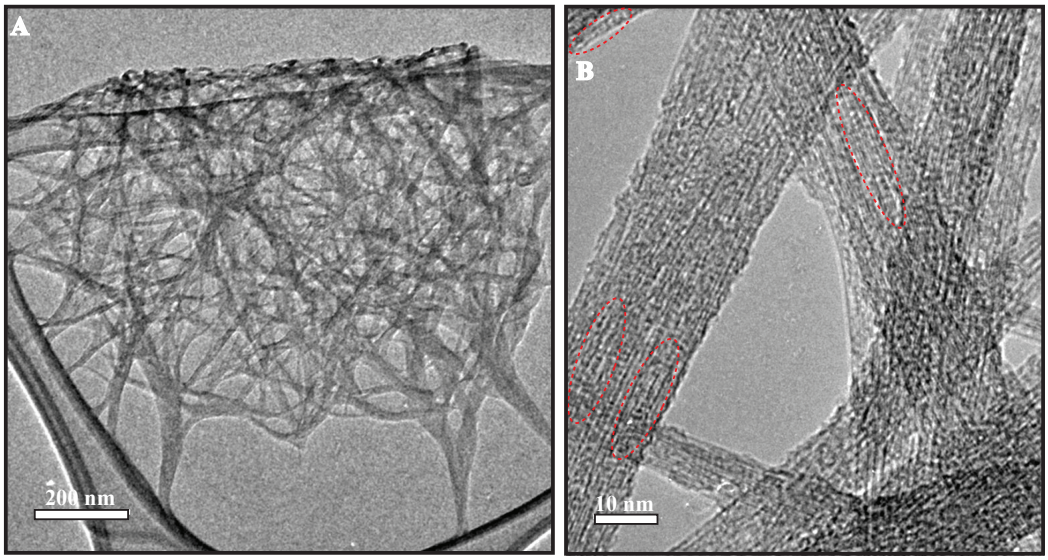


Figure 6.14: HRTEM images showing an ordered array of 100% Y@C_{82} metallofullerenes inside metallic SWCNTs (A) Low magnification image showing nanotube bundles with minimal catalyst particles detected (B) High magnification image of nanotube bundles, peapods are highlighted by red dotted lines.

showed the minimal affect of the processing conditions upon the defect level, the signal observed in the semiconducting peapods may be attributed to the effect of the thermal processing.

Low temperature EPR was performed, at 28db, for the metallic peapod samples, 100% Sc@C_{82}, La@C_{82} and Y@C_{82} and the metallic peapod control is shown in Figure 6.16. Unlike the semiconducting samples the observed EPR indicates a difference between the control sample and the peapod samples. The peapod samples exhibit a narrower linewidth between ∼4–5.5 G, shown in table 6.2, compared to the control linewidth of ∼7.6 G. The metallic peaks have been fitted, shown in Figure 6.17, following the same process that was implemented for DGU-SWCNT peapods. All the observed EPR of metallic peapods was fitted reasonably well by a single Lorentzian curve. DGU-SWCNT metallofullerene peapods resulted in a two

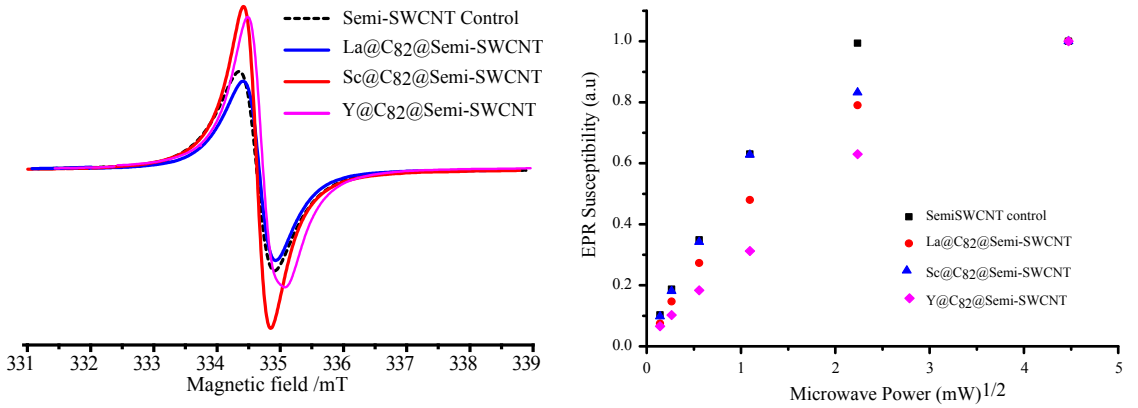


Figure 6.15: (A) EPR spectra, at 5K and 28 dB, of semiconducting SWCNT control, 100% La@C_{82}, 100% Sc@C_{82} and 100% Y@C_{82} semiconducting SWCNT peapods (B) EPR susceptibility measured against increasing power of semiconducting SWCNT control, 100% La@C_{82}, 100% Sc@C_{82} and 100% Y@C_{82} semiconducting SWCNT peapods

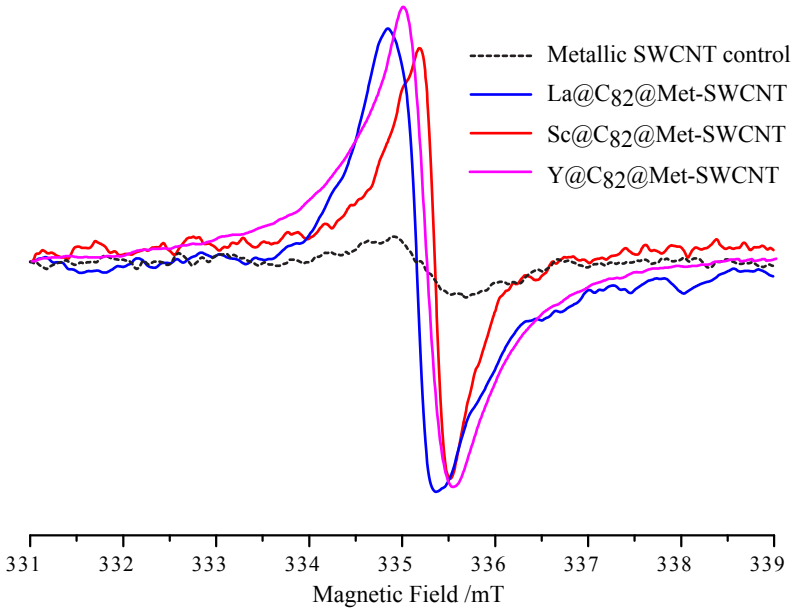


Figure 6.16: EPR spectra, at 5K and 28 dB, of metallic SWCNTs control, 100% La@C_{82}, 100% Sc@C_{82} and 100% Y@C_{82} metallic SWCNT peapods

	Linewidth (G) ±0.1 G	
	Semiconducting	Metallic
Control	5.8	7.6
100% $Sc@C_{82}$	4.5	3.9
15% $Sc@C_{82}$:C_{60}	4.4	4.2
100% $La@C_{82}$	5.3	5.2
5% $La@C_{82}$:C_{60}	6.0	5.9
$Y@C_{82}$	6.0	5.5

Table 6.2: Comparison of the linewidth of 5 K EPR at 28 db for semiconducting and metallic peapods and control

component system, however, this phenomenon was not observed for the metallic peapods and instead only slight narrowing of the linewidth was observed.

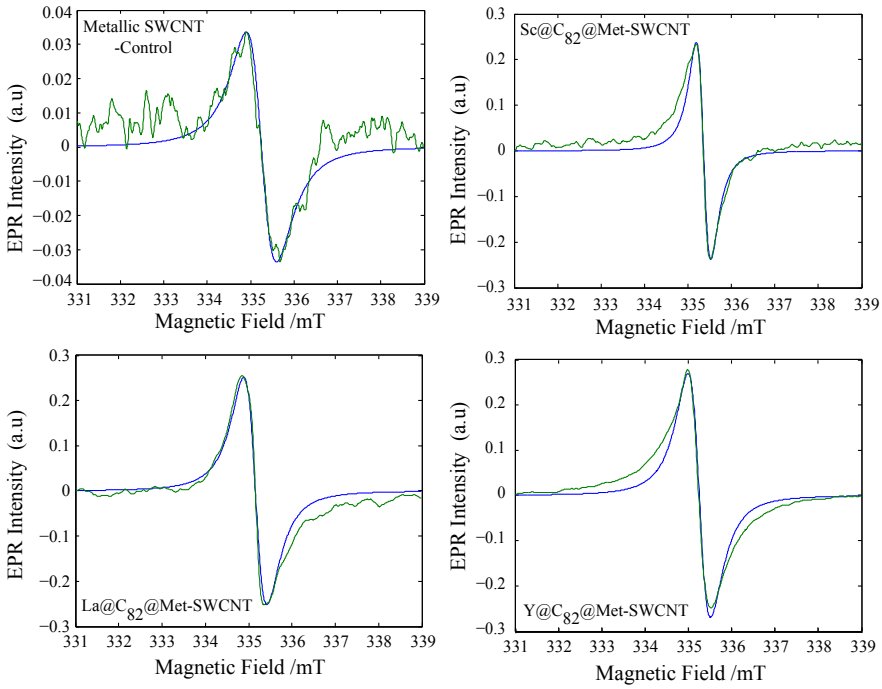


Figure 6.17: EPR spectra (green), at 5K and 28 dB, modelled with single Lorentzian fits (blue) for (A) metallic SWCNTs control (B) 100% $Sc@C_{82}$@Met-SWCNT (C) 100% $La@C_{82}$@Met-SWCNT and (D) 100% $Y@C_{82}$@Met-SWCNT

Semiconducting and metallic peapods were also prepared using dilutions of metallofullerenes, 15% Sc@C_{82}:C_{60} and 5% La@C_{82}:C_{60}. The EPR for semiconducting and metallic diluted peapods is shown in Figures 6.18A and B respectively. Diluted Sc@C_{82} and La@C_{82} metallofullerene peapods, for both semiconducting and metallic SWCNTs, showed only single peaks in the EPR. The observed EPR signals showed similar lineshape and linewidths, indicated in Table 6.2, as observed for the pure metallofullerene peapods. Dilution studies with DGU SWCNTs peapods showed similar results, confirming that the concentration of the metallofullerene sample has a minimal affect on the observed EPR signal.

A possible explanation for the absent metallofullerene spin signal is the spin detection limit, minimum of 10^{13} spins, of the EPR spectrometer. To ascertain whether there was a sufficient number spins present an approximate calculation has been produced for a 0.1 mg peapod sample, shown in Table 6.3. For the calculation a (11,11) SWCNT was chosen as the nanotube diameter, 1.49 nm, should allow exothermic filling and the length of the nanotube was assumed to be 500 nm. Based on this assumption the number of (11,11) SWCNTs in 0.1 mg was calculated. Given an inter fullerene distance of 1.1 nm, as determined from the FFT intensity plot in Figure 6.13, a completely filled SWCNT should contain around 450 fullerenes, and if a 10% M@C_{82}:C_{60} is considered than there will be approximately 45 metallofullerenes spin filled inside a SWCNT. Assuming a SWCNT filling ratio of 10%, there will be approximately 4.5 spins per SWCNT, which results in a total of 1.26×10^{14} metallofullerene spins in 0.1 mg of SWCNTs, which is above the minimum detection limit of the EPR spectrometer. These approximate calculations indicate that there should be sufficient spins to detect any metallofullerene spin signal.

Peapods of semiconducting and metallic SWCNTs were prepared with a variety

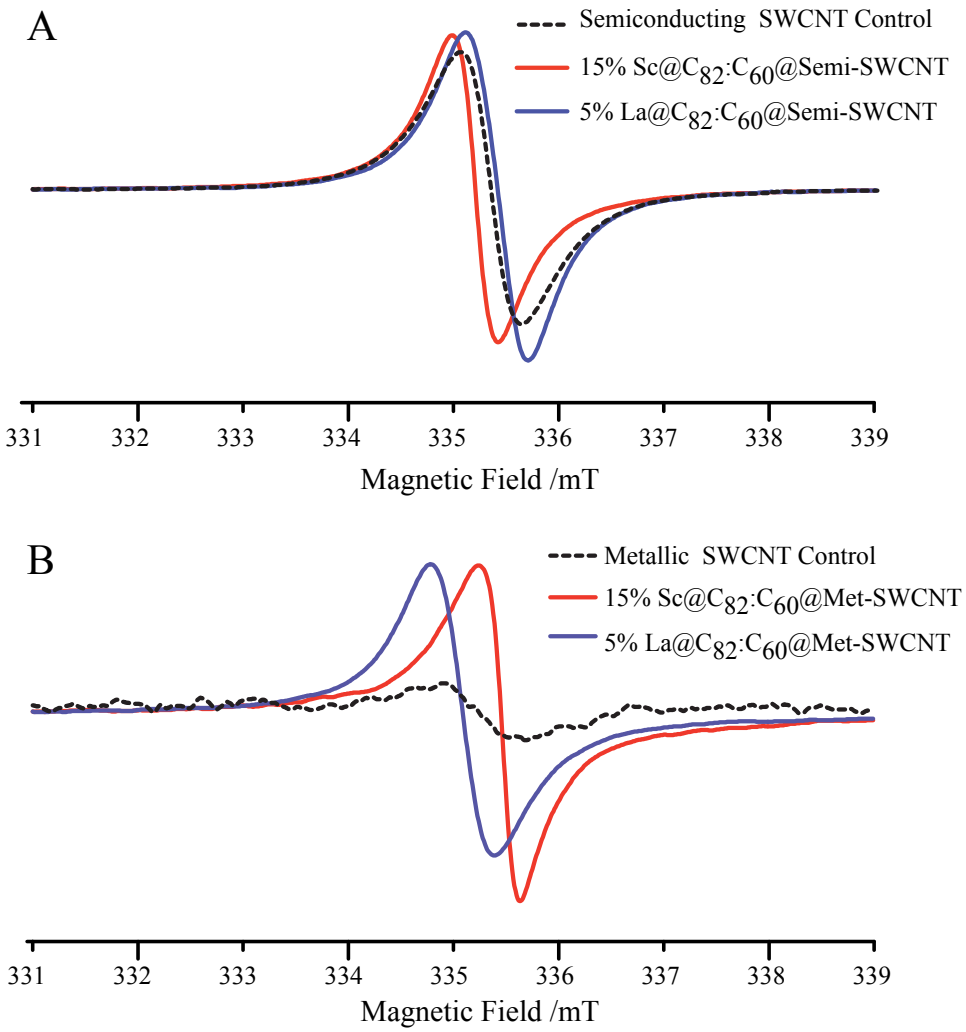


Figure 6.18: (A) EPR spectra, at 5K and 28 dB, of (black dotted) semiconducting SWCNT control, (red) 15% Sc@C_{82}:C_{60}@Semi-SWCNT and (blue) 5% La@C_{82}:C_{60}@Semi-SWCNT (B) EPR spectra, at 5K and 28 dB, of (black dotted) metallic SWCNT control, (red) 15% Sc@C_{82}:C_{60}@Met-SWCNT and (blue) 5% La@C_{82}:C_{60}@Met-SWCNT

Number of carbon atoms in (11,11) 500 nm SWCNT	90,000
Mass of 1 carbon atom /g	1.99×10^{-23}
Mass of a (11,11) 500 nm SWCNT /g	1.78×10^{-18}
Number of (11,11) SWCNTs in 0.1mg	2.79×10^{13}
Number of fullerenes to fill a 500nm SWCNT	450
Concentration of $M@C_{82}$:C_{60} /%	10
Number of metallofullerenes in a 500nm SWCNT	45
Filling Ratio	10%
Total MF spins per SWCNT	4.5
Total number of MF Spins in 0.1 mg of SWCNTs	1.26×10^{14}

Table 6.3: Calculations to determine the total number of metallofullerene spins filled in 0.1mg of SWCNTs

of metallofullerenes. The calculated mean diameter and FWHM diameter distributions of the separated SWCNTs was smaller than observed for DGU-SWCNTs, which may limit the overall filling and affect the nature of the metallofullerene SWCNT spin interactions. HRTEM images showed highly ordered 1D metallofullerene arrays and no catalyst particles for both semiconducting and metallic SWCNTs. As with DGU-SWCNTs, the thermal peapod processing has produced an EPR signal in both samples, which is not related to metallofullerenes. Raman spectroscopy of semiconducting samples showed no major increase in the defect population, suggesting that the signals could originate from spin carrying impurities, which have also been observed in other EPR studies of DGU separated SWCNTs [205]. Metallofullerene hyperfine, exchange or dipole interactions were not observed upon encapsulation inside SWCNTs. Aside from slight narrowing of the EPR signal the peapod showed no difference to the control SWCNT sample. Control samples and peapods from metallic SWCNTs were fitted with single Lorentzian functions confirming the presence of a single signal. Semiconducting SWCNT control and peapods demonstrated similar susceptibility measurements, indicating similar spin

lifetimes.

6.4 Summary

SWCNTs, purified by aqua treatment or ultracentrifugation, and separated semiconducting and metallic SWCNTs were filled with various metallofullerenes, Sc@C_{82}, La@C_{82}, Y@C_{82} and Ce@C_{82} to form peapods. Metallofullerene spin properties observed in 3D crystals have not been maintained when encapsulated inside SWCNTs forming a 1D array. Inserting spin-active metallofullerenes into SWCNTs to form peapods resulted in immeasurable metallofullerene hyperfine structure. For aqua regia and DGU SWCNT peapods the loss of the hyperfine structure has been attributed to charge-transfer interactions between the metallofullerene and the SWCNTs. EPR of Sc@C_{82} and La@C_{82} peapods exhibited a two component system consisting of a broad, $\sim$5 G, and a narrow, $\sim$1 G, component. Nanotube impurities, arising from the thermal peapod production process and catalyst particle impurities, contributed to the broad peak. The narrow peak has been attributed to charge transfer from the nanotube to the metallofullerene. Comparisons with Ce@C_{82} peapods revealed a similar two component system further confirming the charge transfer dynamic.

Using DGU purified SWCNTs, reduced amounts of catalyst particles and minimised the observed EPR nanotube background signal, except those arising from thermal damage. DGU SWCNT control and peapods susceptibility differed in microwave power dependence. Both the narrow and broad peaks in the peapod samples saturated at a lower microwave power compared to the control sample, suggesting different spin lifetimes. Catalyst particle impurities of the SWCNTs sample and the

overall filling ratio of peapods can affect the relative intensities of the broad and narrow peaks. Semiconducting and metallic SWCNTs, grown from arc-discharge using magnetic catalyst particles, contained narrower diameter nanotubes compared to laser ablation PtRhRe SWCNTs. Although HRTEM confirmed filling of ordered metallofullerenes arrays no hyperfine structure could be measured. The EPR spectra of semiconducting and metallic peapods exhibited a single broad peak, similar in line shape and power dependence to the control semiconducting and metallic SWCNTs samples. Separated semiconducting and metallic SWCNT peapods demonstrated different EPR signals to those observed for DGU SWCNT peapods, which showed a two component EPR signal.

These results have detailed information needed for any future advancement of solid-state architectures for spin dependent transport studies and devices using spin active metallofullerenes. The results demonstrate that metallofullerenes can self assemble inside SWCNTs to form 1D arrays of metallofullerenes, however, the peapod systems did not exhibit any hyperfine structure, limiting any control over the metallofullerene spin properties.

Chapter 7

Conclusions

The challenge towards successful application of spin based materials in spintronic devices and quantum information processing has been the development of an architecture that permits controlled assembly at the nanoscale. Metallofullerenes have been demonstrated to form 1-D arrays inside SWCNTs to form peapod structures. In this thesis the electron spin properties of metallofullerenes powders and purified nanotubes have been individually explored to rationalise the nature of the metallofullerene spin upon encapsulation. Various purified SWCNT peapods showed the loss of the metallofullerene hyperfine structure and observed a weak signal, which could be explained by charge transfer from the SWCNT to the metallofullerene. Changing the metallofullerene environment, from a 3D to 1D crystal, significantly affects the nature of the metallofullerene spin.

In Chapter 4, different SWCNT purification processes were investigated with the aim of obtaining high quality catalyst free SWCNTs. Laser ablation PtRhRe catalyst SWCNTs were purified by a multi step process focussed on employing ultracentrifugation, while high vacuum high thermal annealing was performed on CNTs produced by Meijo Carbon. The multi-step centrifugation purification process suc-

cessfully produced highly pure SWCNTs. HRTEM and UV-Vis established the difference between the two samples. The SWCNT sediment, contained substantial amount of catalyst particles and the SWCNT supernatant, contained more isolated SWCNTs with considerable reduction in catalyst particle content and a narrower diameter distribution. EPR of the two contrasting SWCNT samples highlighted a strong correlation between the level of catalyst particles and the detected EPR signal. Purified supernatant and DGU SWCNTs showed no EPR signal at X-band frequencies, whereas the sonicated and sediment SWCNTs, containing higher levels of catalyst particles and both produced an EPR signal. The comparative analysis of the sediment and supernatant SWCNT samples has revealed that metal catalyst carbon complexes were the cause of the strong observable EPR signal. Aqua regia treatment in conjunction with microwave digestion was also employed, however, catalyst particles were observed via HRTEM and resulted in an observed EPR signal. High thermal annealing of Meijo FHP CNTs completely purged magnetic catalyst particles and no EPR signal was observed where as Meijo SO show the presence of magnetic particles in VSM and HRTEM resulting in the detected EPR signal. This research has demonstrated different methods to achieve high quality purified catalyst free SWCNTs.

In Chapter 5, the spin properties $Sc@C_{82}$ and $La@C_{82}$ metallofullerenes were investigated in 3D crystals by dilution in a C_{60} matrix. EPR analysis of $La@C_{82}$ and $Sc@C_{82}$ demonstrated how the environment of the endohedral metallofullerenes can affect the interactions in the system, with three competing interactions identified. At low concentrations, where the endohedral metallofullerenes will be largely isolated the hyperfine interaction for both $La@C_{82}$ and $Sc@C_{82}$ was detected in the

EPR spectra. As the concentrations increases, metallofullerenes will begin to come into contact with each other leading to the rise in exchange interaction, therefore leading to narrowing of the EPR spectra. In complete metallofullerene crystals the dipole-dipole interaction become dominant and leads to an overall broadening of the spectra. Simulation of the experimental data indicated that the metallofullerenes powders may form clusters of metallofullerenes and clusters of empty caged fullerenes. These results have demonstrated that metallofullerene spin properties can be controlled through diluting metallofullerenes in a 3D crystal empty caged fullerene matrix.

In Chapter 6, the spin properties of encapsulated metallofullerenes peapods were investigated to determine the affect of 1-D ordering inside SWCNTs. When metallofullerenes were filled inside laser ablation SWCNTs the metallofullerene hyperfine structure could no longer be observed in EPR. Instead a two component signal, composed of a broad and narrow peak, was detected. The broad peak was accredited to the nanotube, originating from both residual catalyst particles and as a result of the thermal processing. The narrow peak has been attributed to the metallofullerenes present inside the nanotube, and occurs independently of the metallofullerene concentration. The loss of the hyperfine structure has been explained by charge transfer from the nanotube to the metallofullerene, resulting in a closed shell system. For all types of SWCNTs the metallofullerene hyperfine structure was not resolved. DGU SWCNTs, with minimal catalyst particles, allowed both broad and narrow peaks to be resolved at low temperature. For both semiconducting and metallic SWCNTs only a single broad peak could be observed for all metallofullerene peapods.

Overall, the work presented in this thesis highlights the potential of self assembled spin active metallofullerenes for spin based technologies. Spin active metallofullerenes in solid state 3D matrices of empty caged fullerenes are a promising architecture for spin based technologies, offering a high degree of control over the metallofullerene spin properties. Metallofullerene SWCNT peapod systems do not exhibit the EPR characteristics that would deem it as a highly positive route to obtaining 1D spin chains.

List of Publications

I have included a list of my publications in chronological order.

First Author Publications

[1] M. Zaka, Y. Ito, H. Wang, W. Yan, A. Robertson, Y.A. Wu, M.H. Rümmeli, D. Staunton, T. Hashimoto, J.J.L. Morton, A. Ardavan, G.A.D. Briggs, and J. H. Warner; Electron Paramagnetic Resonance Investigation of Purified Catalyst-free Single-Walled Carbon Nanotubes, ACS Nano, 2010, 4 (12), pp 77087716

[2] M. Zaka, J.H. Warner, Y. Ito, J.J.L. Morton, M.H. Rümmeli, T. Pichler, A. Ardavan, H. Shinohara, G.A.D. Briggs; Exchange interactions of spin-active metallofullerenes in solid-state carbon networks, Physical Review B, 2010, 81, 075424

Collaborative Publications

[1] H. Wang, J. Luo, A. Robertson, Y. Ito, W. Yan, V. Lang, M. Zaka, F. Schäffel, M.H. Rümmeli, G.A.D. Briggs,and J.H. Warner; High-performance field effect transistors from solution processed carbon nanotubes, ACS Nano, 2010, 4 (11), pp. 6659-6664

[2] A. Bachmatiuk, F. Börrnert, F. Schäffel, M. Zaka, G.S. Martynkowa, D. Placha, R. Schönfelder, P.M.F.J. Costa, N. Ioannides, J.H. Warner, R. Klingeler, B. Büchner, M.H. Rümmeli, The formation of stacked-cup carbon nanotubes using chemical vapor deposition from ethanol over silica, Carbon, 2010, 48, 3175

[3] Y. Ito, J.H. Warner, R. Brown, M. Zaka, R. Pfeiffer, T. Aono, N. Izumi, H. Okimoto, J.J.L. Morton, A. Ardavan, H. Shinohara, H. Kuzmany, H. Peterlik, G.A.D. Briggs; Controlling intermolecular spin interactions of La@C_{82} in empty fullerene matrices, Physical Chemistry Chemical Physics, 2010, 12 (7), pp. 1618-1623

[4] S. Tetali, M. Zaka, R. Schönfelder, A. Bachmatiuk, F. Börrnert, I. Ibrahim, J.H. Lin, G. Cuniberti, J.H. Warner, B. Büchner, M.H. Rümmeli; Unravelling the mechanisms behind mixed catalysts for the high yield production of single-walled carbon nanotubes, ACS Nano, 2009, 3 (12), pp. 3839-3844

[5] J.H. Warner, Y. Ito, M. Zaka, L. Ge, T. Akachi, H. Okimoto, K. Porfyrakis, A.A.R. Watt, H. Shinohara, G.A.D. Briggs, Rotating fullerene chains in carbon nanopeapods, Nano Letters, 2008 8 (8), pp. 2328-2335

References

[1] M.N. Baibich, J.M. Broto, A. Fert, F.N. Van Dau, F. Petroff, P. Etienne, G. Creuzet, A. Friederich, and J. Chazelas. Giant magnetoresistance of (001) Fe/(001) Cr magnetic superlattices. *Physical Review Letters*, 61(21):2472–2475, 1988. 1

[2] G. Binasch, P. Grünberg, F. Saurenbach, and W. Zinn. Enhanced magnetoresistance in layered magnetic structures with antiferromagnetic interlayer exchange. *Physical Review B*, 39(7):4828–4830, 1989. 1

[3] D.D. Awschalom and M.E. Flatté. Challenges for semiconductor spintronics. *Nature Physics*, 3(3):153–159, 2007. 1

[4] D. Awschalom, D. Loss, and N. Samarth. *Semiconductor spintronics and quantum computation*. Springer Verlag, 2002. 1

[5] I. Zutic, J. Fabian, and S.D. Sarma. Spintronics: Fundamentals and applications. *Arxiv preprint cond-mat/0405528*, 2004. 2, 63, 117

[6] S.C. Benjamin, A. Ardavan, G.A.D. Briggs, D.A. Britz, D. Gunlycke, J. Jefferson, M.A.G. Jones, D.F. Leigh, B.W. Lovett, and A.N. Khlobystov. Towards a

fullerene-based quantum computer. *J. Phys. Cond. Matter*, 18(21):867, 2006. 2, 5, 105, 117

[7] R.M. Brown, Y. Ito, J.H. Warner, A. Ardavan, H. Shinohara, G.A.D. Briggs, and J.J.L. Morton. Electron spin coherence in metallofullerenes: Y, sc, and la@ c_ {82}. *Physical Review B*, 82(3):033410, 2010. 2, 105

[8] J. Lee, H. Kim, S.J. Kahng, G. Kim, Y.W. Son, J. Ihm, H. Kato, ZW Wang, T. Okazaki, H. Shinohara, et al. Bandgap modulation of carbon nanotubes by encapsulated metallofullerenes. *Nature*, 415(6875):1005, 2002. 3, 43, 44

[9] H.W. Kroto, A.W. Allaf, and S.P. Balm. C60: Buckminsterfullerene. *Chemical Reviews*, 91(6):1213–1235, 1991. 5

[10] M. Mikawa, H. Kato, M. Okumura, M. Narazaki, Y. Kanazawa, N. Miwa, and H. Shinohara. Paramagnetic water-soluble metallofullerenes having the highest relaxivity for MRI contrast agents. *Bioconjugate Chem*, 12(4):510–514, 2001. 5

[11] S. Bandow, H. Kitagawa, T. Mitani, H. Inokuchi, Y. Saito, H. Yamaguchi, N. Hayashi, H. Sato, and H. Shinohara. Anaerobic sampling and characterization of lanthanofullerenes: extraction of La@C_{76} and other La@C_{2n}. *J. of Phys. Chem.*, 96(24):9609, 1992. 7

[12] R. Huang, H. Li, W. Lu, and S. Yang. Laser-ablation of C_{60}—La_2O_3 mixture. A new route for trapping metal atoms inside a fullerene cage. *Chem. Phys. Lett.*, 228(1-3):111–116, 1994. 7, 8

[13] T. Hirata, Y. Otomo, and R. Hatakeyama. Production and control of La

plasma and application to fullerene-related material process. *Thin Solid Films*, 407(1-2):32, 2002. 7

[14] R. Kitaura and H. Shinohara. Endohedral Metallofullerenes and Nano-Peapods. *Japanese J. of App. Phys.*, 46(3A):881, 2007. 7, 9

[15] K. Kikuchi, N. Nakahara, T. Wakabayashi, S. Suzuki, H. Shiromaru, Y. Miyake, K. Saito, I. Ikemoto, M. Kainosho, and Y. Achiba. NMR characterization of isomers of C_{78}, C_{82} and C_{84} fullerenes. *Nature*, 357(6374):142–145, 1992. 8

[16] H. Shinohara, H. Yamaguchi, N. Hayashi, H. Sato, M. Ohkohchi, Y. Ando, and Y. Saito. Isolation and spectroscopic properties of scandium fullerenes ($Sc_2@C_{74}$, $Sc_2@C_{82}$, and $Sc_2@C_{84}$). *J. of Phys. Chem.*, 97(17):4259, 1993. 8, 110

[17] J. Xiao, M.R. Savina, G.B. Martin, A.H. Francis, and M.E. Meyerhoff. Efficient HPLC Purification of Endohedral Metallofullerenes on a Porphyrin-Silica Stationary Phase. *J. of the Am. Chem. Soc.*, 116(20):9341, 1994. 8

[18] S. Bandow, H. Shinohara, Y. Saito, M. Ohkohchi, and Y. Ando. High yield synthesis of lanthanofullerenes via lanthanum carbide. *J. of Phys. Chem.*, 97(23):6101, 1993. 8

[19] Y. Lian, Z. Shi, X. Zhou, X. He, and Z. Gu. High-yield preparation of endohedral metallofullerenes by an improved DC arc-discharge method. *Carbon*, 38(15):2117, 2000. 8

[20] R.L. Murry and G.E. Scuseria. Theoretical Evidence for a C_{60} "Window" Mechanism. *Science*, 263(5148):791, 1994. 8

[21] S.W. McElvany. Production of endohedral yttrium-fullerene cations by direct laser vaporization. *J. of Phys. Chem.*, 96(12):4935, 1992. 8

[22] B. Kubler, E. Millon, J.J. Gaumet, and J.F. Muller. Dependence of Endohedral Fullerenes Formation on Laser Ablation Parameters of Carbonaceous Materials. *Fullerenes, Nanotubes and Carbon Nanostructures*, 5(5):839, 1997. 8

[23] Y Achiba and T. Wakabayashi. Stability, structures and a hypothetical growth mechanism of carbon 5/6 network. *Zeitschrift für Physik D*, 26:69, 1993. 9

[24] Z.C. Ying, C. Jin, R.L. Hettich, K. Kadish, R. Ruof, et al. Fullerenes: Recent advances in the chemistry and physics of fullerenes and related materials. *Electro. Soc. Proc.*, page 94, 1994. 9

[25] R. Tellgmann, N. Krawez, SH Lin, I.V. Hertel, and E.E.B. Campbell. Endohedral fullerene production. *Nature*, 382(6590):407, 1996. 10

[26] C. Knapp, K.P. Dinse, B. Pietzak, M. Waiblinger, and A. Weidinger. Fourier transform EPR study of $N@C_{60}$ in solution. *Chem. Phys. Lett.*, 272(5-6):433, 1997. 10

[27] Y. Chai, T. Guo, C. Jin, R.E. Haufler, L.P.F. Chibante, J. Fure, L. Wang, J.M. Alford, and R.E. Smalley. Fullerenes with metals inside. *J. of Phys. Chem.*, 95(20):7564, 1991. 10, 105, 110

[28] M. Takata, B. Umeda, E. Nishibori, M. Sakata, Y. Saitot, M. Ohno, and H. Shinohara. Confirmation by X-ray diffraction of the endohedral nature of the metallofullerene Y@C_{82}. *Nature*, 377(6544):46–49, 1995. 10, 11

[29] L. Soderholm, P. Wurz, K.R. Lykke, D.H. Parker, and F.W. Lytle. An EXAFS study of the metallofullerene Y@C_{82}: is the yttrium inside the cage? *J. of Phys. Chem.*, 96(18):7153, 1992. 10

[30] H. Shinohara, N. Hayashi, H. Sato, Y. Saito, X.D. Wang, T. Hashizume, and T. Sakurai. Direct STM imaging of spherical endohedral Sc_2@C_{84} fullerenes. *J. of Phys. Chem.*, 97(51):13438, 1993. 10

[31] R. Beyers, C.H. Kiang, R.D. Johnson, J.R. Salem, M.S. de Vries, C.S. Yannoni, D.S. Bethune, H.C. Dorn, P. Burbank, K. Harich, et al. Preparation and structure of crystals of the metallofullerene Sc_2@C_{84}. *Nature*, 370(6486):196, 1994. 10

[32] C.S. Yannoni, M. Hoinkis, M.S. de Vries, D.S. Bethune, J.R. Salem, M.S. Crowder, and R.D. Johnson. Scandium Clusters in Fullerene Cages. *Science*, 256(5060):1191, 1992. 10, 16, 110

[33] H.M. Rietveld. A profile refinement method for nuclear and magnetic structures. *J. App. Crystal.*, 2(2):65, 1969. 10

[34] D.M. Collins. Electron density images from imperfect data by iterative entropy maximization. *Nature*, 298:49–51, 1982. 10

[35] K. Laasonen, W. Andreoni, and M. Parrinello. Structural and Electronic Properties of La@C_{82}. *Science*, 258(5090):1916, 1992. 11

[36] M. Takata, E. Nishibori, B. Umeda, M. Sakata, E. Yamamoto, and H. Shinohara. Structure of Endohedral Dimetallofullerene $Sc_2@C_{84}$. *Phys. Rev. Lett.*, 78(17):3330, 1997. 11

[37] E. Nishibori, M. Takata, M. Sakata, M. Inakuma, and H. Shinohara. Determination of the cage structure of $Sc@C_{82}$ by synchrotron powder diffraction. *Chem. Phys. Lett.*, 298(1-3):79, 1998. 11, 13, 105

[38] E. Nishibori, K. Iwata, M. Sakata, M. Takata, H. Tanaka, H. Kato, and H. Shinohara. Anomalous endohedral structure of $Gd@C_{82}$ metallofullerenes. *Phys. Rev. B*, 69(11):113412, 2004. 11

[39] P.W. Fowler, D.E. Manolopoulos, G. Orlandi, and F. Zerbetto. Energetics and isomerization pathways of a lower fullerene: The Stone-Wales map for C_{40}. *J. Chem. Soc.*, 91(10):1421, 1995. 12

[40] M. Hoinkis, C.S. Yannoni, D.S. Bethune, J.R. Salem, R.D. Johnson, M.S. Crowder, and M.S. De Vries. Multiple species of $La@C_{82}$ and $Y@C_{82}$. Mass spectroscopic and solution EPR studies. *Chem. Phys. Lett.*, 198(5):461, 1992. 12, 14

[41] S. Suzuki, S. Kawata, H. Shiromaru, K. Yamauchi, K. Kikuchi, T. Kato, and Y. Achiba. Isomers and carbon-13 hyperfine structures of metal-encapsulated fullerenes $M@C_{82}$ (M= Sc, Y, and La). *J. Phys. Chem.*, 96(18):7159, 1992. 12, 14

[42] K. Kobayashi and S. Nagase. Structures and electronic states of $M@C_{82}$ (M= Sc, Y, La and lanthanides). *Chem. Phys. Lett.*, 282(3-4):325, 1998. 12, 105

[43] K. Kobayashi and S. Nagase. Structures and electronic states of endohedral dimetallofullerenes: $M_2@C_{80}$ (M= Sc, Y, La, Ce, Pr, Eu, Gd, Yb and Lu). *Chem. Phys. Lett.*, 262(3-4):227, 1996. 12, 105

[44] S. Nagase and K. Kobayashi. Metallofullerenes $M@C_{82}$ (M= Sc, Y, and La). A theoretical study of the electronic and structural aspects. *Chem. Phy. Lett.*, (1), 1993. 13

[45] H. Shinohara, H. Sato, M. Ohkohchi, Y. Ando, T. Kodama, T. Shida, T. Kato, and Y. Saito. Encapsulation of a scandium trimer in C_{82}. *Nature*, 357(6373):52–54, 1992. 13, 110

[46] S. Hino, K. Umishita, K. Iwasaki, T. Miyamae, M. Inakuma, and H. Shinohara. Ultraviolet photoelectron spectra of $Sc@C_{82}$. *Chem. Phys. Lett.*, 300(1-2):145, 1999. 13

[47] E. Nishibori, M. Takata, M. Sakata, M. Inakuma, and H. Shinohara. Determination of the cage structure of $Sc@C_{82}$ by synchrotron powder diffraction. *Chemical physics letters*, 298(1-3):79–84, 1998. 13

[48] J. Lu, X. Zhang, X. Zhao, S. Nagase, and K. Kobayashi. Strong metal-cage hybridization in endohedral $La@C_{82}$, $Y@C_{82}$ and $Sc@C_{82}$. *Chemical Physics Letters*, 332(3-4):219–224, 2000. 13

[49] G.W. Morley, B.J. Herbert, S.M. Lee, K. Porfyrakis, T.J.S. Dennis, D. Nguyen-Manh, R. Scipioni, J. van Tol, A.P. Horsfield, A. Ardavan, and G.A.D. Briggs. Hyperfine structure of $Sc@C_{82}$ from ESR and DFT. *Nanotechnology*, 16(11):2469, 2005. 14, 113

[50] R.D. Johnson, M.S. Vries, J. Salem, et al. Electron paramagnetic resonance studies of lanthanum-containing C_{82}. *Nature*, 355:239, 1992. 14, 107, 108

[51] M. Hoinkis, C.S. Yannoni, D.S. Bethune, J.R. Salem, R.D. Johnson, M.S. Crowder, and M.S. De Vries. Multiple species of La@C_{82} and Y@C_{82}. Mass spectroscopic and solution EPR studies. *Chemical physics letters*, 198(5):461–465, 1992. 14

[52] H. Shinohara. Endohedral metallofullerenes. *Reports on Progress in Physics*, 63:843, 2000. 14, 15

[53] K. Yamamoto, H. Funasaka, T. Takahasi, T. Akasaka, T. Suzuki, and Y. Maruyama. Isolation and Characterization of an ESR-Active La@C_{82} Isomer. *J. Phys. Chem.*, 98(49):12831, 1994. 14, 17, 18

[54] K. Kikuchi, Y. Nakao, S. Suzuki, Y. Achiba, T. Suzuki, and Y. Maruyama. Characterization of the Isolated Y@C_{82}. *J. Am. Chem. Soc.*, 116(20):9367, 1994. 16, 107, 110

[55] T. Suzuki, Y. Maruyama, T. Kato, K. Kikuchi, and Y. Achiba. Electrochemical properties of La@C_{82}. *J. of Am. Chem. Soc.*, 115(23):11006, 1993. 16

[56] T. Suzuki, K. Kikuchi, F. Oguri, Y. Nakao, S. Suzuki, Y. Achiba, K. Yamamoto, H. Funasaka, and T. Takahashi. Electrochemical properties of fullerenolanthanides. *Tetrahedron*, 52(14):4973, 1996. 16

[57] Q. Li, F. Wudl, C. Thilgen, R.L. Whetten, and F. Diederich. The unusual electrochemical properties of the higher fullerene, chiral C_{76}. *J. of Am. Chem. Soc.*, 114(10):3994, 1992. 16

[58] P.B. Burbank, J.R. Gibson, H.C. Dorn, and M.R. Anderson. Electrochemistry of C_{82}: relationship to metallofullerene electrochemistry. *J. Electroanalytical Chem.*, 417(1):1, 1996. 16

[59] M.R. Anderson, H.C. Dorn, and S. Stevenson. The Electrochemistry of $Sc_3@C_{82}$. *J. Am. Chem. Soc*, 119:437, 1997. 16

[60] K. Akiyama, K. Sueki, T. Kodama, K. Kikuchi, I. Ikemoto, M. Katada, and H. Nakahara. Absorption Spectra of Metallofullerenes $M@C_{82}$ of Lanthanoids. *J. Phys. Chem. A*, 104(31):7224, 2000. 17, 110

[61] H. Funasaka, K. Sakurai, Y. Oda, K. Yamamoto, and T. Takahashi. Magnetic properties of $Gd@C_{82}$ metallofullerene. *Chem. Phys. Lett.*, 232(3):273, 1995. 18

[62] H. Funasaka, K. Sugiyama, K. Yamamoto, and T. Takahashi. Magnetic properties of rare-earth metallofullerenes. *J. Phys. Chem.*, 99(7):1826, 1995. 18, 19

[63] Y. Ito, W. Fujita, T. Okazaki, T. Sugai, K. Awaga, E. Nishibori, M. Takata, M. Sakata, and H. Shinohara. Magnetic properties and crystal structure of solvent-free $Sc@C_{82}$ metallofullerene microcrystals. *Chem. Phys. Chem.*, 8(7):1019, 2007. 18, 19

[64] T. Watanuki, A. Fujiwara, K. Ishii, Y. Matuoka, H. Suematsu, K. Ohwada, H. Nakao, Y. Fujii, T. Kodama, K. Kikuchi, et al. Structural phase transitions of endohedral metallofullerene $La@C_{82}$ studied by single crystal X-ray diffraction. *Mole. crystals and liq. crystals*, 340:639, 2000. 19

[65] L.V. Radushkevich and V.M. Lukyanovich. Carbon structure formed under thermal decomposition of carbon monoxide on iron. *Zh. Fiz. Khim.(SoV. J. Phys. Chem.)*, 26:88–95, 1952. 19

[66] A. Oberlin and T. Endo. Filamentous growth of carbon through benzene decomposition. *Journal of Crystal Growth*, 32(3):335–349, 1976. 19

[67] S. Iijima. Helical microtubules of graphitic carbon. *nature*, 354(6348):56–58, 1991. 19, 22, 24

[68] H. Wang, J. Luo, A. Robertson, Y. Ito, W. Yan, V. Lang, M. Zaka, F. Schäffel, M.H. Rümmeli, and G.A.D. Briggs. High-Performance Field Effect Transistors from Solution Processed Carbon Nanotubes. *ACS nano*. 21

[69] D.S. Bethune, C.H. Klang, M.S. De Vries, G. Gorman, R. Savoy, J. Vazquez, and R. Beyers. Cobalt-catalysed growth of carbon nanotubes with single-atomic-layer walls. 1993. 24

[70] C. Journet, W.K. Maser, P. Bernier, A. Loiseau, M. Lamy de la Chapelle, S. Lefrant, P. Deniard, R. Lee, and J.E. Fischer. Large-scale production of single-walled carbon nanotubes by the electric-arc technique. *Nature*, 388(6644):756–757, 1997. 24

[71] S. Iijima and T. Ichihashi. Single-shell carbon nanotubes of 1-nm diameter. 1993. 24

[72] Y. Saito, T. Yoshikawa, M. Okuda, N. Fujimoto, K. Sumiyama, K. Suzuki, A. Kasuya, and Y. Nishina. Carbon nanocapsules encaging metals and car-

bides. *Journal of Physics and Chemistry of Solids*, 54(12):1849–1860, 1993. 24

[73] S. Seraphin and D. Zhou. Single-walled carbon nanotubes produced at high yield by mixed catalysts. *Applied Physics Letters*, 64(16):2087–2089, 2009. 24

[74] M. Takizawa, S. Bandow, M. Yudasaka, Y. Ando, H. Shimoyama, and S. Iijima. Change of tube diameter distribution of single-wall carbon nanotubes induced by changing the bimetallic ratio of Ni and Y catalysts. *Chemical Physics Letters*, 326(3-4):351–357, 2000. 24

[75] S. Farhat, M.L. de La Chapelle, A. Loiseau, C.D. Scott, S. Lefrant, C. Journet, and P. Bernier. Diameter control of single-walled carbon nanotubes using argon–helium mixture gases. *The Journal of Chemical Physics*, 115:6752, 2001. 24

[76] A. Thess, R. Lee, P. Nikolaev, H. Dai, P. Petit, J. Robert, C. Xu, Y.H. Lee, S.G. Kim, A.G. Rinzler, et al. Crystalline ropes of metallic carbon nanotubes. *Science*, 273(5274):483, 1996. 24

[77] M.H. Rümmeli, C. Kramberger, M. Löffler, O. Jost, M. Bystrzejewski, A. Grüneis, T. Gemming, W. Pompe, B. Büchner, and T. Pichler. Catalyst volume to surface area constraints for nucleating carbon nanotubes. *J. Phys. Chem. B*, 111(28):8234–8241, 2007. 25, 65, 67, 84, 118

[78] X. Fan, R. Buczko, A.A. Puretzky, D.B. Geohegan, J.Y. Howe, S.T. Pantelides, and S.J. Pennycook. Nucleation of single-walled carbon nanotubes. *Physical review letters*, 90(14):145501, 2003. 26

[79] S. Tetali, M. Zaka, R. Schönfelder, A. Bachmatiuk, F. Börrnert, I. Ibrahim, J.H. Lin, G. Cuniberti, J.H. Warner, B. Büchner, and M.H. Rümmeli. Unravelling the Mechanisms Behind Mixed Catalysts for the High Yield Production of Single-Walled Carbon Nanotubes. *ACS nano*, 3(12):3839–3844, 2009. 26

[80] J. Kong, A.M. Cassell, and H. Dai. Chemical vapor deposition of methane for single-walled carbon nanotubes. *Chemical Physics Letters*, 292(4-6):567–574, 1998. 27

[81] B. Zheng, C. Lu, G. Gu, A. Makarovski, G. Finkelstein, and J. Liu. Efficient CVD growth of single-walled carbon nanotubes on surfaces using carbon monoxide precursor. *Nano Letters*, 2(8):895–898, 2002. 27

[82] S. Fan, M.G. Chapline, N.R. Franklin, T.W. Tombler, A.M. Cassell, and H. Dai. Self-oriented regular arrays of carbon nanotubes and their field emission properties. *Science*, 283(5401):512, 1999. 27

[83] C.L. Cheung, A. Kurtz, H. Park, and C.M. Lieber. Diameter-controlled synthesis of carbon nanotubes. *J. Phys. Chem. B*, 106(10):2429–2433, 2002. 27

[84] K. Hata, D.N. Futaba, K. Mizuno, T. Namai, M. Yumura, and S. Iijima. Water-assisted highly efficient synthesis of impurity-free single-walled carbon nanotubes. *Science*, 306(5700):1362, 2004. 27, 29, 31

[85] M.J. Bronikowski, P.A. Willis, D.T. Colbert, KA Smith, and R.E. Smalley. Gas-phase production of carbon single-walled nanotubes from carbon monoxide via the HiPco process: A parametric study. *Journal of Vacuum Science & Technology A: Vacuum, Surfaces, and Films*, 19:1800, 2001. 28

[86] J. Lu, S. Nagase, S. Re, X. Zhang, D. Yu, J. Zhang, R. Han, Z. Gao, H. Ye, S. Zhang, et al. Interplay of single-wall carbon nanotubes and encapsulated La@ C_ {82}, La_ {2}@ C_ {80}, and Sc_ {3} N@ C_ {80}. *Physical Review B*, 71(23):235417, 2005. 28, 120, 135, 136

[87] G. Lolli, L. Zhang, L. Balzano, N. Sakulchaicharoen, Y. Tan, and D.E. Resasco. Tailoring (n, m) structure of single-walled carbon nanotubes by modifying reaction conditions and the nature of the support of CoMo catalysts. *J. Phys. Chem. B*, 110(5):2108–2115, 2006. 28, 29

[88] W.E. Alvarez, F. Pompeo, J.E. Herrera, L. Balzano, and D.E. Resasco. Characterization of Single-Walled Carbon Nanotubes (SWNTs) Produced by CO Disproportionation on Co- Mo Catalysts. *Chem. Mater*, 14(4):1853–1858, 2002. 28

[89] D.E. Resasco, W.E. Alvarez, F. Pompeo, L. Balzano, J.E. Herrera, B. Kitiyanan, and A. Borgna. A scalable process for production of single-walled carbon nanotubes (SWNTs) by catalytic disproportionation of CO on a solid catalyst. *Journal of Nanoparticle Research*, 4(1):131–136, 2002. 28

[90] I.W. Chiang, B.E. Brinson, R.E. Smalley, J.L. Margrave, and R.H. Hauge. Purification and characterization of single-wall carbon nanotubes. *J. Phys. Chem. B*, 105(6):1157–1161, 2001. 30

[91] H. Hu, B. Zhao, M.E. Itkis, and R.C. Haddon. Nitric acid purification of single-walled carbon nanotubes. *J. Phys. Chem. B*, 107(50):13838–13842, 2003. 30, 87

[92] R. Schönfelder, M.H. Rümmeli, W. Gruner, M. Löffler, J. Acker, V. Hoffmann, T. Gemming, B. Büchner, and T. Pichler. Purification-induced sidewall functionalization of magnetically pure single-walled carbon nanotubes. *Nanotechnology*, 18:375601, 2007. 30, 67, 84

[93] K.B. Shelimov, R.O. Esenaliev, A.G. Rinzler, C.B. Huffman, and R.E. Smalley. Purification of single-wall carbon nanotubes by ultrasonically assisted filtration. *Chemical physics letters*, 282(5-6):429–434, 1998. 31, 91, 102

[94] G.S. Duesberg, W. Blau, H.J. Byrne, J. Muster, M. Burghard, and S. Roth. Chromatography of carbon nanotubes. *Synthetic Metals*, 103(1-3):2484–2485, 1999. 31

[95] X. Huang, R.S. Mclean, and M. Zheng. High-resolution length sorting and purification of DNA-wrapped carbon nanotubes by size-exclusion chromatography. *Anal. Chem*, 77(19):6225–6228, 2005. 31

[96] A. Yu, E. Bekyarova, M.E. Itkis, D. Fakhrutdinov, R. Webster, and R.C. Haddon. Application of centrifugation to the large-scale purification of electric arc-produced single-walled carbon nanotubes. *J. Am. Chem. Soc*, 128(30):9902–9908, 2006. 31

[97] X. Li, X. Tu, S. Zaric, K. Welsher, W.S. Seo, W. Zhao, and H. Dai. Selective synthesis combined with chemical separation of single-walled carbon nanotubes for chirality selection. *J. Am. Chem. Soc*, 129(51):15770–15771, 2007. 32

[98] S.M. Bachilo, L. Balzano, J.E. Herrera, F. Pompeo, D.E. Resasco, and R.B. Weisman. Narrow (n, m)-distribution of single-walled carbon nanotubes grown

using a solid supported catalyst. *Journal of the American Chemical Society*, 125(37):11186–11187, 2003. 32

[99] L. Ding, A. Tselev, J. Wang, D. Yuan, H. Chu, T.P. McNicholas, Y. Li, and J. Liu. Selective growth of well-aligned semiconducting single-walled carbon nanotubes. *Nano letters*, 9(2):800–805, 2009. 32

[100] Y. Li, D. Mann, M. Rolandi, W. Kim, A. Ural, S. Hung, A. Javey, J. Cao, D. Wang, E. Yenilmez, et al. Preferential growth of semiconducting single-walled carbon nanotubes by a plasma enhanced CVD method. *Nano Letters*, 4(2):317–321, 2004. 32

[101] L. Qu, F. Du, and L. Dai. Preferential syntheses of semiconducting vertically aligned single-walled carbon nanotubes for direct use in FETs. *Nano Lett*, 8(9):2682–2687, 2008. 32

[102] R. Krupke, F. Hennrich, H. Lohneysen, and M.M. Kappes. Separation of metallic from semiconducting single-walled carbon nanotubes. *Science*, 301(5631):344, 2003. 32, 34

[103] M. Zheng, A. Jagota, E.D. Semke, B.A. Diner, R.S. McLean, S.R. Lustig, R.E. Richardson, and N.G. Tassi. DNA-assisted dispersion and separation of carbon nanotubes. *Nature Materials*, 2(5):338–342, 2003. 33, 34

[104] X. Tu, S. Manohar, A. Jagota, and M. Zheng. DNA sequence motifs for structure-specific recognition and separation of carbon nanotubes. *Nature*, 460(7252):250–253, 2009. 33, 34

[105] A. Nish, J.Y. Hwang, J. Doig, and R.J. Nicholas. Highly selective dispersion

of single-walled carbon nanotubes using aromatic polymers. *Nature Nanotechnology*, 2(10):640–646, 2007. 33

[106] F. Chen, B. Wang, Y. Chen, and L.J. Li. Toward the extraction of single species of single-walled carbon nanotubes using fluorene-based polymers. *Nano lett*, 7(10):3013–3017, 2007. 33

[107] M.S. Arnold, A.A. Green, J.F. Hulvat, S.I. Stupp, and M.C. Hersam. Sorting carbon nanotubes by electronic structure using density differentiation. *Nature nanotechnology*, 1(1):60–65, 2006. 33, 34, 65, 75, 84, 97

[108] E.J.F. Carvalho and M.C. dos Santos. Role of Surfactants in Carbon Nanotubes Density Gradient Separation. *ACS nano*, 4(2):765–770, 2010. 35

[109] K. Yanagi, Y. Miyata, T. Tanaka, S. Fujii, D. Nishide, and H. Kataura. Colors of carbon nanotubes. *Diamond and Related Materials*, 18(5-8):935–939, 2009. 35

[110] Y. Feng, Y. Miyata, K. Matsuishi, and H. Kataura. High-Efficiency Separation of Single-Wall Carbon Nanotubes by Self-Generated Density Gradient Ultracentrifugation. *The Journal of Physical Chemistry C*, pages 2204–2206, 2011. 35

[111] B.W. Smith, M. Monthioux, and D.E. Luzzi. Encapsulated C_{60}in carbon nanotubes. *Nature*, page 323, 1998. 35, 36, 117

[112] B. Burteaux, A. Claye, B.W. Smith, M. Monthioux, D.E. Luzzi, and J.E. Fischer. Abundance of encapsulated C_{6n} in single wall nanotubes. *Chem. Phys. Lett*, 310:21, 1999. 35

[113] D.A. Britz, A.N. Khlobystov, K. Porfyrakis, A. Ardavan, and G.A.D. Briggs. Chemical reactions inside single-walled carbon nano test-tubes. *Chem. Comm.*, (1):37, 2005. 36

[114] S. Okada, S. Saito, and A. Oshiyama. Energetics and Electronic Structures of Encapsulated C_{60} in a Carbon Nanotube. *Phys. Rev. Lett.*, 86(17):3835, 2001. 36

[115] M. Otani, S. Okada, and A. Oshiyama. Energetics and electronic structures of one-dimensional fullerene chains encapsulated in zigzag nanotubes. *Phys. Rev. B*, 68(12):125424, 2003. 36

[116] W. Song, M. Ni, J. Lu, Z. Gao, S. Nagase, D. Yu, H. Ye, and X. Zhang. Encapsulations of La@C_{82} and La_2@C_{80} inside single-walled boron nitride nanotubes. *J. Mole. Struc.*, 730(1-3):121, 2005. 37

[117] K. Hirahara, K. Suenaga, S. Bandow, H. Kato, T. Okazaki, H. Shinohara, and S. Iijima. One-Dimensional Metallofullerene Crystal Generated Inside Single-Walled Carbon Nanotubes. *Phys. Rev. Lett.*, 85(25):5384, 2000. 37

[118] F. Simon, H. Kuzmany, H. Rauf, T. Pichler, J. Bernardi, H. Peterlik, L. Korecz, F. Fülöp, and A. Jánossy. Low temperature fullerene encapsulation in single wall carbon nanotubes: synthesis of N@C_{60}@SWCNT. *Chem. Phy. Lett.*, 383(3):362, 2004. 38

[119] A. Mrzel, A. Hassanien, Z. Liu, K. Suenaga, Y. Miyata, K. Yanagi, and H. Kataura. Effective, fast, and low temperature encapsulation of fullerene derivatives in single wall carbon nanotubes. *Surface Science*, 601(22):5116, 2007. 38

[120] A.N. Khlobystov, D.A. Britz, J. Wang, S.A. O'Neil, M. Poliakoff, and G.A.D. Briggs. Low temperature assembly of fullerene arrays in single-walled carbon nanotubes using supercritical fluids. *J. Mater. Chem.*, 14(19):2852, 2004. 38, 39

[121] E.T. Thostenson, Z. Ren, and T.W. Chou. Advances in the science and technology of carbon nanotubes and their composites: a review. *Comp. Sci. and Tech.*, 61(13):1899, 2001. 39

[122] T. Belin and F. Epron. Characterization methods of carbon nanotubes: a review. *Mat. Sci. and Eng. B*, 119:105–118, 2005. 39

[123] X. Liu, T. Pichler, M. Knupfer, MS Golden, J. Fink, H. Kataura, Y. Achiba, K. Hirahara, and S. Iijima. Filling factors, structural, and electronic properties of C_{60} molecules in single-wall carbon nanotubes. *Phys. Rev. B*, 65(4):45419, 2002. 40

[124] J.H. Warner, Y. Ito, M. Zaka, L. Ge, T. Akachi, H. Okimoto, K. Porfyrakis, A.A. Watt, H. Shinohara, and G.A.D. Briggs. Rotating Fullerene Chains in Carbon Nanopeapods. *Nano Lett*, 8(8):2328, 2008. 40, 117

[125] J.H. Warner, F. Schäffel, G. Zhong, M.H. Rümmeli, B. Büchner, J. Robertson, and G.A.D. Briggs. Investigating the Diameter-Dependent Stability of Single-Walled Carbon Nanotubes. *ACS nano*, 3(6):1557–1563, 2009. 40, 56

[126] J. Cambedouzou, V. Pichot, S. Rols, P. Launois, P. Petit, R. Klement, H. Kataura, R. Almairac, and G.D. des Phases Condensees. On the diffraction pattern of C_{60} peapods. *Euro. Phys. J. B*, 42(1):31, 2004. 40

[127] M. Hodak and L.A. Girifalco. Ordered phases of fullerene molecules formed inside carbon nanotubes. *Phys. Rev. B*, 67(7):75419, 2003. 41

[128] A.N. Khlobystov, D.A. Britz, A. Ardavan, and G.A.D. Briggs. Observation of Ordered Phases of Fullerenes in Carbon Nanotubes. *Phys. Rev. Lett.*, 92(24):245507, 2004. 41

[129] A.N. Khlobystov, D.A. Britz, and G.A.D. Briggs. Molecules in Carbon Nanotubes. *Acc. Chem. Res*, 38(12):901, 2005. 41, 42

[130] L. Guan, H. Li, Z. Shi, L. You, and Z. Gu. Standing or lying C_{70}s encapsulated in carbon nanotubes with different diameters. *Solid State Comm.*, 133(5):333, 2005. 41

[131] K. Suenaga, T. Okazaki, K. Hirahara, S. Bandow, H. Kato, A. Taninaka, H. Shinohara, and S. Iijima. High-resolution electron microscopy of individual metallofullerene molecules on the dipole orientations in peapods. *App. Phy. A*, 76(4):445, 2003. 42

[132] T. Okazaki, T. Shimada, K. Suenaga, Y. Ohno, T. Mizutani, J. Lee, Y. Kuk, and H. Shinohara. Electronic properties of Gd@C_{82} metallofullerene peapods:(Gd@C_{82})n@SWNTs. *App. Phy. A*, 76(4):475–478, 2003. 43, 44

[133] P. Jakes, A. Gembus, K.P. Dinse, and K. Hata. Electron paramagnetic resonance investigation of metalloendofullerene derived carbon nanotube peapods. *J. Chem. Phys.*, 128:052306, 2008. 44, 111, 118, 135

[134] B. Corzilius, A. Gembus, N. Weiden, and K.P. Dinse. Preparation and EPR

characterization of N@C_{60} and N@C_{70} based peapods. *AIP Conference Proceedings*, 786:317, 2005. 44

[135] T. Shimada, T. Okazaki, R. Taniguchi, T. Sugai, H. Shinohara, K. Suenaga, Y. Ohno, S. Mizuno, S. Kishimoto, and T. Mizutani. Ambipolar field-effect transistor behavior of Gd@C_{82} metallofullerene peapods. *Applied physics letters*, 81(21):4067–4069, 2002. 45

[136] T. Shimada, Y. Ohno, T. Okazaki, T. Sugai, K. Suenaga, S. Kishimoto, T. Mizutani, T. Inoue, R. Taniguchi, N. Fukui, et al. Transport properties of C_{78}, C_{90} and Dy@C_{82} fullerenes-nanopeapods by field effect transistors. *Physica E: Low-dimensional Systems and Nanostructures*, 21(2-4):1089, 2004. 45

[137] A.L. Cantone, M.R. Buitelaar, C.G. Smith, D. Anderson, G.A.C. Jones, S.J. Chorley, C. Casiraghi, A. Lombardo, A.C. Ferrari, H. Shinohara, et al. Electronic transport characterization of Sc@C_{82} single-wall carbon nanotube peapods. *Journal of Applied Physics*, 104:083717–1, 2008. 46, 93

[138] T. Akasaka, S. Nagase, K. Kobayashi, M. Walchli, K. Yamamoto, H. Funasaka, M. Kako, T. Hoshino, and T. Erata. ^{13}C AND ^{139}LA NMR studies of La_2@C_{80} : First evidence for circular motion of metal atoms in endohedral dimetallofullerenes. *Ang. Chemie. Int.*, 36(15):1643, 1997. 46, 47

[139] A.N. Khlobystov, K. Porfyrakis, M. Kanai, D.A. Britz, A. Ardavan, H. Shinohara, T.J.S. Dennis, and G.A.D. Briggs. Molecular Motion of Endohedral Fullerenes in Single-Walled Carbon Nanotubes. *Ang. Chemie. Int.*, 43(11):1386, 2004. 46, 47

[140] K. Suenaga, R. Taniguchi, T. Shimada, T. Okazaki, H. Shinohara, and S. Iijima. Evidence for the Intramolecular Motion of Gd Atoms in a $Gd_2@C_{92}$ Nanopeapod. *Nano. Lett.*, 3(10):1395, 2003. 46

[141] J.H. Warner, A.A.R. Watt, L. Ge, K. Porfyrakis, T. Akachi, H. Okimoto, Y. Ito, A. Ardavan, B. Montanari, J.H. Jefferson, et al. Dynamics of paramagnetic metallofullerenes in carbon nanotube peapods. *Nano letters*, 8(4):1005–1010, 2008. 47, 141

[142] M. Brustolon and G. Giamello. *Electron paramagnetic resonance: a practitioner's toolkit*. John Wiley & Sons Inc, 2009. 51, 52

[143] C.A. Popp and J.S. Hyde. Effects of oxygen on EPR spectra of nitroxide spin-label probes of model membranes. *Journal of Magnetic Resonance (1969)*, 43(2):249–258, 1981. 53

[144] E. Ruska. The early development of electron lenses and electron microscopy. *Applied Optics*, 25:820, 1986. 55

[145] R. Erni, M.D. Rossell, C. Kisielowski, and U. Dahmen. Atomic-resolution imaging with a sub-50-pm electron probe. *Physical review letters*, 102(9):96101, 2009. 55, 58

[146] F. Banhart. Irradiation effects in carbon nanostructures. *Reports on Progress in Physics*, 62:1181, 1999. 56

[147] N. Tanaka, J. Yamasaki, T. Kawai, and H. Pan. The first observation of carbon nanotubes by spherical aberration corrected high-resolution transmission electron microscopy. *Nanotechnology*, 15:1779, 2004. 56

[148] N. Tanaka. Present status and future prospects of spherical aberration corrected TEM/STEM for study of nanomaterials. *Science and Technology of Advanced Materials*, 9:014111, 2008. 56

[149] K. Hirahara, K. Saitoh, J. Yamasaki, and N. Tanaka. Direct observation of six-membered rings in the upper and lower walls of a single-wall carbon nanotube by spherical aberration-corrected HRTEM. *Nano Lett*, 6(8):1778–1783, 2006. 58

[150] S.M. Bachilo, M.S. Strano, C. Kittrell, R.H. Hauge, R.E. Smalley, and R.B. Weisman. Structure-assigned optical spectra of single-walled carbon nanotubes. *Science*, 298(5602):2361, 2002. 58

[151] H. Kataura, Y. Kumazawa, Y. Maniwa, I. Umezu, S. Suzuki, Y. Ohtsuka, and Y. Achiba. Optical properties of single-wall carbon nanotubes. *Synthetic Metals*, 103(1-3):2555–2558, 1999. 59, 60

[152] M.E. Itkis, D.E. Perea, S. Niyogi, S.M. Rickard, M.A. Hamon, H. Hu, B. Zhao, and R.C. Haddon. Purity evaluation of as-prepared single-walled carbon nanotube soot by use of solution-phase near-IR spectroscopy. *Nano Letters*, 3(3):309–314, 2003. 60, 89

[153] M.S. Dresselhaus, G. Dresselhaus, R. Saito, and A. Jorio. Raman spectroscopy of carbon nanotubes. *Physics Reports*, 409(2):47–99, 2005. 60, 61

[154] N.B. Colthup, L.H. Daly, and S.E. Wiberley. *Introduction to infrared and Raman spectroscopy*. Academic press New York, 1990. 61

[155] P.C. Eklund, J.M. Holden, and R.A. Jishi. Vibrational modes of carbon nanotubes; spectroscopy and theory. *Carbon*, 33(7):959–972, 1995. 61, 100, 139

[156] L.E. Hueso, J.M. Pruneda, V. Ferrari, G. Burnell, J.P. Valdés-Herrera, B.D. Simons, P.B. Littlewood, E. Artacho, A. Fert, and N.D. Mathur. Transformation of spin information into large electrical signals using carbon nanotubes. *Nature*, 445(7126):410–413, 2007. 63

[157] P. Petit, E. Jouguelet, J.E Fischer, A.G. Rinzler, and R.E. Smalley. Electron spin resonance and microwave resistivity of single-wall carbon nanotubes. *Physical Review B*, 56(15):9275–9278, 1997. 63, 64

[158] S. Bandow, S. Asaka, X. Zhao, and Y. Ando. Purification and magnetic properties of carbon nanotubes. *Applied Physics A: Materials Science & Processing*, 67(1):23–27, 1998. 63, 64

[159] J.P. Salvetat, T. Fehér, C. LHuillier, F. Beuneu, and L. Forró. Anomalous electron spin resonance behavior of single-walled carbon nanotubes. *Physical Review B*, 72(7):75440, 2005. 64

[160] B. Corzilius, A. Gembus, N. Weiden, K.P. Dinse, and K. Hata. EPR characterization of catalyst-free SWNT and N@C_{60}-based peapods. *physica status solidi (b)*, 243(13):3273–3276, 2006. 64

[161] M. Zaka, J.H. Warner, Y. Ito, J.J.L. Morton, M.H. Rümmeli, T. Pichler, A. Ardavan, H. Shinohara, and G.A.D. Briggs. Exchange interactions of spin-active metallofullerenes in solid-state carbon networks. *Physical Review B*, 81(7):75424, 2010. 64, 65

[162] B. Náfrádi, NM Nemes, T. Fehér, L. Forró, Y. Kim, J.E. Fischer, D.E. Luzzi, F. Simon, and H. Kuzmany. Electron spin resonance of single-walled carbon nanotubes and related structures. *physica status solidi (b)*, 243(13):3106–3110, 2006. 64

[163] K. Shen, D.L. Tierney, and T. Pietraß. Electron spin resonance of carbon nanotubes under hydrogen adsorption. *Physical Review B*, 68(16):165418, 2003. 64

[164] R. Kitaura, D. Ogawa, Kobayashi, T. Saito, S. Ohshima, T. Nakamura, H. Yoshikawa, K. Awaga, and H. Shinohara. High yield synthesis and characterization of the structural and magnetic properties of crystalline ErCl 3 nanowires in single-walled carbon nanotube templates. *Nano Research*, 1(2):152–157, 2008. 65, 70, 102

[165] D. Nishide, Y. Miyata, K. Yanagi, T. Tanaka, and H. Kataura. Effective Separation of Carbon Nanotubes and Metal Particles from Pristine Raw Soot by Ultracentrifugation. *Japanese Journal of Applied Physics*, 48(1):015004–4, 2009. 65

[166] K. Yanagi, Y. Miyata, and H. Kataura. Optical and conductive characteristics of metallic single-wall carbon nanotubes with three basic colors; cyan, magenta, and yellow. *Applied Physics Express*, 1(3):34003, 2008. 65, 75, 79

[167] K. Yanagi, T. Iitsuka, S. Fujii, and H. Kataura. Separations of metallic and semiconducting carbon nanotubes by using sucrose as a gradient medium. *The Journal of Physical Chemistry C*, 112(48):18889–18894, 2008. 66

[168] X. Zhao, S. Inoue, M. Jinno, T. Suzuki, and Y. Ando. Macroscopic oriented web of single-wall carbon nanotubes. *Chemical Physics Letters*, 373(3-4):266–271, 2003. 69, 86, 98, 102

[169] J. Liu, M.J. Casavant, M. Cox, D.A. Walters, P. Boul, W. Lu, A.J. Rimberg, K.A. Smith, D.T. Colbert, and R.E. Smalley. Controlled deposition of individual single-walled carbon nanotubes on chemically functionalized templates. *Chemical Physics Letters*, 303(1-2):125–129, 1999. 71

[170] S. Ghosh, S.M. Bachilo, and R.B. Weisman. Advanced sorting of single-walled carbon nanotubes by nonlinear density-gradient ultracentrifugation. *Nature Nanotechnology*, 2010. 81

[171] Y. Feng, Y. Miyata, K. Matsuishi, and H. Kataura. High-Efficiency Separation of Single-Wall Carbon Nanotubes by Self-Generated Density Gradient Ultracentrifugation. *The Journal of Physical Chemistry C*, pages 2204–2206. 82

[172] M. Yudasaka, M. Zhang, C. Jabs, and S. Iijima. Effect of an organic polymer in purification and cutting of single-wall carbon nanotubes. *Applied Physics A: Materials Science & Processing*, 71(4):449–451, 2000. 91

[173] Y. Asada, Y. Miyata, Y. Ohno, R. Kitaura, T. Sugai, T. Mizutani, and H. Shinohara. High-Performance Thin-Film Transistors with DNA-Assisted Solution Processing of Isolated Single-Walled Carbon Nanotubes. *Advanced Materials*, 22(24):2698–2701, 2010. 93

[174] F. Schäffel, C. Täschner, M.H. Rümmeli, V. Neu, U. Wolff, U. Queitsch, D. Pohl, R. Kaltofen, A. Leonhardt, B. Rellinghaus, et al. Carbon nanotubes

terminated with hard magnetic FePt nanomagnets. *Applied Physics Letters*, 94:193107, 2009. 99

[175] L. Dennany, P. Sherrell, J. Chen, P.C. Innis, G.G. Wallace, and A.I. Minett. EPR characterisation of platinum nanoparticle functionalised carbon nanotube hybrid materials. *Physical Chemistry Chemical Physics*, 12(16):4135–4141, 2010. 100, 102, 139

[176] C.S. Nicolau, H.G. Thom, and E. Pobitschka. Electron spin resonance studies of some supported hydrogenation-dehydrogenation catalysts. *Transactions of the Faraday Society*, 55:1430–1434, 1959. 100, 102

[177] J. Wang, Y. Lu, X. Li, and M. Dong. Point-Defect Mediated Bonding of Pt Clusters on (5, 5) Carbon Nanotubes. *The Journal of Physical Chemistry C*, 113(3):890–893, 2008. 101, 102

[178] K.L. Lu, R.M. Lago, Y.K. Chen, M.L.H Green, P.J.F. Harris, and S.C. Tsang. Mechanical damage of carbon nanotubes by ultrasound. *Carbon*, 34(6):814 – 816, 1996. 102

[179] A. De Martino, R. Egger, K. Hallberg, and C.A. Balseiro. Spin-orbit coupling and electron spin resonance theory for carbon nanotubes. *Physical review letters*, 88(20):206402, 2002. 102

[180] F. Kuemmeth, S. Ilani, D.C. Ralph, and P.L. McEuen. Coupling of spin and orbital motion of electrons in carbon nanotubes. *Nature*, 452(7186):448–452, 2008. 102

[181] D. Huertas-Hernando, F. Guinea, and A. Brataas. Spin-orbit coupling in

curved graphene, fullerenes, nanotubes, and nanotube caps. *Physical Review B*, 74(15):155426, 2006. 103

[182] J.R. Heath, S.C. O'Brien, Q. Zhang, Y. Liu, R.F. Curl, F.K. Tittel, and R.E. Smalley. Lanthanum complexes of spheroidal carbon shells. *J. Am. Chem. Soc.*, 107(25):7779, 1985. 105

[183] L. Ge, B. Montanari, J.H. Jefferson, D.G. Pettifor, N.M. Harrison, and G.A.D. Briggs. Modeling spin interactions in carbon peapods using a hybrid density functional theory. *Physical Review B*, 77(23):235416, 2008. 106, 117

[184] L. Ge, J.H. Jefferson, B. Montanari, N.M. Harrison, D.G. Pettifor, and G.A.D. Briggs. Effects of Doping on Electronic Structure and Correlations in Carbon Peapods. *ACS nano*, 3(5):1069–1076, 2009. 106

[185] C.J. Nuttall, Y. Inada, K. Nagai, and Y. Iwasa. Low-temperature bistability in the magnetic properties of solvent-including lanthanide metallofullerene crystals. *Physical Review B*, 62(13):8592–8595, 2000. 106, 110

[186] T. Kato, S. Suzuki, K. Kikuchi, and Y. Achiba. ESR study of the electronic structures of metallofullerenes: a comparison between lanthanum fullerene ($La@C_{82}$) and scandium fullerene ($Sc@C_{82}$). *Journal of Physical Chemistry*, 97(51):13425–13428, 1993. 106

[187] J.H. Weaver, Y. Chai, G.H. Kroll, C. Jin, T.R. Ohno, R.E. Haufler, T. Guo, J.M. Alford, J. Conceicao, L.P.F. Chibante, et al. XPS probes of carbon-caged metals. *Chem. phys. lett.*, 190(5):460, 1992. 107

[188] P.W. Anderson and P.R. Weiss. Exchange narrowing in paramagnetic resonance. *Reviews of Modern Physics*, 25(1):269–276, 1953. 108

[189] V.M. Berdnikov, A.B. Doktorov, and L.L. Makarshin. The dipole-dipole broadening of the ESR spectra of free radicals in the presence of paramagnetic ions. *Theoretical and Experimental Chemistry*, 16(6):554–559, 1981. 109

[190] N. Weiden, T. Kato, and K.P. Dinse. Hyperfine Interactions in La@C_{82} Studied by W-Band Electron Paramagnetic Resonance and Electron Nuclear Double Resonance. *J. Phys. Chem. B*, 108(27):9469–9474, 2004. 110

[191] S. Knorr, A. Grupp, M. Mehring, U. Kirbach, A. Bartl, and L. Dunsch. Pulsed ESR investigations of anisotropic interactions in M@C_{82} (M= Sc, Y, La). *App. Phys. A: Materials Science & Processing*, 66(3):257, 1998. 110

[192] H. Shinohara. Endohedral metallofullerenes. *Reports on progress in Physics*, 63(6):843, 2000. 110

[193] S. Stoll and A. Schweiger. EasySpin, a comprehensive software package for spectral simulation and analysis in EPR. *Journal of Magnetic Resonance*, 178(1):42–55, 2006. 111

[194] Y. Ito, J.H. Warner, R. Brown, M. Zaka, R. Pfeiffer, T. Aono, N. Izumi, H. Okimoto, J.J.L. Morton, A. Ardavan, and G.A.D. Briggs. Controlling intermolecular spin interactions of La@C_{82} in empty fullerene matrices. *Physical Chemistry Chemical Physics*, 12(7):1618–1623, 2010. 115

[195] C. Knapp, K.P. Dinse, B. Pietzak, M. Waiblinger, and A. Weidinger. Fourier

transform EPR study of N@C_{60} in solution. *Chemical Physics Letters*, 272(5-6):433–437, 1997. 118

[196] B. Pietzak, M. Waiblinger, T.A. Murphy, A. Weidinger, M. Höhne, E. Dietel, and A. Hirsch. Properties of endohedral N@C_{60}. *Carbon*, 36(5-6):613–615, 1998. 118

[197] M. Hodak and LA Girifalco. Fullerenes inside carbon nanotubes and multi-walled carbon nanotubes: optimum and maximum sizes. *Chemical physics letters*, 350(5-6):405–411, 2001. 119

[198] T. Wakahara, J. Kobayashi, M. Yamada, Y. Maeda, T. Tsuchiya, M. Okamura, T. Akasaka, M. Waelchli, K. Kobayashi, S. Nagase, et al. Characterization of Ce@C_{82} and its anion. *J. Am. Chem. Soc*, 126(15):4883–4887, 2004. 131

[199] A. Débarre, R. Jaffiol, C. Julien, D. Nutarelli, A. Richard, and P. Tchénio. Specific raman signatures of a dimetallofullerene peapod. *Phys. Rev. Lett.*, 91(8):085501, Aug 2003. 135

[200] Y. Nakayama, S. Fujiki, Y. Hirado, H. Shiozawa, H. Ishii, T. Miyahara, Y. Maniwa, T. Kodama, Y. Achiba, H. Kataura, et al. Photoemission study of electronic structures of fullerene and metallofullerene peapods. *physica status solidi (b)*, 245(10):2025–2028, 2008. 135

[201] Y. Cho, S. Han, G. Kim, H. Lee, and J. Ihm. Orbital hybridization and charge transfer in carbon nanopeapods. *Physical review letters*, 90(10):106402, 2003. 135

[202] T. Suzuki Koichi, F. Oguri, Y. Nakao, S. Suzuki, Y. Achiba Kazunori, et al.

Electrochemical properties of fullerenolanthanides. *Tetrahedron*, 52(14):4973–4982, 1996. 136

[203] T. Akasaka, T. Wakahara, S. Nagase, K. Kobayashi, M. Waelchli, K. Yamamoto, M. Kondo, S. Shirakura, S. Okubo, Y. Maeda, et al. La@C_{82} anion. An unusually stable metallofullerene. *Journal of the American Chemical Society*, 122(38):9316–9317, 2000. 136

[204] A. Vargová, A. Popov, P. Rapta, B. Sun, L. Zhang, and L. Dunsch. Electrochemical Tuning of Spin States of the Endohedral Metallofullerene Y@C_{82} as Probed by ESR Spectroelectrochemistry. *ChemPhysChem*, 11(8):1650–1653, 2010. 136

[205] M. Havlicek, W. Jantsch, M. Rümmeli, R. Schönfelder, K. Yanagi, Y. Miyata, H. Kataura, F. Simon, H. Peterlik, and H. Kuzmany. Electron spin resonance from semiconductor–metal separated SWCNTs. *physica status solidi (b)*, 247(11):2851, 2010. 148